Surface Engineering of $Cu(In,Ga)Se_2$ by KF and CdS – a Study by High-Energy Photoemission Spectroscopy

Dissertation

zur Erlangung des akademischen Grades
eines Doktors der Naturwissenschaften
(Dr. rer. nat.)

von

Bünyamin Ümsür

eingereicht am Fachbereich Physik
der Freien Universität Berlin

angefertigt am
Helmholtz Zentrum Berlin für Materialien und Energie

2017

Gutachter:

1. Frau Prof. Dr. M. Ch. Lux-Steiner (Betreuerin)

2. Herr Prof. Dr. W. Kuch

Disputation am 26.6.2017

To my brother, Yusuf Ümsür...

Table of Contents

Abstract 9

Kurzfassung 11

1 Introduction 13

2 Material Properties of $Cu(In,Ga)Se_2$ and CdS Compounds 17

2.1 Structure of CIGSe-Based Thin Film Solar Cells 17

2.2 Crystal Structure of CIGSe 19

2.3 Phase Diagram of CIGSe 20

2.4 Defects in CI(G)Se 22

2.5 Band Gap Energy of $Cu(In_{1-x},Ga_x)Se_2$ 24

2.6 Basic Properties of CdS 25

2.7 Electronic Band Diagram of CIGSe-Based Thin Film Solar Cell 26

2.8 The Role of CBD-CdS Buffer Layer 27

2.9 The Effect of KF Post-Deposition Treatment 28

3 Sample Preparation and Characterization Methods 29

3.1 Preparation of $Cu(In,Ga)Se_2$ Thin Films and $Cu(In,Ga)Se_2$/CdS Heterostructures 29

3.1.1 $Cu(In,Ga)Se_2$ Absorber Films: Growth and Post Treatments 30

3.1.2 Chemical Bath Deposition of the CdS 32

3.1.3 Detailed Description of the Samples under Investigation 34

3.2 Microstructure Characterization Methods 36

3.2.1 X-ray Photoelectron Spectroscopy 36

3.2.2 Ultraviolet Photoelectron Spectroscopy 47

3.3 Experimental Setups for XPS-UPS and HAXPES Measurements 48

3.3.1 CISSY Setup for XPS and UPS 48

3.3.2 HIKE Setup for HAXPES 49

4 Cd Diffusion into Cu-rich and Cu-poor $Cu(In,Ga)Se_2$ Absorbers 51

4.1 Mechanism of the Cd Diffusion into Cu-rich and Cu-poor CIGSe Absorbers: Theoretical Considerations 52

4.2 Composition-Dependent Cd Diffusion into CIGSe Absorbers 56

4.3 Chemical Changes at the Cu-rich and Cu-poor CIGSe/CdS Interface upon Annealing 72

4.4 Summary 78

5 Impact of KF Post-Deposition Treatment on the Cu(In,Ga)Se_2/CdS Interface 81

5.1 Analysis of CIGSe+KF/CdS and CIGSe/CdS Interfaces by Depth-Resolved HAXPES 82

5.2 Surface Properties of CIGSe and CIGSe+KF Absorbers and the Influence of Ammonia Etching during the CBD Process 96

5.3 Summary 104

6 Summary 107

7 Appendices 111

7.1 Nomenclature of the Photoelectrons 111

7.2 Reference Data for XPS 113

7.3 Supporting Material for Chapter 4 116

7.4 List of Abbreviations and Symbols 118

References 121

List of publications 141

Acknowledgments 145

Selbständigkeitserklärung 147

Curriculum Vitae 149

Abstract

Thin film solar cells based on polycrystalline Cu(In,Ga)Se_2 (CIGSe) absorbers have reached a maximum conversion efficiency of 22.8% on the laboratory scale, already exceeding efficiencies of solar cells based on polycrystalline silicon. However, many questions about the exact surface and near-surface composition remain and a complete picture of the formation of the interface to the CdS buffer layer is still under debate. In this work, first, the interface formation between CIGSe and CdS was investigated by means of hard x-ray photoelectron spectroscopy (HAXPES) depending on the Cu concentration of the CIGSe. For this purpose, a Cu-poor and a Cu-rich absorber with bulk Cu to In+Ga ratios of 0.80 and 0.95, respectively, were compared. It was shown that the Cd diffusion into the Cu-poor absorber is a two-step process, where Cu atoms are actively exchanged by Cd impurities during the diffusion process; whereas in the Cu-rich sample, the Cu atoms are not directly involved in the diffusion process. In addition, it was observed that by having a lower activation energy for Cd diffusion in the Cu-poor samples, Cd atoms completely disappeared from the near-surface region after an annealing process up to 400 °C, whereas a small amount of Cd could be still measured within the same depth of Cu-rich sample after the same annealing process. Another difference in the interface formation of Cu-poor and Cu-rich CIGSe/CdS samples upon the annealing process was found to be a Ga diffusion towards the CIGSe surface. In contrast to the Cu-rich sample, a significant Ga diffusion towards the CIGSe surface was observed in case of the Cu-poor samples at elevated temperatures.

Second, the impact of KF post-deposition treatment of CIGSe on the CIGSe/CdS interface was investigated by means of depth-resolved HAXPES. Besides a strong intermixing at the interface, an increased Cu depletion due to the KF-PDT was observed in combination with an increased accumulation of Cd and S. A general shift of about 0.15 eV to higher binding energies of the CIGSe valence band at the absorber surface as well as the CIGSe and CdS related core levels was measured on the KF treated sample. This phenomenon was attributed to the impact of additional cadmium, which acts as donor and releases further electrons into the conduction band of the absorber. Then, the electrons accumulate at the CdS surface after having passed the interface region. This additional surface charge leads to a pronounced shift in the photoemission spectra as observed on the KF treated CIGSe absorber compared to the non-treated absorber.

Kurzfassung

Chalcopyrit-Dünnschichtsolarzellen haben im Labormaßstab einen maximalen Wirkungsgrad von 22.8 % erreicht. Allerdings bleiben viele offene Fragen über die genaue Oberfläche und oberflächennahe Zusammensetzung, und ein vollständiges Bild von der Ausbildung der Grenzfläche zum CdS-Pufferschicht wird noch diskutiert. In dieser Arbeit wurde zunächst die Grenzflächenbildung zwischen CIGSe und CdS mittels HAXPES (engl. hard x-ray photoelectron spectroscopy) in Abhängigkeit von der Cu-Konzentration des CIGSe untersucht. Es wurde gezeigt, dass die Cd-Diffusion in die Cu-armen Absorber ein zweistufiger Prozess ist, bei dem Cu-Atome während des Diffusionsprozesses aktiv durch Cd-Störatome ausgetauscht werden; wohingegen in der Cu-reichen Probe die Cu-Atome nicht direkt am Diffusionsprozess beteiligt werden. Darüber hinaus wurde beobachtet, dass Cd-Atome nach einem Temperprozess bis zu 400 °C durch eine niedrigere Aktivierungsenergie aus dem oberflächennahen Bereich von Cu-armen Probe vollständig verschwunden sind; wohingegen eine kleine Menge von Cd innerhalb der gleichen Tiefe der Cu-reichen Probe nach dem gleichen Temperprozess gemessen werden konnte. Ein weiterer Unterschied in der Grenzflächenbildung von Cu-armen und Cu-reichen CIGSe/CdS-Proben beim Tempern wurde gefunden: Eine Ga-Diffusion in Richtung der CIGSe Oberfläche. Im Gegensatz zur Cu-reichen Probe wurde eine signifikante Ga-Diffusion bei erhöhten Temperaturen im Falle der Cu-armen Proben beobachtet.

Zweitens wurden die Auswirkungen der KF-PDT (engl. post-deposition treatment) von CIGSe auf die CIGSe/CdS-Grenzfläche mittels tiefenaufgelöster HAXPES untersucht. Neben einer starken Vermischung an der Grenzfläche wurde eine erhöhte Cu-Verarmung aufgrund der KF-PDT in Kombination mit einer erhöhten Akkumulation von Cd und S beobachtet. Eine Verschiebung des CIGSe-Valenzbandes an der Oberfläche von etwa 0,15 eV zu höheren Bindungsenergien sowie der CIGSe- und CdS-bezogenen Kernniveaus wurde an der KF-behandelten Probe gemessen. Dieses Phänomen wurde den Auswirkungen von zusätzlichem Cadmium zugeschrieben, das als Donator wirkt und weitere Elektronen in das Leitungsband des Absorbers freisetzt. Dann akkumulieren die Elektronen an der CdS-Oberfläche, nachdem sie den Grenzflächenbereich passiert haben. Diese zusätzliche Oberflächenladung führt zu einer deutlichen Verschiebung der Photoemissionsspektren, wie sie auf dem KF-behandelten CIGSe-Absorber im Vergleich zum unbehandelten Absorber beobachtet wird.

1 Introduction

The world population is growing and correspondingly demand for energy is steadily rising. Currently, most of the available energy is generated from coal, oil and gas. When these so-called fossil fuels are burned during the production of the electricity, they emit large amounts of CO_2, which is one of the greenhouse gases that contributes to global warming. One way to fight against the global warming is to turn our interest into clean and renewable energies as an alternative to fossil fuels.

Photovoltaic devices, which directly convert the sun light into electricity, are some of the most promising renewable energy sources [1]. Nowadays, silicon-based solar cell devices dominate the photovoltaic market [2]. However, thin film solar cells based on $Cu(In,Ga)Se_2$ (CIGSe) chalcopyrite are among the most promising candidates to provide low-cost solar electricity because of their long-term stability [3], high efficiency [4], low energy pay-back time [5] and flexibility in the device design [6]. Indeed, thin film solar cells based on polycrystalline CIGSe absorbers have reached a maximum conversion efficiency of 22.8 % on the laboratory scale, already exceeding the efficiencies of solar cells based on polycrystalline silicon [7].

With 22.8 % conversion efficiency, CIGSe-based solar cells present the best efficiencies among thin film devices [7]. Although the CdS buffer layer is widely accepted to be leading to the best efficiencies, the latest record conversion efficiency has been achieved by the use of a Cd-free Zn(O,S,OH) buffer layer [7]. This achievement encourages the replacement of the CdS buffer layer without efficiency loss, as the usage of Cd-containing compounds in electronic devices is undesired because of its toxicity. However, state of the art CIGSe thin film devices still contain a thin layer of CdS and they are widely used as a reference material for the evaluation of their Cd-free counterparts. Therefore, the investigation of CdS containing structures is still a current topic of

research, which could help to shed light on the unknown device properties and thus open new ways to enhance the efficiencies of any kind of CIGSe-based solar cells.

The first aim of this thesis is to investigate the properties of the CIGSe/CdS interface, which plays a crucial role in the achievement of high conversion efficiencies in the CIGSe-based thin film solar cells.

Another feature of the current record CIGSe solar cell is that a KF post-deposition treatment (KF-PDT) is applied on the CIGSe film under a Se atmosphere. After the achievement of the record efficiency of 20.4 % for the first time by the usage of KF-PDT [8], it has been leading to further improvements in the efficiencies. Investigation of the impact of the KF-PDT on the CIGSe/CdS interface is the second aim of this thesis.

This work is organized as in the following:

The theoretical background for the scientific interpretation of the experimental results of this work is given in Chapter 2 and Chapter 3:

Chapter 2 covers the basic material properties of $Cu(In,Ga)Se_2$ and CdS compounds. It starts with a brief description of the structure of a CIGSe-based chalcopyrite thin film solar cell. This is followed by a review of the fundamental features of the CIGSe absorber materials, including their crystal structure, phase diagram, defects, and their band gap dependency on the composition. The heterocontact formation between the absorber layer and the CdS buffer layer is then presented with an energy band diagram. The role of the chemical bath deposited CdS buffer layer and the KF post-deposition treatment of the CIGSe layer are briefly discussed in the last part of the Chapter 2, which helps later to interpret the experimental results.

Chapter 3 describes the experimental methods that are used within this thesis. It starts with the presentation of the sample preparation methods for the CIGSe absorber layer by a three-stage coevaporation process and for the CdS buffer layer by chemical bath deposition. This is followed by a detailed description of all samples that are investigated in this work. Finally, sample characterization methods, such as (standard and hard) x-ray and ultraviolet photoelectron spectroscopies, as well as their experimental setups are described.

The experimental results of this thesis are given in Chapter 4 and Chapter 5:

Chapter 4 discusses the differences in the Cd diffusion from chemically deposited CdS into the $Cu(In,Ga)Se_2$ films depending on their Cu concentration. The motivation for this chapter is given with DFT calculations on the Cd diffusion into Ga-free $CuInSe_2$ and $CuIn_5Se_8$, as well as their Ga-containing counterpart materials; where distinguished mechanisms as well as corresponding activation energies for the Cd diffusion in both cases are theoretically calculated [9–11]. The DFT calculations were carried out by the ComCIGS-II project partners J. Kiss and H. Mirhosseini from the Max-Planck-Institute for Chemical Physics of Solids. The experimental proof of the theoretical calculations is performed by means of hard x-ray photoelectron spectroscopy on two differently grown CIGSe+CdS samples with the relative Cu concentrations of [Cu]/([In]+[Ga])=0.80 and 0.95, respectively. Although both absorbers have a Cu-poor composition, they are labeled in Chapter 4 as Cu-poor for [Cu]/([In]+[Ga])=0.80 and Cu-rich for [Cu]/([In]+[Ga])=0.95 to indicate the differences in the relative Cu concentrations.

Chapter 5 deals with the experimental results on the impact of the KF post-deposition treatment (KF-PDT) of the CIGSe film on the interface formation between the CIGSe and the CdS heterojunction partners. Compositional and electronic depth-profile analyses, including the interface region, of CIGSe+CdS and CIGSe+KF+CdS samples are performed using HAXPES. In order to distinguish the effect of the CdS on the surface properties of the CIGSe from the effect of the KF-PDT, the uncovered CIGSe and CIGSe+KF samples are investigated as well using standard XPS and UPS. In addition, the results of the variation of the surface chemistry and electronic properties due to the KF-PDT are discussed.

Finally, **Chapter 6** gives a summary of the theoretical and the experimental results on the atomic interdiffusion at the $Cu(In,Ga)Se_2$/CdS interface, and the impact of the KF post-deposition treatment of the CIGSe film on the interface formation at the CIGSe/CdS heterostructure.

2 Material Properties of $Cu(In,Ga)Se_2$ and CdS Compounds

In this chapter, the stacked layer structure of Mo/$Cu(In,Ga)Se_2$/CdS/i-ZnO/ZnO:Al thin film solar cells is first briefly presented. The focus is then directed onto the material properties of the $Cu(In,Ga)Se_2$ (CIGSe) absorber films; including their crystal structure, their phase diagram, defects in CIGSe films and their composition-dependent band gap energy. This is followed by the description of the basic material properties of the CdS buffer layer. Then, the electronic band diagram of a CIGSe-based thin film solar cell is presented. Finally, the role of a chemical bath-deposited CdS buffer layer in the stacked layer structure and the effect of a KF post-deposition treatment on the CIGSe-based solar cells are briefly described.

2.1 Structure of CIGSe-Based Thin Film Solar Cells

This section deals with the stacked layer structure of Mo/$Cu(In,Ga)Se_2$/CdS/i-ZnO/ZnO:Al thin film solar cells. Figure 2.1 depicts (a) a schematic view of the stacked layer sequence of a CIGSe-based thin film solar cell with the various components and (b) a SEM cross-section image of a real CIGSe solar cell.

Soda lime glass is typically used as a substrate with a thickness of about 2 mm. The substrate is coated with a ~500 nm thick molybdenum film by sputtering. The Mo layer serves as a back contact. The CIGSe chalcopyrite absorber is deposited on top of the back contact by means of a three-stage coevaporation process (see Section 3.1.1 for details). The thickness of the absorber layer is about 2 μm.

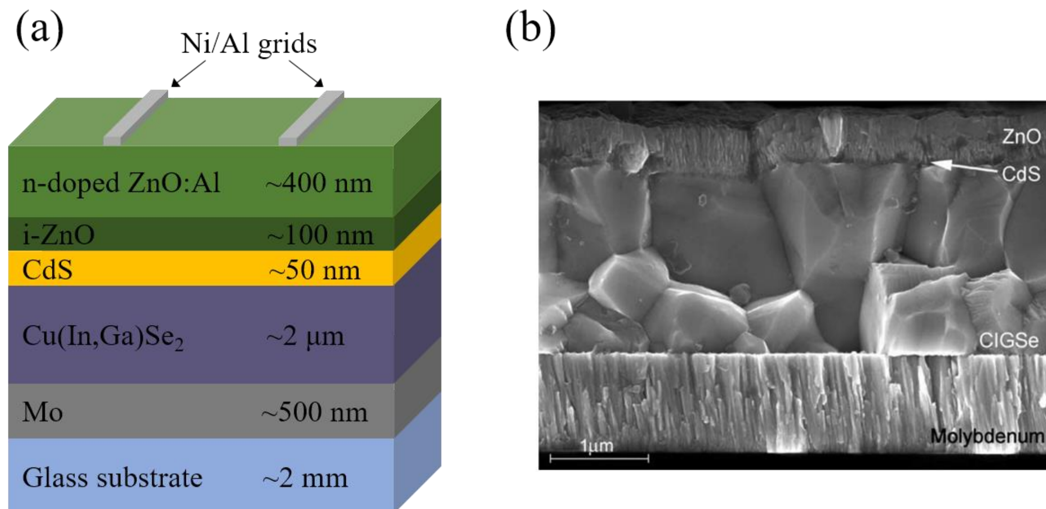

Figure 2.1 (a) Schematic and (b) SEM cross section view image (from [12]) of a CIGSe-based thin film solar cell.

The so-called buffer layer CdS is deposited on top of the CIGSe by means of chemical bath deposition (CBD). Details on the CdS deposition process is given in Section 3.1.2. The thickness of the CdS layer is approximately 50 nm. Although the state of the art CIGSe thin film solar cells contain CBD-CdS buffer layers, alternative buffer layers together with different deposition techniques are intensively investigated [13]. The main function of the buffer layer is to provide a favorable band alignment at the absorber/window interface. This is for instance done by the Cd diffusion from the buffer layer into the absorber, which converts the absorber surface from p to n-type [14,15].

The p-n junction is formed between the p-type CIGSe absorber and the n-type CdS buffer layer together with an n-type double window layer of ZnO, which consists of a thin layer of intrinsic ZnO and highly doped Al:ZnO with the thicknesses of about 100 nm and 400 nm, respectively. The double window ZnO layer, which is sputter-deposited on top of the CdS buffer layer, serves as a transparent conductive oxide (TCO) and permits the incoming light to pass through and to reach the underlying absorber film. A Ni-Al grid is evaporated on top of the window layer and provides the front contact of the device.

2.2 Crystal Structure of CIGSe

The $Cu(In,Ga)Se_2$ (CIGSe) compound crystallizes in a tetragonal chalcopyrite structure [16,17]. It is a ternary I-III-VI_2 compound, which consists of a group I element (Cu), group III elements (In, Ga) and a group VI element (Se). The group number III is used in Chapter 4 and Chapter 5 to abbreviate In+Ga elements, where the Cu and Ga concentrations are defined with respect to the group III elements as Cu/III and Ga/III, respectively.

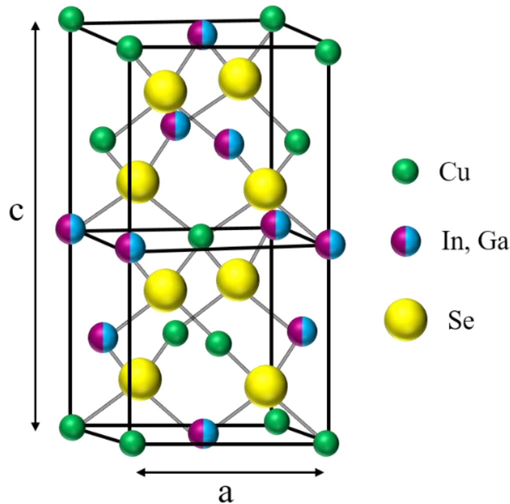

Figure 2.2 Chalcopyrite unit cell of a $Cu(In,Ga)Se_2$ compound with the lattice parameters of a and c. Cu, In (or Ga) and Se atoms are presented by green, purple (or blue) and yellow spheres, respectively.

The unit cell of the tetragonal chalcopyrite structure is shown in Figure 2.2. This crystal structure can be derived from the cubic sphalerite (zincblende) by doubling the unit cell [18]. In this structure, each Cu and In/Ga atom is coordinated to four Se atoms, whereas each Se atom is coordinated to two Cu and two In/Ga atoms in a tetrahedral way. In this compound, Cu and In/Ga metals are denoted as cations, whereas Se atoms are denoted as anions. In contrast to the zincblende structure, the different bonding lengths between the cations and group VI anions cause a distortion of the lattice constants a and c [17]. The ratio of the lattice constants c/a is 2 for an undisturbed crystal structure and varies linearly with the Ga content x, with the relation $a(x)=(-0.17x+5.782)$ Å and $c(x)=(0.589x+11.619)$ Å [19,20].

2.3 Phase Diagram of CIGSe

The possible phases in the Cu-In-Se system are indicated in the ternary phase diagram in Figure 2.3-(a). Thin films of Cu-In-Se prepared under an excess supply of Se, that is, normal conditions for thin film growth of $Cu(In,Ga)Se_2$, have compositions that fall on, or close to, the tie-line between Cu_2Se and In_2Se_3. The chalcopyrite $CuInSe_2$ is located on this tie-line as well as a number of phases called ordered defect compounds (ODC), because they have a lattice structure described by the chalcopyrite structure with an ordered insertion of intrinsic defects [21].

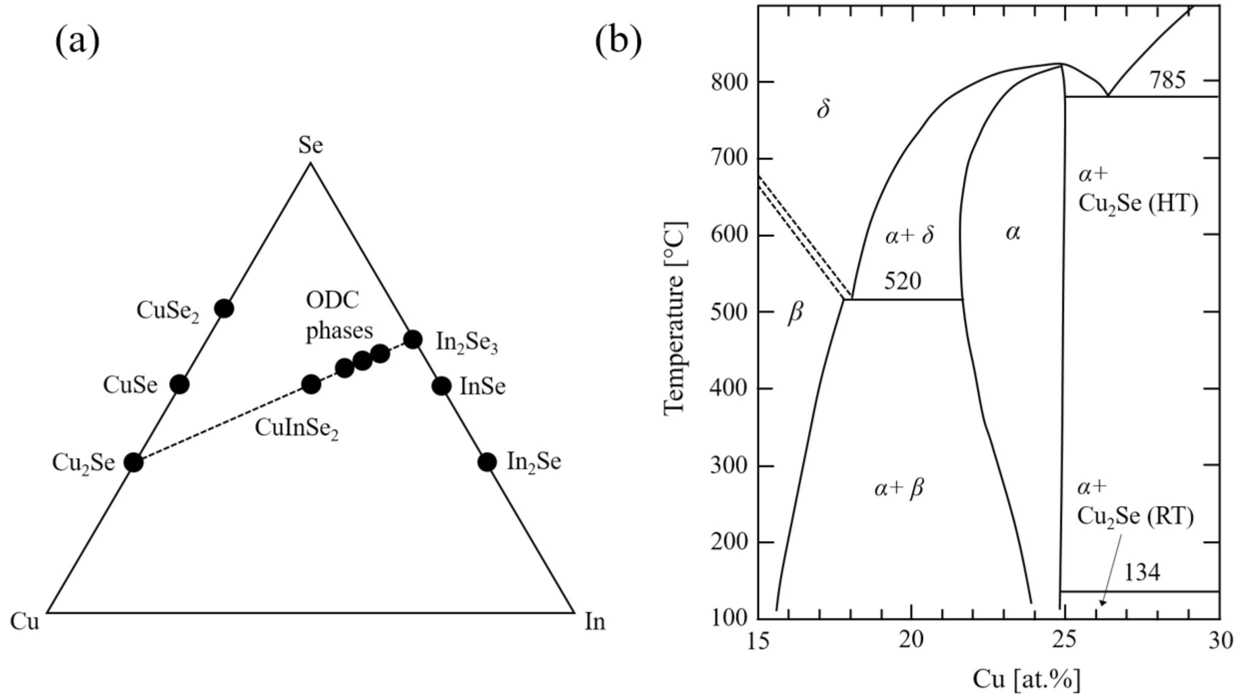

Figure 2.3 (a): Ternary phase diagram of the Cu-In-Se system. Thin film composition is usually near the pseudobinary Cu_2Se-In_2Se_3 tie-line (taken from [21]). (b): Pseudobinary In_2Se_3-Cu_2Se equilibrium phase diagram for compositions around the $CuInSe_2$ chalcopyrite phase, denoted α. The δ-phase is the high-temperature sphalerite phase, and the β-phase is an ordered defect phase (ODC). Cu_2Se exists as a room-temperature (RT) or high-temperature (HT) phase [21,22].

Figure 2.3-(b) displays a phase diagram of the $CuInSe_2$ along the Cu_2Se–In_2Se_3 pseudo binary section as a function of Cu concentration and temperature [22]. The diagram is given between the Cu concentration of 15 at.% and 30 at.%, where a Cu concentration of 25 at.% corresponds to

[Cu]/[In]=1. The Greek letter α in the Figure 2.3-(b) labels the chalcopyrite type $CuInSe_2$ phase, whereas β and δ represent the ODC phase and the high temperature sphalerite phase, respectively. The α-phase exists as a single phase for Cu concentrations between ~23 at.% and ~25 at.% for temperatures up to ~800 °C. This implies that in the corresponding temperature regime, the chalcopyrite structure (α) remains as a single phase with a Cu concentration tolerance of about 3 at.%, resulting in significantly Cu-poor CISe compounds.

The single α-phase field for $CuInSe_2$ at low temperatures is relatively narrow and does not contain the composition 25 at.%. At higher temperatures, around 500 °C, where CIGSe thin films are usually grown, the phase field widens toward the In-rich side. Typical average compositions of device-quality films have Cu-poor compositions with 22 to 24 at.% Cu, which fall within the single-phase region at growth temperature.

For a Cu content between ~16 at.% and ~23 at.%, the α-phase coexists with a β-phase, which represents the ODC with the composition of $CuIn_3Se_5$ [23]. Although the β-phase consists of Cu vacancies V_{Cu} and antisite defects In_{Cu} [24], it crystallizes in a similar structure as the α-phase. For a Cu content below ~16 at.%, the β-phase is stable as a single phase.

For the experimental investigations in this work, three types of CIGSe films are used. They are named as Cu-rich CIGSe, Cu-poor CIGSe and standard CIGSe (for details see Section 3.1.3). The Cu-rich CIGSe film is prepared with a bulk [Cu]/([In]+[Ga]) (CGI) ratio of 0.95, which corresponds to a Cu concentration of ~24 at.%. Considering the phase diagram in Figure 2.3-(b), the Cu-rich CIGSe film consists of a single α-phase. On the other hand, the Cu-poor CIGSe film is grown with a bulk CGI ratio of 0.80, which corresponds to a Cu concentration of ~21 at.%. Figure 2.3-(b) implies that the Cu-poor CIGSe film consists of two phases (i.e. $Cu(In,Ga)Se_2$ and $Cu(In,Ga)_3Se_5$). Finally, the standard CIGSe film has a bulk CGI ratio of 0.88, which is equivalent to a Cu concentration of ~23 at.%. Although its Cu concentration slightly deviates from the stoichiometric composition of $Cu(In,Ga)Se_2$, Figure 2.3-(b) indicates that the standard CIGSe film still consists of a single α-phase.

2.4 Defects in CI(G)Se

$Cu(In_{1-x},Ga_x)Se_2$ (CIGSe) is a p-type semiconductor and its p-type character is governed by intrinsic defects. Although a number of intrinsic defects exist in CIGSe, some of the most relevant intrinsic defects in CIGSe together with the Cd_{Cu} extrinsic defect are listed in Table 2.1.

Table 2.1 Some relevant intrinsic and extrinsic point defects in the ternary compounds $CuInSe_2$ and $CuGaSe_2$. The type indicates the electronic character of the corresponding defect (A: acceptor, D: donor). Defect transition energies of divalent donors (+/0) and acceptors (0/−) in CGSe and CISe relative to the CBM, E_C, for the donors and to the VBM, E_V, for the acceptors are adapted from [25,26]. The formation enthalpies ΔH of the neutral defects in CISe and CGSe are taken from [25,26].

Defect	Type	$Energy^{CISe}$[eV]	$Energy^{CGSe}$[eV]	ΔH^{CISe}[eV]	ΔH^{CGSe}[eV]
V_{Cu}	A	E_V+0.03 [25]	E_V+0.01 [25]	0.60 [25]	0.66 [25]
V_{III}	A	E_V+0.17 [25]	E_V+0.19 [25]	3.04 [25]	2.83 [25]
Cu_{III}	A	E_V+0.29 [25]	E_V+0.29 [25]	1.54 [25]	1.41 [25]
III_{Cu}	D	E_C−0.25 [25]	E_C−0.49 [25]	3.34 [25]	4.42 [25]
Cu_i	D	E_C−0.20 [25]	E_C−0.21 [25]	2.88 [25]	3.38 [25]
Cd_{Cu}	D	E_C−0.00 [26]	E_C−0.06 [26]	−0.90 [26]	−0.51 [26]

The formation enthalpy of the listed point defects shows a dependence on the Ga to In ratio (x). The lowest formation enthalpy of the Cu vacancies V_{Cu} among the intrinsic defects implies that the V_{Cu} is the dominant defect within the CIGSe. The acceptor-like type of the V_{Cu} defect (energy position close to valence band) is responsible for the intrinsic p-type conductivity of the CIGSe. In case of Cu-poor grown CIGSe, V_{Cu}^- acceptors easily form a neutral defect pair $2V_{Cu}^-+In_{Cu}^{2+}$ together with In_{Cu}^{2+} donors [24]. This indicates that the neutral CIGSe can be obtained even for non-stoichiometric composition due to a high degree of self-compensation of point defects. However, a small excess of V_{Cu} acceptors due to the low formation enthalpy results in p-type doping of the CIGSe.

The negative formation enthalpy of the Cd_{Cu} extrinsic donors indicates that it can form rather easily due to the Cd diffusion into CIGSe when the CdS buffer layer is deposited on top of the CIGSe. The Cd diffusion into CIGSe, thus the formation of Cd_{Cu} defects is considered to be the reason for the type inversion (from p-type to n-type) of the CIGSe surface [8,27,28].

Zhang et al. [29] calculated the intrinsic defects in $CuInSe_2$ (CISe). A summary of their results is schematically shown in Figure 2.4 including additionally the defect transition energy of Cd extrinsic defects, calculated by Persson et al. [26].

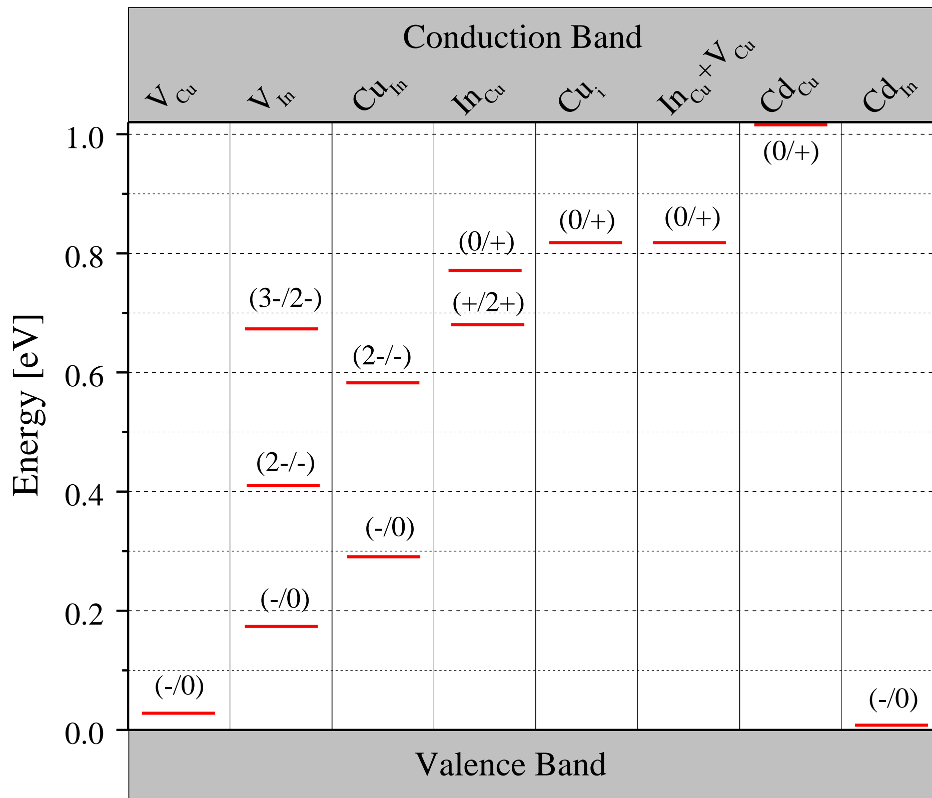

Figure 2.4 Defect transition energy levels of some intrinsic and extrinsic defects in $CuInSe_2$ (adapted from [26,29]). The corresponding charge states for the transitions are indicated in parentheses.

The most shallow intrinsic defect level in CISe is formed by the V_{Cu} acceptor defect with $E(-/0)=E_V+0.03$ eV. As this defect also has a low formation enthalpy at Cu-poor composition (see Table 2.1), it appears to be responsible for p-type doping [30]. The In vacancy (V_{In}) is the next deeper acceptor level at $E(-/0)=E_V+0.17$ eV. All the other defect levels are relatively deep,

including the two V_{In} acceptor levels at 0.41 eV and 0.67 eV above the valence band E_V, respectively. The Cu_{In} antisite has two deep acceptor levels at 0.29 eV and 0.58 eV above E_V. In addition, the In_{Cu} antisite defect with two energy levels at 0.25 eV and 0.34 eV, and the Cu_i interstitial defect with one level at 0.20 eV below the conduction band E_C appear as the deep donors. Persson et al. [26] calculated the transition energy levels for Cd_{Cu} donors and Cd_{In} acceptors at $E(0/+)=E_C-0.00$ eV and $E(-/0)=E_V+0.00$ eV, respectively.

Wei et al. [25] calculated the effect of the Ga concentration on the defect properties and they found that the acceptor levels remain almost the same for the $CuInSe_2$ (CISe) and the $CuGaSe_2$ (CGSe) compounds (see Table 2.1). However, donor levels are deeper in CGSe compound. Persson et al. [26] showed a trend that CGSe has somewhat deeper Cd_{Cu} donors than CISe, and this trend is more pronounced for Cd_{In} acceptors.

2.5 Band Gap Energy of $Cu(In_{1-x},Ga_x)Se_2$

$Cu(In_{1-x},Ga_x)Se_2$ (CIGSe) is a direct band gap semiconductor [31]. The band gap energy E_g of CIGSe can be tuned from ~1.0 eV of $CuInSe_2$ (i.e. x=0) to ~1.7 eV of $CuGaSe_2$ (i.e. x=1) by changing the Ga concentration [32]. The band gap energy of CIGSe can be expressed as a function of x [33]:

$$E_g = (1-x)E_g(CuInSe_2) + xE_g(CuGaSe_2) - bx(1-x) \quad (2.1)$$

where b refers to the “bowing coefficient” and takes values between b=0.15 eV and 0.24 eV [34], x corresponds to the Ga concentration, $E_g(CuInSe_2)\approx1.04$ eV [35,36] and $E_g(CuGaSe_2)\approx1.65$ eV [36].

The band gap energy of the CIGSe as a function of Ga concentration ratio ([Ga]/[In]+[Ga] or x) is shown in Figure 2.5, demonstrating that the variation in E_g is related to a variation in conduction band minimum (CBM or E_C).

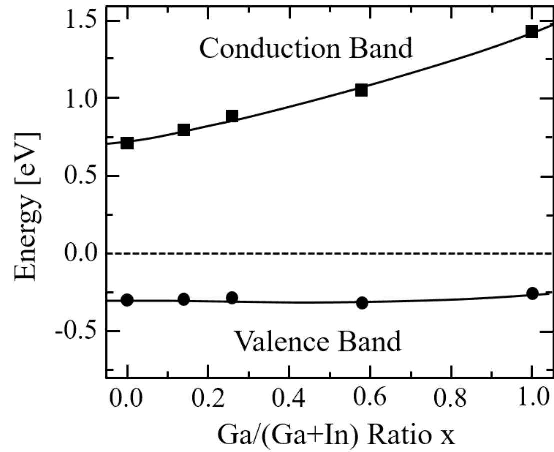

Figure 2.5 The band gap energy of $Cu(In_{1-x},Ga_x)Se_2$ as a function of Ga/(In+Ga) atomic ratio x. The dependence of the valence band energy E_V and the conduction band energy E_C on the Ga ratio x [37].

It is shown in Figure 2.5 that the valence band maximum (VBM or E_V) is not influenced by the variation of Ga concentration [37]. This is due to the fact that the CBM consists of the In/Ga *s*,*p* orbits and the VBM consists of hybrid orbitals of Cu-*d* and Se-*p* [29]. This means that a variation in the Cu concentration would influence the position of the E_V and thus the band gap energy E_g. The strong repulsion of the Cu-*d* and Se-*p* orbitals pushes the VBM towards the conduction band and results in a lower band gap energy [38]. Therefore, a reduction of the Cu content leads to an increase in E_g by lowering the *p*-*d* repulsion [39]. As a result, the CIGSe compounds with a high amount of Cu vacancies V_{Cu} exhibit a higher band gap energy [38,40,41].

2.6 Basic Properties of CdS

CdS is a binary II-VI group compound semiconductor. It crystallizes in a hexagonal wurtzite structure or in a cubic zinc blende structure with lattice parameters *a*=4.137 Å, *c*=6.716 Å and *a*=5.825 Å, respectively [42]. However, the most common form is the hexagonal wurtzite structure [43]. CdS is an n-type semiconductor and has a direct band gap of 2.42 eV, giving it a transparent, sunny yellow appearance [44].

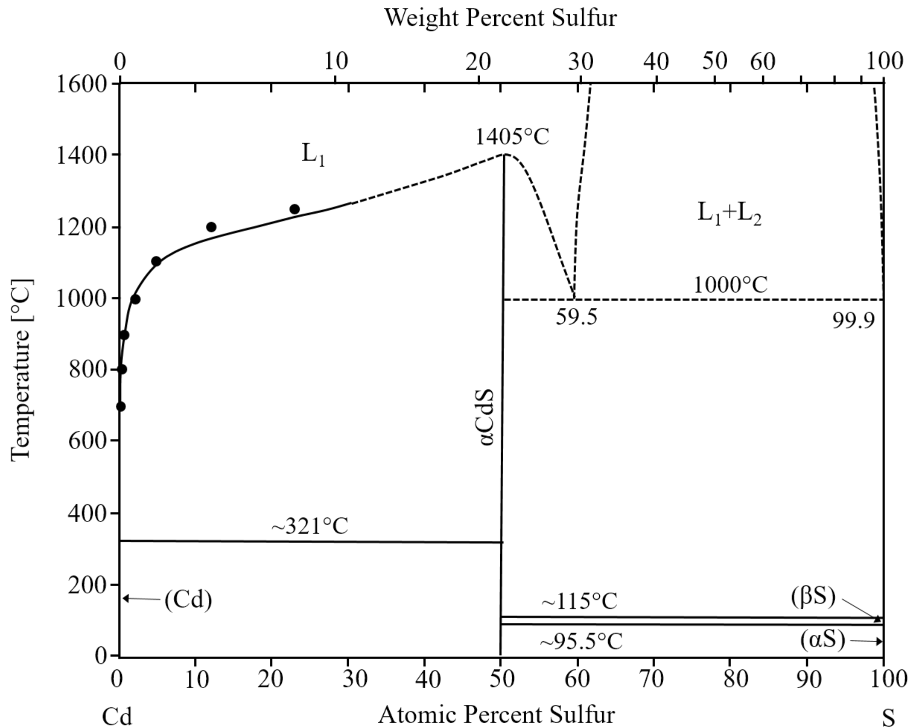

Figure 2.6 Assessed phase diagram of Cd-S as a function of sulfur concentration and temperature (taken from [45]. Symbols are experimental points from [46].

The assessed phase diagram of Cd-S system is given in Figure 2.6. In the Cd-S system, αCdS has essentially the stoichiometric composition with 50 at.% S and melts congruently. The melting point of αCdS is in the order of 1405 °C [47]. The detailed explanation of the phase diagram in Figure 2.6 can be found in [45]. Nevertheless, the abovementioned basic information on the phase formation of CdS as a function of temperature will be revisited in Chapter 4, where the annealing-assisted diffusion of Cd into CIGSe is discussed.

2.7 Electronic Band Diagram of CIGSe-Based Thin Film Solar Cell

Figure 2.7 shows a schematic band diagram of a CIGSe-based thin film solar cell. The band diagram is determined by the electron affinities χ (energy difference between the conduction band minimum CBM and the vacuum level E_{vac}), Fermi levels and the band gap energies [48]. Because of the large band gap energies of the ZnO window layer and the CdS buffer layer (~3.3 eV and 2.4 eV, respectively) most of the light is transmitted to the CIGSe layer without being absorbed in the

window layer. The band gap energy of the CIGSe absorber is strongly influenced by its composition and has a strong impact on the band discontinuities.

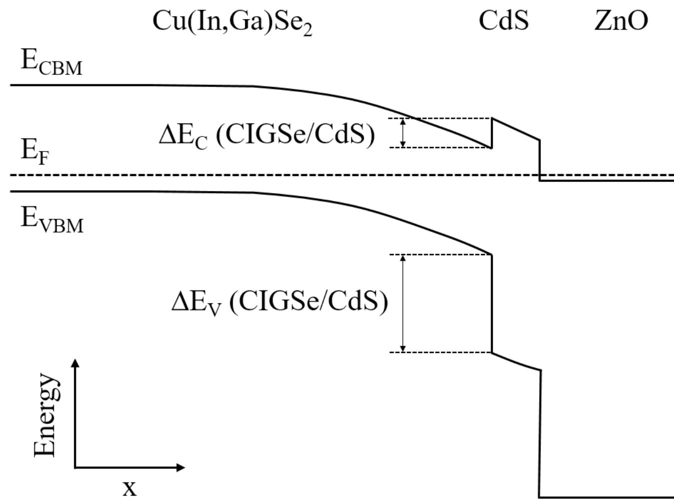

Figure 2.7 Schematic electronic band diagram of a $Cu(In,Ga)Se_2$-based thin film solar cell including the valence band maximum E_{VBM}, the Fermi energy E_F and the conduction band minimum E_{CBM}.

Band discontinuities occur at the interfaces due to the differences in the position of the valence and conduction bands of the corresponding layers with respect to the Fermi level. The band discontinuities at the absorber/buffer interface play a crucial role in the carrier transport, thus the performance of the solar cell. The presence of a spike-like ΔE_C (CBM of the CdS is energetically higher than that of the CIGSe) between the values 0 eV-0.4 eV is reported to be beneficial by reducing the recombination of the electron-hole pairs at the CIGSe/CdS interface [49,50]. However, the formation of a cliff-like ΔE_C (CBM of the CdS is energetically lower than that of CIGSe) is undesirable due to the reduction of the energy barrier for the carrier recombination at the interface [51].

2.8 The Role of CBD-CdS Buffer Layer

The deposition of a thin CdS buffer layer by chemical bath deposition (CBD) between the CIGSe absorber and the ZnO window layer is an important step to produce high efficiency solar cells [52]. One of the most important features of the CBD-CdS is the etching of the CIGSe surface oxides in

the chemical bath prior to the CdS formation [53]. The surface coverage of the CBD-CdS is satisfactory even within the early stage of the CBD, corresponding to the deposition of a few nanometers of CdS [54]. The good coverage of the CIGSe surface by CdS could help to protect the CIGSe surface from sputtering damage during the ZnO deposition.

It has been proposed that the deposition of CdS may lead to a reduction of defects at the interface [55,56]. It can be also beneficial on the band alignment between the absorber and window layers [57]. The formation of a spike-like conduction band offset was reported between 0.3 eV and 0.7 eV [58,59], which could help to reduce the recombination of charge carriers at the CIGSe/CdS interface.

It has been observed that Cd may diffuse into the absorber during the chemical bath deposition and may result in an n-type inversion at the absorber surface [3,52,60–62]. The diffusion of Cd atoms into the CIGSe absorber upon the Cu concentration is the subject of the Chapter 4 of this thesis.

2.9 The Effect of KF Post-Deposition Treatment

Incorporation of sodium into the absorber is known to play an important role for the performance optimization of the $Cu(In,Ga)Se_2$ (CIGSe)-based thin film solar cells. The beneficial effect of Na incorporation on the conversion efficiency was first reported more than twenty years ago [63]. Since that, many research groups published a number of studies on the role of the Na (some examples: [64–69]). However, the main effect of it is still not fully understood. On the other hand, the effect of different alkali metals (Li, Na, K, Rb and Cs) as well as their fluoride compounds on the CIGSe absorber has been widely studied theoretically and experimentally by different research groups [70–74]. After the achievement of a world record conversion efficiency of a KF treated CIGSe-based thin film solar cell grown on a flexible substrate by Chirilă et al. [8], the new research interest turned on the investigation of the effect of the KF treatment on the CIGSe absorbers. Some of the possible effects of the KF treatment are summarized in Chapter 5 as a motivation to that chapter, where the influence of the KF on the formation of CIGSe/CdS interface is investigated.

3 Sample Preparation and Characterization Methods

The materials that are subject to investigation in this work are $Cu(In,Ga)Se_2$ (CIGSe) absorber materials and CdS buffer layers. In this chapter, first, the preparation techniques of the CIGSe films by a three-stage coevaporation method and the CdS layer on top of the CIGSe by chemical bath deposition (CBD) are briefly described.

As the surfaces of the CIGSe films as well as the interface at CIGSe/CdS are studied by means of x-ray and ultraviolet photoelectron spectroscopies (XPS and UPS, respectively), then, the fundamentals of the characterization techniques are shortly explained. The more profound details on the XPS and UPS can be found in references [75–80].

In addition, the experimental setups for the XPS and UPS measurements are presented.

3.1 Preparation of $Cu(In,Ga)Se_2$ Thin Films and $Cu(In,Ga)Se_2$/CdS Heterostructures

The preparation methods of the CIGSe films by the three-stage coevaporation process as well as their post treatments by KCN and KF, additionally CBD technique for the deposition of the CdS as a heterocontact partner of the CIGSe are briefly described in the following. The detailed description of the samples under investigation is given in the end of this section.

3.1.1 $Cu(In,Ga)Se_2$ Absorber Films: Growth and Post Treatments

The photovoltaic absorbers that are investigated in this work are polycrystalline $Cu(In,Ga)Se_2$ (CIGSe) thin films with a thickness of approximately 2 µm. They are grown on molybdenum coated soda-lime glass (SLG) substrates using a three-stage process [12,81,82]. The three-stage process is a coevaporation process under vacuum conditions (basis pressure: 10^{-7} mbar), where the production of the CIGSe layer is based on the temperature-induced interdiffusion of the evaporated elements.

The deposition rate of the individual elements is controlled with optical real-time methods, where the scattering of the laser light is used [12]. The three-stage coevaporation process is schematically described in Figure 3.1.

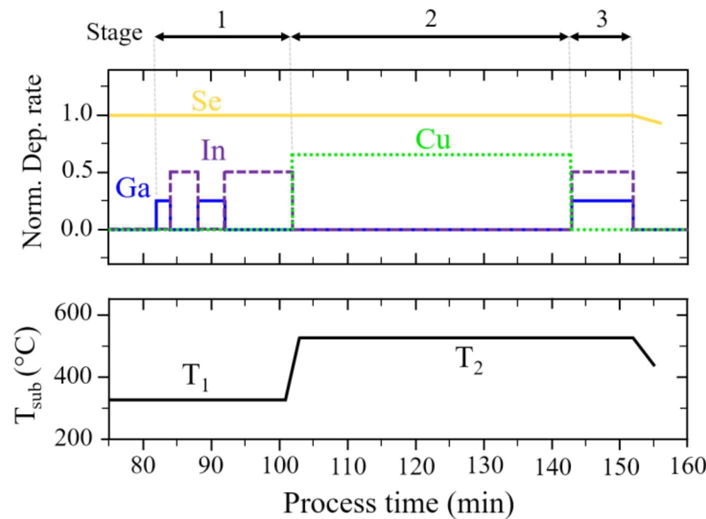

Figure 3.1 Schematic description of the three-stage process. Below: the course of the substrate temperature. Above: deposition rates of individual elements normalized to selenium [19], (after [12,82])

In the first stage of the process, In and Ga are deposited sequentially at a substrate temperature of 330 °C to form an (In,Ga)-Se precursor layer, while the whole process occurs under Se atmosphere at a basis pressure of about 10^{-7} mbar. In the second stage, Cu and Se are provided at an elevated substrate temperature of 525 °C, where the shutters of the In and Ga sources are closed. The chalcopyrite phase is formed in this second stage because of the Cu diffusion in the (In,Ga)-Se precursor layer. The stoichiometric composition is obtained at the end of the second stage, where the integral composition of [Cu]/([In]+[Ga]) (CGI) is approximately 1. After reaching the

stoichiometric composition, the further evaporation of Cu and Se is responsible for the formation of Cu-Se secondary phases during the second stage, which segregate on the surface of the layer during the growth process. During the third stage, only In and Ga are provided simultaneously under Se atmosphere to form Cu-poor material with a composition ratio of CGI=0.80-0.90, which is the optimum concentration interval for high efficiency CIGSe solar cells, at least in our lab, therefore denoted as *standard absorber*. In addition to the Cu-poor content of the material, the Ga concentration with ratio of [Ga]/([In]+[Ga]) (GGI)=0.27-0.36 is desired for high efficiencies [82,83].

The integral Cu concentration of the CIGSe film in the three-stage process is controlled with the duration of the second and third stages. The evaporation of In, Ga and Se beyond the stoichiometric composition (i.e. 1-1-2 composition) of the compound in the third stage results in a Cu-poor CIGSe absorber, whereas by shortening the third stage accordingly, relatively Cu-rich absorbers can be also produced. The Cu-poor and Cu-rich samples that are investigated within Chapter 4 are prepared by this method.

Potassium fluoride post-deposition treatment (KF-PDT)

Within the Chapter 5, the impact of potassium fluoride post-deposition treatment (KF-PDT) on the interface properties of CIGSe/CdS material system is investigated since this post-treatment approach improves the photovoltaic performance in CIGSe PV technology [7]. For this purpose, a KF-PDT is applied on a standard CIGSe absorber. The KF-PDT is performed in a separate UHV evaporation chamber for 20 min at a substrate temperature of 330 °C in the presence of KF and Se molecular beams, which were the PDT conditions for the record efficiency solar cell at the time of the experiment [8].

KCN etching of the CIGSe films

The KCN-etching is well known to be used in preparing well-defined CIGSe films. It removes surfaces oxides (e.g. Ga_2O_3, In_2O_3) and sodium from the surface away [84,85]. It has no major effect on the solar cell efficiency of Cu-poor grown samples [12] or leads to improvements in some cases [86,87]. In case of Cu-rich grown samples, the usage of KCN-etching before the chemical bath deposition of CdS is necessary in order to remove copper-selenide phases from the surface

[88–90]. The KCN-etching does not affect the chalcopyrite phase and it has no influence on the surface composition of Cu-poor grown samples [88,90,91].

The CIGSe samples that are used in Chapter 4 are etched in a 10 % KCN containing aqueous solution for three minutes at room temperature. They are then rinsed with deionized water and dried in a nitrogen gas stream. Finally, they are either rapidly transferred to the corresponding UHV based analysis system for XPS-UPS measurements using a small transport box flooded with nitrogen or they are further processed in a wet chemical bath for the CdS deposition.

3.1.2 Chemical Bath Deposition of the CdS

The most established buffer layer in high efficiency CIGSe PV technology is CdS [92]. In this work, the CdS buffer layer is deposited (as commonly done) by a chemical bath deposition (CBD) technique. The experimental setup for the CBD is schematically illustrated in Figure 3.2.

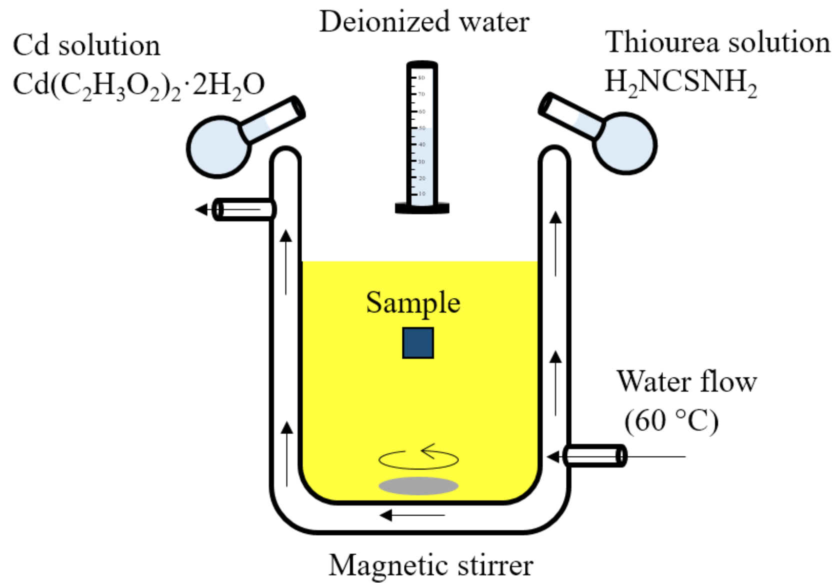

Figure 3.2 Schematic illustration of the experimental setup for the chemical bath deposition of CdS.

Before starting the deposition process, Cd and thiourea solutions are prepared. For this purpose, 0.44 g of cadmium acetate dihydrate ($Cd(C_2H_3O_2)_2{\cdot}2H_2O$) salt is mixed with ammonium hydroxide solution (25 %) to a total volume of 100 ml. This 0.02 M solution is used as a Cd source in the

CBD. Additionally, a thiourea solution is prepared by mixing 7.08 g of thiourea (H_2NCSNH_2) together with deionized water to a total volume of 100 ml. This 0.96 M solution is used as a sulfur source. Although the Cd salt is rapidly and almost spontaneously soluble in the NH_3-based solution; the special laboratory bottle, containing the thiourea solution should be shaken for a while in order to dissolve the salt in the deionized water at room temperature.

First, a clean 200 ml double-walled glass container is connected to a warm water supplier. 50 ml of deionized water is added to the glass container. Then, 11.25 ml of Cd and 30 ml of thiourea solutions are added to the water, respectively and mixed together with a magnetic stirrer. Finally, 58.75 ml of deionized water is added to the bath in order to have a total volume of 150 ml bath. The chemical bath is now basically ready for the usage but still at room temperature. During the preparation of the solution in the glass container, the temperature of the water supplier is set to 60 °C. To start the deposition process, the sample is dipped into the bath and the valve of the thermostat is opened to make the 60 °C water flow into the double-wall. The deposition time starts after opening the valve. The standard deposition time is eight minutes to obtain a complete buffer layer for standard solar cells. In this case, the thickness of the CdS layer lies between 50-60 nm. However, the samples that are investigated in Chapter 4 and Chapter 5 are dipped into the bath for less than one minute, which leads to a CdS thickness of 5-10 nm. This is a strategy to make the CIGSe substrate, CdS over layer and the corresponding interface accessible with hard x-rays. After removing the sample from the CBD bath, the sample should be immediately rinsed with deionized water and dried in a nitrogen stream.

Simultaneous ammonia etching during the CBD process

It is well known that an ammonia containing solution cleans the CIGSe surfaces by partially removing some surface oxides (e.g. Ga_2O_3, In_2O_3), although it is not as strong as KCN [27,61,85,93–95]. Since the CdS deposition in this work is done in an ammonia containing chemical bath, it is thought that the etching effect of the chemical bath due to NH_3 and the CdS deposition should occur in a competitive way, at least in the first stage of the CBD. Indeed, the first stage of the CBD with some ten seconds corresponds to the total deposition time of CdS on CIGSe samples, which are investigated in Chapter 4 and Chapter 5. To determine the ammonia etching in the chemical bath, the same bath is prepared, but now without adding the Cd and thiourea into the solution (i.e. 11.25 ml of ammonia 25 % and 30 ml of deionized water instead of Cd and thiourea

solutions). The sample is dipped into the bath for the same time as the real CBD of CdS. To have a comparable process to the real CBD process, the sample is rinsed with deionized water and dried in a nitrogen stream. Such samples are investigated in Section 5.2.

3.1.3 Detailed Description of the Samples under Investigation

The samples that are subject to investigation within this work are listed in Table 3.1 with some key properties. They are divided in three categories:

Table 3.1 List of the samples under investigation within this work.

#	Sample Name	Properties	Where
1	Cu-rich CIGSe+CdS	CGI=0.95; KCN-etched; t(CBD-CdS)=45s	Chapter 4
2	Cu-poor CIGSe+CdS	CGI=0.80; KCN-etched; t(CBD-CdS)=45s	
3	Standard CIGSe+CdS	CGI=0.88; t(CBD-CdS)=50s	Section 5.1
4	Standard CIGSe+KF+CdS	CGI=0.88; KF-20min; t(CBD-CdS)=50s	
5	Standard CIGSe	CGI=0.88	Section 5.2
6	Standard CIGSe+KF	CGI=0.88; KF-20min	
7	Standard CIGSe (CBD-etched)	CGI=0.88; CBD-etched	
8	Standard CIGSe+KF (CBD-etched)	CGI=0.88; KF-20min; CBD-etched	

Preparation of the samples #1 and #2

The CIGSe thin films are grown on molybdenum coated soda-lime glass (SLG) substrates using a three-stage coevaporation process. Details on this process are given in the previous section. The Cu content of the samples is chosen to be CGI=0.95 (sample #1) and CGI=0.80 (sample #2) (representing the Cu to In+Ga ratio) for Cu-rich and Cu-poor samples, respectively. The samples are grown on 5 cm x 5 cm large SLG substrates, which are cut down to a size of 10 mm x 10 mm and mounted on the sample holder for the subsequent HAXPES measurements. In order to remove segregated Cu_xSe or surface oxide phases, the samples are etched in a KCN-containing aqueous solution (5 %) for 3 min at room temperature. Afterwards, they are rinsed with deionized water and dried in a gaseous nitrogen stream. Thin CdS layers are then deposited on top of them by the standard CBD process, as explained in the previous section. The samples are simultaneously dipped

into the chemical bath for 45 s, leading to ultrathin CdS layers in the thickness range of less than 10 nm as estimated from the standard CdS deposition process. Finally, these samples are transferred to the UHV based analysis chamber for HAXPES measurements using a special transport box flooded with nitrogen. The samples #1 and #2 are investigated in Chapter 4.

Preparation of the samples from #3 to #8

The CIGSe thin films are prepared on molybdenum-coated soda-lime glass substrates using a three-stage coevaporation process. For the experiment in Section 5.1, two standard (Cu-poor) CIGSe samples are grown on 5 cm x 5 cm large SLG substrates with bulk compositions of [Cu]/([In]+[Ga]) = 0.88 and [Ga]/([In]+[Ga]) = 0.32, as determined by x-ray fluorescence. Directly after finishing the absorber preparation process, sample #3 was stored in nitrogen atmosphere in order to minimize the impact of air exposure, whereas on the sample #4 a KF-PDT is applied. The post-deposition treatment is performed ex-situ in a separate UHV evaporation chamber for 20 min at a substrate temperature of 330 °C in the presence of KF and Se molecular beams. Afterwards, thin CdS layers are deposited using the standard CBD process. Both samples (sample #3 and #4) are simultaneously dipped into the chemical bath for 50 s at 60 °C, leading to ultrathin CdS layers in the thickness range of less than 10 nm as estimated from the standard CdS deposition process. Afterwards, they are rinsed with deionized water and dried in a nitrogen gas stream. Prior to the wet chemical CdS deposition process, both samples are cut into small pieces of 4 mm x 8 mm size in order to be able to mount them both on one sample holder. The CIGSe+CdS and CIGSe+KF+CdS samples are then rapidly transferred to the UHV based analysis system dedicated for HAXPES using a small transport box flooded with nitrogen.

The influence of the usage of an NH_3-containing solution in the chemical bath for CdS deposition is studied in Section 5.2. For this purpose, the same samples as in the Section 5.1 (now sample #5 and sample #6) are first measured in their as-grown state without CdS layer on top (i.e. CIGSe and CIGSe+KF). The samples are then measured after a dedicated etching process in the chemical bath (i.e. CIGSe (CBD-etched) being sample #7 and CIGSe+KF (CBD-etched) being sample #8). Details on the preparation of the ammonia-containing solution can be found in the previous section.

3.2 Microstructure Characterization Methods

In order to analyze the microstructure of the CIGSe films and CIGSe/CdS-heterostructures, x-ray photoelectron spectroscopy and ultraviolet photoelectron spectroscopy were applied. Theoretical background, set-ups available for the analyses as well as the data of the specific material parameters used for the spectral analyses will be described in the following sections.

3.2.1 X-ray Photoelectron Spectroscopy

X-ray photoelectron spectroscopy (XPS), also referred to *electron spectroscopy for chemical analysis* (ESCA) is a surface sensitive spectroscopic method based on the photoelectric effect. In this technique, a sample is irradiated by a beam of x-rays with a known energy. The x-ray photons can transfer their entire energy to core level electrons in the material. After the absorption of photons with enough energy, the electrons can escape the atom and the material. The emitted photoelectrons are detected and counted depending on their kinetic energy by an electron spectrometer. It is the kinetic energy of the photoelectrons that gives the information about the binding states of the atoms in the material.

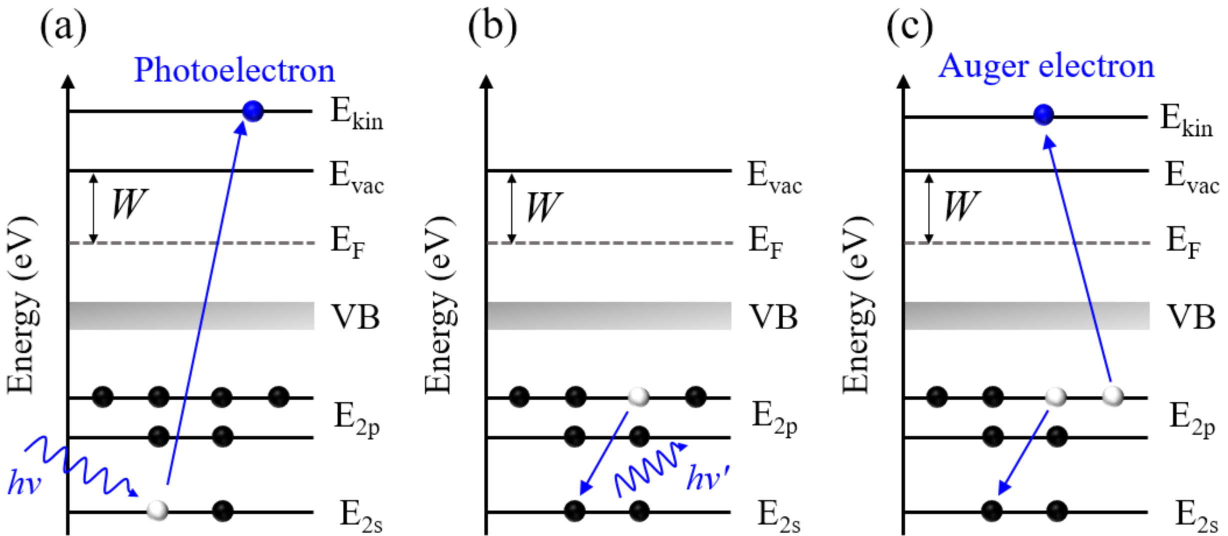

Figure 3.3 Schematic illustration of (a): creation of a photoelectron by an incident x-ray with energy of hv, (b): emission of a photon with energy of *hv'* by the relaxation of an outer electron into the hole, (c): emission of an Auger electron by the secondary x-ray with energy of *hv'*.

The XPS method is based on the photoionization process. Some possible phenomena that occur in this process are illustrated in Figure 3.3.

In Figure 3.3, the black, white and blue spheres represent the electrons, the holes and the excited electrons that escape the material, respectively. The vertical axis represents the energy axis, whereas some characteristic energy levels, e.g. Fermi level, vacuum level are shown as horizontal lines. Figure 3.3-(a) shows the photoionization process, where an electron in a specific core level with a binding energy of BE is excited to a kinetic energy level above the vacuum level by a photon with enough energy of hν. In this process, the kinetic energy of the excited electron (photoelectron) is given by [96]:

$$\mathrm{KE} = h\nu - \mathrm{BE} - W \tag{3.2}$$

Where h is the Planck constant, ν is the frequency of the photon and W is the work function of the material. After the formation of a photoelectron, another core level electron can be relaxed into the hole by releasing a characteristic fluorescence radiation with energy of $h\nu'$, as shown in Figure 3.3-(b). The energy of the fluorescence radiation $h\nu'$ is then enough to ionize another core level electron, which is then called Auger electron, as shown in Figure 3.3-(c). The XPS analysis of any sample in this work is mainly based on the measurement of the photoelectrons and the Auger electrons.

A typical XPS survey spectrum of a $Cu(In,Ga)Se_2$ sample, which is used as substrate material in this work, is given in Figure 3.4. The spectrum consists of mainly the characteristic core level photoelectron peaks (Cu $2p_{1/2}$, Ga $2p_{3/2}$ etc.) and the Auger electron peaks (In MNN, Se LMM etc.). The upwards bending shape of the spectrum from right to left hand side is due to the secondary electrons that form a background. These are electrons, which lose energy in the photoionization process by inelastic collisions, hence they do not carry a specific and therefore a characteristic energy of a core level.

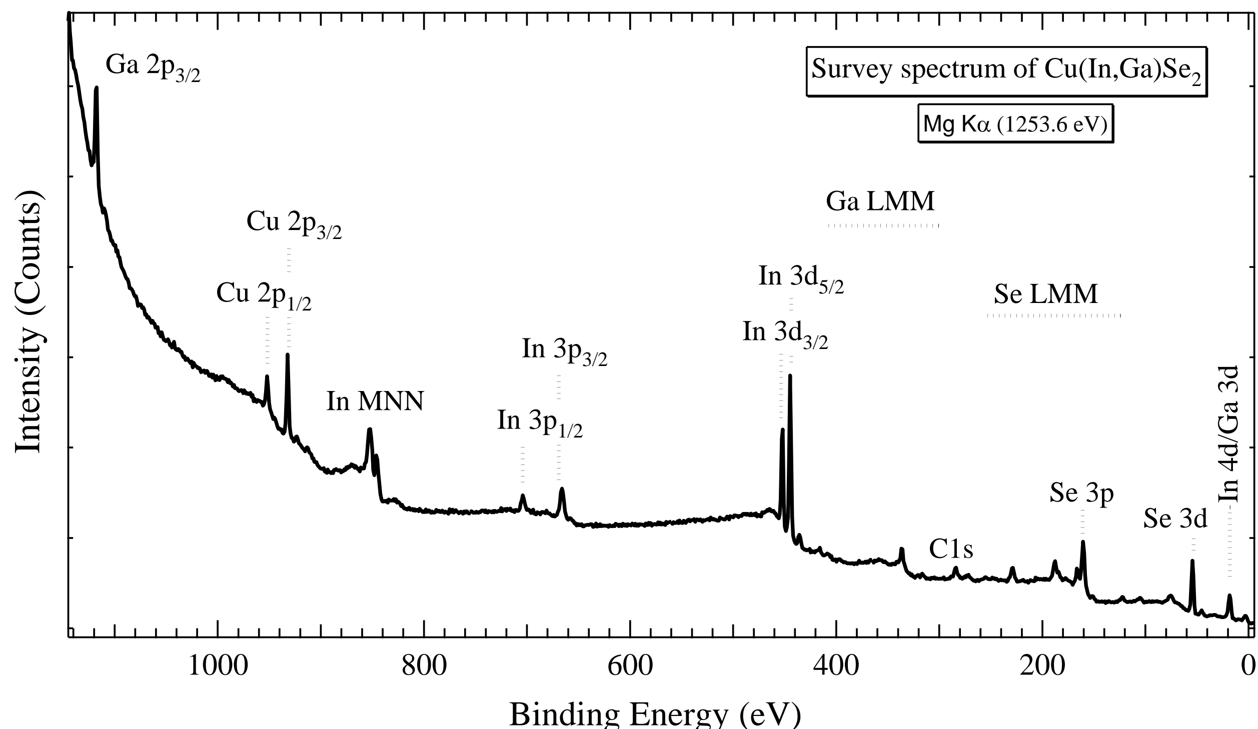

Figure 3.4 A typical XPS survey spectrum of a $Cu(In,Ga)Se_2$ sample measured with Mg Kα x-ray source (hν=1253.6 eV).

The spectrum in Figure 3.4 is recorded using an x-ray source of Mg Kα, which gives rise to an x-ray energy of 1253.6 eV. In addition to Mg Kα, another x-ray source of Al Kα with 1486.6 eV energy is used in this work as excitation energy in the photoionization process. Beside the Mg Kα and Al Kα laboratory sources, tunable synchrotron-based x-rays are used in this work as well, which allow to select a desired excitation energy.

In the measurement of the spectrum in Figure 3.4, photoelectrons are counted by the spectrometer according to their kinetic energies. The count of the electrons is reflected in the vertical axis with intensity in unit of (Counts). By convention, the XPS core level spectra are plotted with binding energy (BE) in the horizontal axis in eV units, as shown in Figure 3.4. It is the BE that gives characteristic information and remains unchanged for a core level with the same chemical environment even under different excitation energies. Since the spectrometer counts the photoelectrons according to their Kinetic Energy (KE), it has to be converted to BE.

As it was shown in Equation 3.2, the KE of a photoelectron is related to its BE with the photon energy (*hv*) and the work function of the material (*W*). Basically, the Equation 3.2 is used for the

conversion of KE to BE, however the W in there might be confusing because it is the work function of the sample, which is defined as the minimum energy required by an electron at the Fermi level to escape the material ($W = E_{vac} - E_F$). In the XPS measurement, the sample is in electrical contact to the spectrometer and therefore they are thermodynamically in equilibrium. Thus, their Fermi levels are energetically aligned, as shown schematically in Figure 3.5.

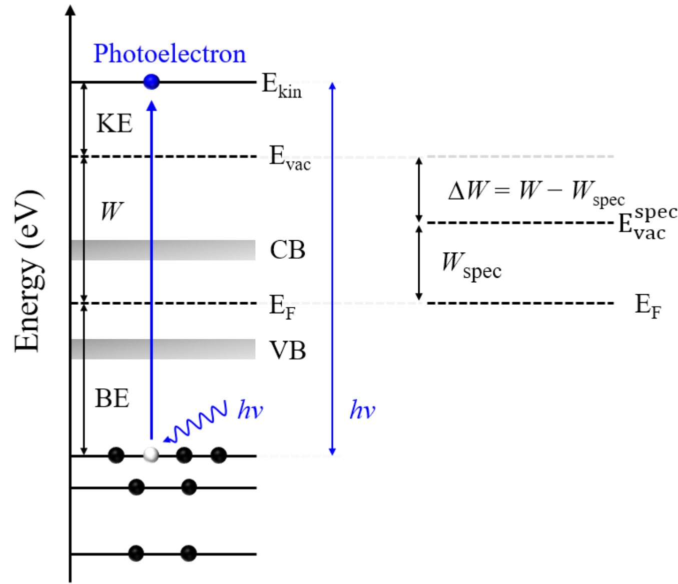

Figure 3.5 Schematic illustration of the energetic situation of a photoelectron and the work function of the spectrometer, where their Fermi levels are aligned due to electrical contact [97].

It can be clearly seen in Figure 3.5 that the "effective" work function that the electron is exposed to, is reduced by ΔW, as a result of the work function of the spectrometer (W_{spec}). Adding the additional term (ΔW) to the equation 3.2 gives:

$$\mathrm{KE} = h\nu - \mathrm{BE} - W_{spec} \quad (3.3)$$

W_{spec} is usually determined by measuring clean Au or Ag metals in the calibration of the spectrometer. After the calibration, it is assumed that the spectrometer remains stable for a long time under ultra-high vacuum. However, the calibration of the XPS spectra in this work is done at each measurement by measuring additionally a clean gold foil on the manipulator, which has a core level binding energy of BE (Au $4f_{7/2}$)=84.0 eV according to reference [75]. Once the measured XPS spectrum is calibrated, its BE gives information about its binding state and the chemical environment, which can be estimated by a comparison of BE with the literature values that are

widely available for instance online in the NIST database [98]. The comparison of BEs should be done carefully though, since some other factors can affect the measured BE, for instance charging of the sample due to its bad conductivity or a bad electrical contact of the sample to the experimental setup.

Another feature that contributes to the XPS spectra is the Auger electron, which arises because of the Auger decay as shown in Figure 3.3-(b) and (c). Since the origin of an Auger electron is the secondary x-ray ($h\nu'$), its kinetic energy is fixed and characteristic, and does not depend on the energy of the incoming x-ray ($h\nu$). Therefore, the Auger spectra are plotted in KE as convention. In general, the Auger electrons are more sensitive to the chemical environment of an atom than photoelectrons [99]. The so-called modified Auger parameter α' provides valuable information regarding the chemical state of an atom in a sample, which is calculated by the addition of the BE of photoelectron and the KE of Auger electron [100]:

$$\alpha' = \text{BE (photoelectron)} + \text{KE (Auger electron)} \tag{3.4}$$

The advantage of α' in the determination of the chemical state is that the α' is a fixed value for a specific compound and is not affected by the surface dipoles and band bending; and systematical errors in determining the work function of the spectrometer do not play a role due to canceling of each other in the addition. Another advantage is that the α' is independent of the excitation energy ($h\nu$), since the BE (photoelectron) and KE (Auger electron) are independent of $h\nu$. Details on the modified Auger parameter concept can be found in [101]. Similar to BE of core level electron, a widely used database of α' can be found in [98,102].

Spectrometer

The count of photoelectrons according to their kinetic energies is schematically illustrated in Figure 3.6. In the x-ray tube, electrons are accelerated onto a magnesium or aluminum anode under a potential energy in the range of 10-15 keV. The accelerated electrons hit the target anode and produce x-ray radiation and Bremsstrahlung. The x-ray radiation contains Mg $K\alpha_{1,2}$ and Al $K\alpha_{1,2}$ lines with a line width of 0.70 eV and 0.85 eV, respectively. The spectral lines have the energy of Mg $K\alpha_1$=1253.6 eV, Mg $K\alpha_2$=1253.4, Al $K\alpha_1$=1486.6 eV and Al $K\alpha_2$=1486.2 eV [103]. The usage of a crystal monochromator enables to select only Mg $K\alpha_1$ or Al $K\alpha_1$. However, for each photoelectron peak that results from the routinely used Mg and Al $K\alpha$ x-ray photons, there is a

family of minor peaks (satellite peaks) at lower binding energies with intensity and spacing characteristic of the x-ray anode material. For instance, the most intense satellite peaks of Mg Kα appear in the XPS spectra for $K\alpha_3$ and $K\alpha_4$ emissions at a displacement of 8.4 eV and 10.1 eV, and with a relative height of 8.0 % and 4.1 %, respectively [77]. Most of the energy of the incident electrons to the anodes is released in form of heat, therefore Mg and Al anodes have to be cooled down with surrounding water flow to prevent any degradation.

Once an electron has been ejected from the sample, its kinetic energy is measured most commonly by a concentric hemispherical analyzer (CHA) [75,76]. The spectrometer is composed of three main components: (1) electron optics, which retard the incident electrons; (2) the analyzer, which has one inner and one outer metal hemisphere, which selects the electrons with respect to their kinetic energies; (3) a detector, which counts the electrons. The width of the entrance slit influences the count rate and the resolution of the measurements. In between the outer and the inner hemispheres, an electric field is applied such that the outer one is more negative and the inner one is more positive with respect to the potential at the center [104].

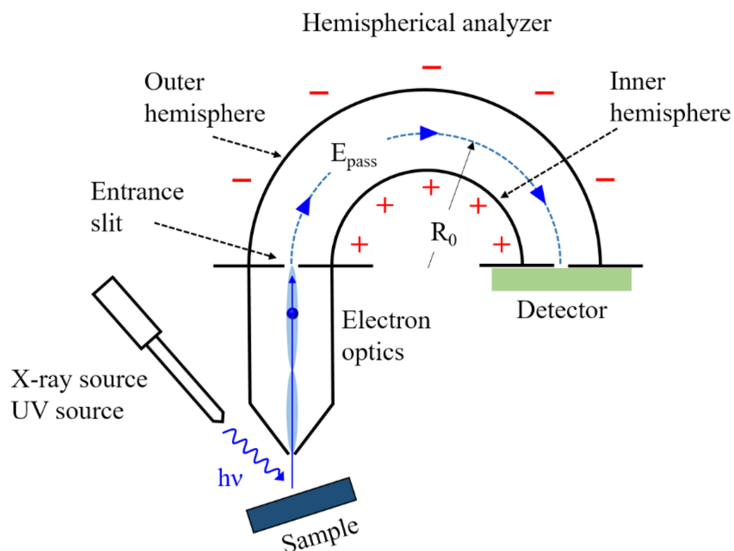

Figure 3.6 Schematic illustration of a photoelectron spectrometer, including its components: hemispherical analyzer, electron optics and detector.

The potential at the center is called pass energy (E_{pass}). The setting of the E_{pass} will allow only electrons with a narrow energy window to pass through the analyzer and reach the detector. The electrons having much higher kinetic energy than the E_{pass} hit the outer hemisphere and those

having much lower kinetic energy are drawn onto the inner hemisphere. These electrons are lost within the analyzer and do not contribute to the measurements. The pass energy (E_{pass}), the width of the entrance slit (s) as well as the radius of the hemispherical analyzer (R_0) are the responsible parameters in the determination of the energy resolution of the analyzer (ΔE), which is expressed with the following equation [75]:

$$\Delta E = \frac{s \cdot E_{pass}}{2 \cdot R_0} \tag{3.5}$$

Information Depth in XPS

X-ray photoelectron spectroscopy is a very surface sensitive technique. Although the x-rays can penetrate about 1000 nm into the sample, the smaller distance of electrons that they can travel through the sample without losing energy, limits the information depth in XPS. The distance that an electron can travel without undergoing inelastic collisions is called inelastic mean free path (IMFP) (λ) of an electron. The λ is a function of the kinetic energy of the photoelectrons and does only slightly depend on the type of the material. The relation of the λ and the KE of an electron shows a similar trend in a large number of materials, expressed by the so-called universal curve of the IMFP, as shown in Figure 3.7 [105].

The λ values within this work are calculated by the TPP-2M formula [106] using the QUASES code [107]. The λ value has a direct influence on the information depth (ID) of the XPS technique. For an electron intensity of I_0, emitted at a depth of d below the surface, the intensity at the surface is attenuated according to the Lambert-Beer law:

$$I_s(d) = I_0 e^{-d/\lambda(KE)} \tag{3.6}$$

where I_s is the attenuated intensity of electrons, I_0 is the initial intensity of electrons, d is the thickness and λ is the IMFP of electrons. The ID is defined as the depth from which 95 % of all photoelectrons are scattered by the time they reach the surface, which gives a value of approximately 3λ. Most of the λ values lie between 1-3.5 nm for Al Kα radiation, which results in an ID of approximately 3-10 nm. The Equation 3.6 can be used to identify the thickness of an overlayer as well, which attenuates the photoelectrons below it.

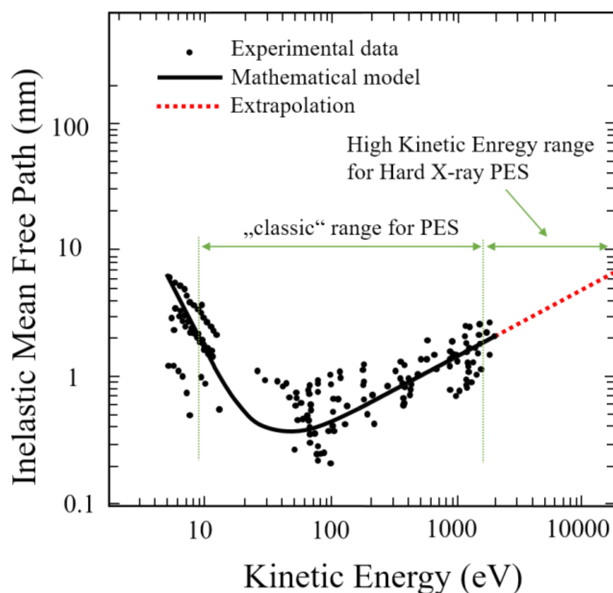

Figure 3.7 Universal curve of the inelastic mean free path (IMFP) (λ) of electrons in a material as a function of photoelectron kinetic energy (adopted from [105]). Data points: Experimental data points for different materials, black line: mathematical model, red dashed line: extrapolation.

Quantitative Analysis of XPS Data

The quantitative analysis of the measured XPS data includes mainly two steps. In the first step; the secondary electron background is subtracted from the XPS peak as shown in Figure 3.8. This is an important step to make the peaks with different binding energies comparable because the background steadily varies from low to high binding energies, as shown in the survey spectrum in Figure 3.4. The choice of the background type is another crucial point. Although different types of backgrounds, such as linear, Tougaard or Shirley background are available, the Shirley background gives usually the best results and is widely used in literature. Therefore, the background subtraction within this work is done by subtraction of a Shirley function [108] from the measured XPS peak, as shown in Figure 3.8.

In the second step, a software-controlled peak fitting routine is applied to the measured data to simulate basically the intensity and the position of the photoemission peak. For this purpose, the computer program "PeakFit" is used in this work [109]. There, photoemission signals are fitted using a Voigt profile, which is a convolution of a Gaussian and a Lorentzian profile, and widely

used at peak fitting in literature. The signal intensity of an individual peak is then calculated as the area of the Voigt profile, as shown in Figure 3.8.

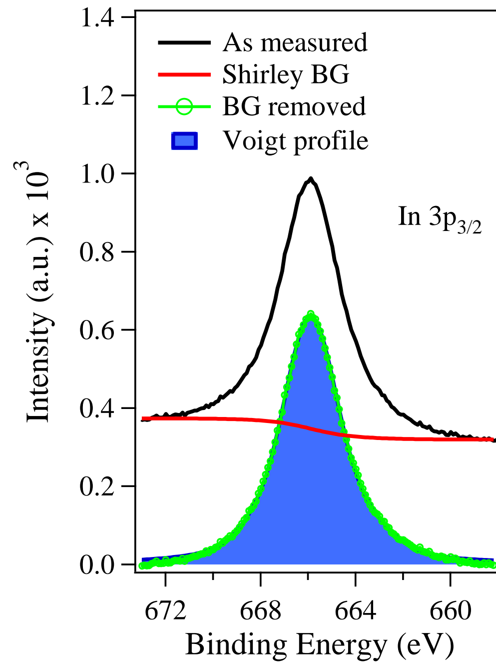

Figure 3.8 Example of quantitative analysis showing the raw data as-measured (black line), the Shirley back ground (red line), removal of the Shirley back ground (green circles) and the peak fitting by a Voigt profile (blue area). The integrated blue area gives the intensity of the corresponding peak.

The intensity of an individual photoemission peak is influenced by many factors; therefore, it has to be normalized to these factors before any comparison between two different peaks. The intensity of a peak is given [110]:

$$I = C \cdot n \cdot I_0 \cdot d\sigma/d\Omega(h\nu) \cdot T(E_{kin}) \cdot \lambda(E_{kin}) \quad (3.7)$$

The explanation of each factor is given in the following:

C is the concentration of the element.

n is the number of scans, which is done during the measurement of the XPS signals.

I_0 is a measure of the incoming beam flux during the measurement. This is especially important to consider in the HAXPES measurements at the synchrotron, since the ring current, thus the incoming x-ray intensity in the synchrotron, steadily declines after each injection of electrons into

the ring. I_0 during the HAXPES measurements in this work is recorded using an N_2 ionization chamber, which is attached between the experimental setup and the x-ray source.

$d\sigma/d\Omega$ is the partial subshell photoionization cross section. It describes the probability that a photon with a certain energy will be absorbed by an electron in a certain shell of a certain atom. The values are tabulated in [111,112] for some energy values. The cross section values in this work for a certain excitation energy (*hv*) are then calculated using the tables in [111,112] and the best fit of the given values. The calculated subshell photoionization cross section values, which are used in Chapter 4 and Chapter 5 are listed in Table 3.2

Table 3.2 Calculated subshell photoionization cross section values for some selected core levels and photon energies for the quantitative analysis in this work. The values are given in unit of kb ($=10^{-21}$ cm^2).

Core level \ hν (eV)	2030	3000	4000	5000	6000
Cu $2p_{3/2}$	17.32	5.51	2.30	1.16	0.66
In $3d_{5/2}$	12.42	4.06	1.74	0.90	0.52
In $3p_{3/2}$	13.73	6.13	3.27	1.98	1.30
Ga $2p_{3/2}$	22.91	7.45	3.14	1.59	0.91
Se $2p_{3/2}$	32.70	11.19	4.80	2.45	1.40
Cd $3d_{5/2}$	11.24	3.67	1.58	0.62	0.47
S 1s	-	14.57	6.84	3.77	2.31

$T(E_{kin})$ is the transmission function of the photoelectron spectrometer, which describes the sensitivity of the spectrometer to the photoelectrons according to their kinetic energies. It can be either provided by the device supplier or determined experimentally. For the experimental determination, different peaks of a clean sample such as Au, Cu etc. are measured. Using the calculated cross section values and Equation 3.7, $T(E_{kin})$ can be calculated in a way that the intensities (I) of different core level peaks give the same value. In this work, a transmission function of

$$T(E_{kin}) = 840.2335 \cdot (E_{kin})^{-0.9748} \tag{3.8}$$

is used for the spectrometer at the CISSY setup (see Section 3.3.1), which is experimentally determined by Tschöke [113]. The $T(E_{kin})$ of the analyzer at the HIKE setup (see Section 3.3.2) for

HAXPES measurements is provided by VG-Scienta-Gammadata and described by the following polynomial [19]:

$$T(E_{kin}) = 1 - 0.041 \cdot x + 9.4 \cdot 10^{-4} \cdot x^2 - 1.0 \cdot 10^{-5} \cdot x^3 + 3.9 \cdot 10^{-8} \cdot x^4 \; ; \; x = \frac{E_{kin}}{E_{pass}} \quad (3.9)$$

$\lambda(E_{kin})$ is the inelastic mean free path (IMFP) of the photoelectrons as described previously. The $\lambda(E_{kin})$ values in this work are calculated by the TPP-2M formula [106] using the QUASES code [107]. The calculated IMFPs for some selected core levels and excitation energies and the corresponding information depths (ID≈3λ) are listed in Table 3.3. The normalization of the XPS signal intensities with λ provides a comparison of the elements within the same sampling depth.

Table 3.3 Calculated inelastic mean free paths of some selected photoelectrons and excitation energies and the corresponding information depths (ID). The *hν* is given in eV, λ and ID in nm, respectively.

hν (eV)	2030		3000		4000		5000		6000	
λ, ID (nm) / Core level	λ	ID	λ	ID	λ	ID	λ	ID	λ	ID
Cu $2p_{3/2}$	21.5	6.4	35.2	10.6	48.5	14.5	61.1	18.3	73.4	22.0
In $3d_{5/2}$	-	-	41.4	12.4	-	-	-	-	-	-
In $3p_{3/2}$	25.4	7.6	38.8	11.7	51.9	15.6	64.4	19.3	76.6	23.0
Ga $2p_{3/2}$	18.6	5.6	32.7	9.8	46.1	13.8	58.8	17.6	71.1	21.3
Se $2p_{3/2}$	13.6	4.1	28.3	8.5	41.9	12.6	54.9	16.5	67.3	20.2
Cd $3d_{5/2}$	29.1	8.7	42.3	12.7	55.2	16.6	67.6	20.3	79.7	23.9
S 1s	-	-	12.6	3.8	27.8	8.3	41.5	12.4	54.4	16.3

In this work, the normalization of a measured XPS signal is done using the previously mentioned normalization factors in order to have a concentration profile within a certain information depth using the following formula:

$$I(\text{normalized}) = \frac{I(\text{measured})}{n \cdot I_0 \cdot d\sigma/d\Omega(h\nu) \cdot T(E_{kin}) \cdot \lambda(E_{kin})} \quad (3.10)$$

3.2.2 Ultraviolet Photoelectron Spectroscopy

Ultraviolet photoelectron spectroscopy (UPS) allows analysis of valence electron states. Excitation energies lower than 100 eV mark the ultraviolet range of photoelectron spectroscopy. The method that uses this energy range of excitation energy is referred to as UPS. In this technique, ultraviolet radiation of a helium discharge lamp is commonly used, resulting in excitation energies of 21.22 eV and 40.82 eV from the He I and the He II emission lines, respectively. The resolution of the He I and He II sources are 3 meV and 17 meV, respectively. The high resolution of especially He I allows high resolution measurements of the valence band edge [114], which is usually limited by the energy resolution of the spectrometer [115].

A typical valence band spectrum of a $Cu(In,Ga)Se_2$ sample is shown in Figure 3.9-(a), which is recorded under He I radiation source.

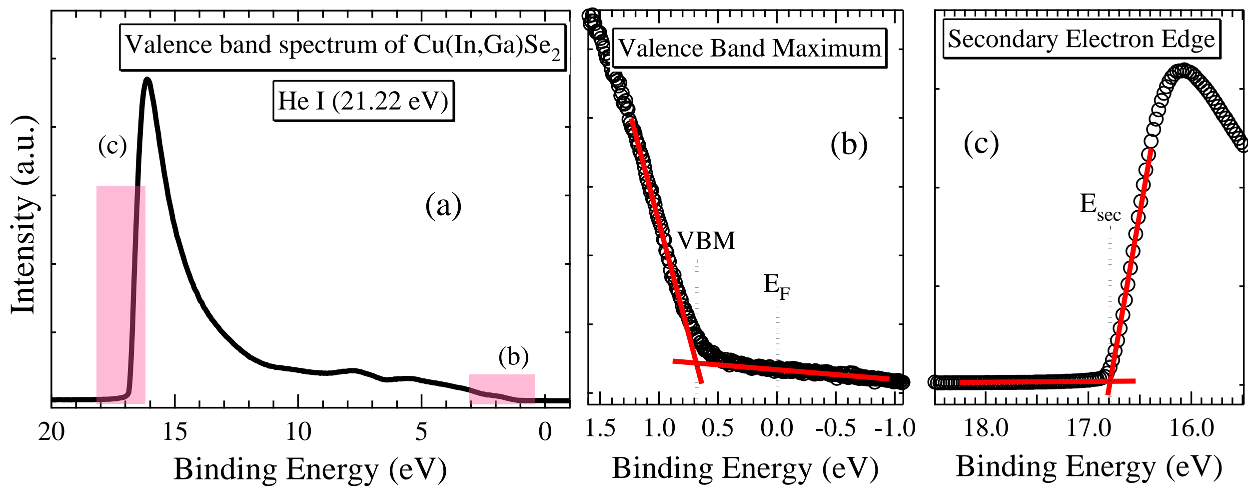

Figure 3.9 (a): Valence band spectrum of a $Cu(In,Ga)Se_2$ sample measured with He I (21.22 eV), (b) and (c): the right and the left hand side of the spectrum corresponding to the valence band and the secondary electron edges, respectively.

The work function of the material can be determined by the secondary electron edge, which is shown as an enlargement of the high binding energy side of the spectrum in Figure 3.9-(c). The work function *W* is then calculated by the following equation:

$$W = h\nu - \mathrm{E_{sec}} - \mathrm{E_F} \tag{3.11}$$

where E_{sec} is the position of the secondary electron cutoff, *hv* the excitation energy (He I=21.22 eV) and E_F the Fermi level. The Fermi level is determined by measuring a clean gold sample, which is in electrical contact to both the sample and the manipulator. In UPS measurements, usually a potential in the range of V_{bias}=10-15 V is applied to the sample to speed up the low kinetic energy electrons for them to reach the spectrometer and contribute especially to the secondary electron cutoff. Therefore, the applied bias voltage should be considered in the conversion of the measured kinetic energy of photoelectrons to the corresponding binding energy by simply adding it up to the excitation energy.

The valence band maximum (VBM) can be determined using the band edge of the spectrum at the low binding energy side. It is commonly determined by a linear extrapolation of the valence band onset with respect to the background level (see Figure 3.9-(b)). In most cases, the VBM is determined with an error of about ±0.05 eV that strongly depends on the shape of the corresponding edge.

3.3 Experimental Setups for XPS-UPS and HAXPES Measurements

3.3.1 CISSY Setup for XPS and UPS

The XPS and UPS measurements in this work using laboratory radiation sources are performed at the CISSY (derived from CIS+Synchrotron) setup. It is schematically shown in Figure 3.10. It consists of two x-ray sources of Mg Kα (1253.6 eV) and Al Kα (1486.6 eV), and two UV-light sources of He I (21.22 eV) and He II (40.82 eV). The main vacuum chamber consists of analysis chamber, preparation chamber and load-lock chamber; which are operated under a pressure of about $5 \cdot 10^{-9}$ mbar. The operation under the UHV conditions allows to minimize the contamination of the sample surface.

The photoelectron detection in the CISSY is done with a hemispherical CLAM 4 electron analyzer provided by Thermo VG Scientific. The sputter chamber, which is directly attached to the preparation chamber allows to prepare some TCO layers (i.e. ZnO, CuO) by magnetron sputtering and their in-system characterization with XPS-UPS without breaking UHV conditions. Recently, two additional chambers were attached to the analysis chamber: the PVD chamber, in which some alkali metals (Na, K) and their fluoride compounds (NaF, KF) can be deposited on a CIGSe sample;

the SPV chamber, which provides surface photo voltage measurements under UHV and the opportunity to combine SPV and XPS-UPS measurements of the same sample without air exposure.

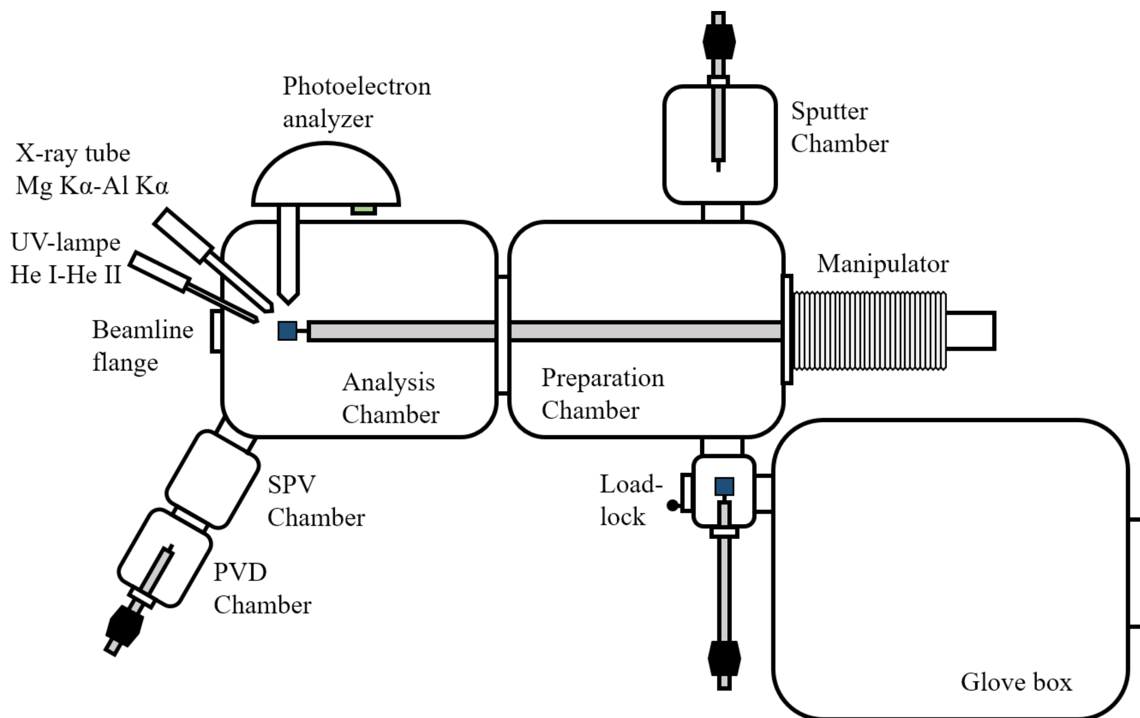

Figure 3.10 Illustration of ultra-high vacuum system CISSY setup.

The sample transfer to the CISSY is done via the load-lock chamber, where eight samples can be stored under UHV. Additionally, the glove box allows the transfer of samples to the analysis chamber without air contact after a dedicated surface treatment under N_2 atmosphere. An additional feature of the CISSY is that it can be moved to the synchrotron and attached to a beamline through the beamline flange as illustrated in Figure 3.10.

3.3.2 HIKE Setup for HAXPES

The hard x-ray photoelectron spectroscopy (HAXPES) measurements in this work are performed at the HIKE (derived from High Kinetic Energy photoelectron spectrometer) endstation, which is operated at the KMC-1 (Kristal Monochromator) located at the BESSY II synchrotron facility. The HIKE endstation has been available for user operation starting from 2006 [116]. It can provide variable photon energies between 2010 and 12000 eV [117]. The monochromatic synchrotron

radiation is directed to the endstation through a slit and a N_2 filled ionization chamber. The incoming light intensity I_0 is measured by the ionization chamber, which is proportional to the ionization current [117].

The experimental chamber is operated under UHV conditions with a basic pressure of about $9 \cdot 10^{-9}$ mbar. The size of the samples has to be maximum 10 mm x 10 mm in order to mount them on the Omicron type sample holder. The sample transfer is done through a load-lock system, which contains a sample magazine that accommodate up to six samples. The analysis system at the HIKE endstation consists of a hemispherical photoelectron spectrometer R4000 manufactured by Scienta Gammadata, which is optimized for high kinetic energy applications. It is a high-resolution electron energy hemispherical analyzer with a 200 mm radius (R_0). It consists of an electron spectrometer supporting high voltage power supply cabinet and a personal computer for instrument control, read-out and data management. The spectra that are measured within this work, are recorded at a constant pass energy of 200 eV. The x-ray beam is horizontally polarized hitting the sample in grazing incidence geometry under an angle of 3° towards the surface. The generated photoelectrons are detected in the polarization plane perpendicular to the beam. The beam flux was kept constant for all measurements (top-up mode of the storage ring). The spot size of the beam on the sample is in the range of 2 mm in length and several µm in height, which reduces the influence of the surface roughness and inhomogeneity on the accuracy of the measurements. The entrance slit of the electron analyzer is fixed to 0.5 mm.

4 Cd Diffusion into Cu-rich and Cu-poor $Cu(In,Ga)Se_2$ Absorbers

It is widely accepted that the best efficiencies in $Cu(In,Ga)Se_2$ (CIGSe)-based thin film solar cells can be achieved by growing the CIGSe absorber under Cu-poor conditions [15,39,118–121]. It has been recently reported that the insertion of a Cu-poor compound $Cu(In,Ga)_3Se_5$ at the CIGSe/CdS interface leads to an improvement in the photovoltaic performance [122]. The improvement in the performance was attributed to a higher Cd diffusion from CdS side into the Cu-poor compound, which in turn causes a type inversion on the CIGSe surface from p- to n-type conductivity because of the Cd (donor) doping into the $Cu(In,Ga)_3Se_5$ compound [122]. Despite the improvement of the conversion efficiencies in the CIGSe-based solar cells due to the Cd diffusion into the CIGSe, there is still a lack of information on the underlying diffusion mechanisms of the Cd into the CIGSe. Therefore, a better understanding of the diffusion of the constituent atoms around the CIGSe/CdS interface is required for further improvements.

The aim of this chapter is to investigate the mechanism of Cd diffusion into the CIGSe compounds depending on their Cu concentration. In the first section of this chapter, density functional theory considerations on the Cd diffusion into the CIGSe absorbers with respect to their Cu composition are summarized, where the qualitative as well as quantitative differences in the diffusion mechanisms are shown in case of “Cu-poor” and “Cu-rich” absorbers. In the following sections, the experimental proof of the theoretical considerations is done using photoelectron spectroscopy techniques.

4.1 Mechanism of the Cd Diffusion into Cu-rich and Cu-poor CIGSe Absorbers: Theoretical Considerations

The objective of this section is to present ab-initio density functional theory (DFT) calculations on the Cd diffusion into the $Cu(In,Ga)Se_2$ compounds with respect to their Cu concentration. The DFT calculations were carried out by the ComCIGS-II project partners J. Kiss and H. Mirhosseini from the Max-Planck-Institute for Chemical Physics of Solids [11]. The experimental proof of the DFT calculations is the main motivation of this chapter and will be shown later in the second section using photoelectron spectroscopy methods.

Kiss et al. [9–11] carried out ab-initio density functional theory (DFT) calculations to study the correlation between the diffusion properties of Cd dopants with the copper concentration of the $Cu(In,Ga)Se_2$ absorber material. Details on the theoretical methodology can be found in [9,10]. As model systems in the theoretical calculations for "Cu-rich" compounds they investigated $CuInSe_2$ and to represent the "Cu-poor" absorber material they investigated the $CuIn_5Se_8$ ordered vacancy compound (OVC).

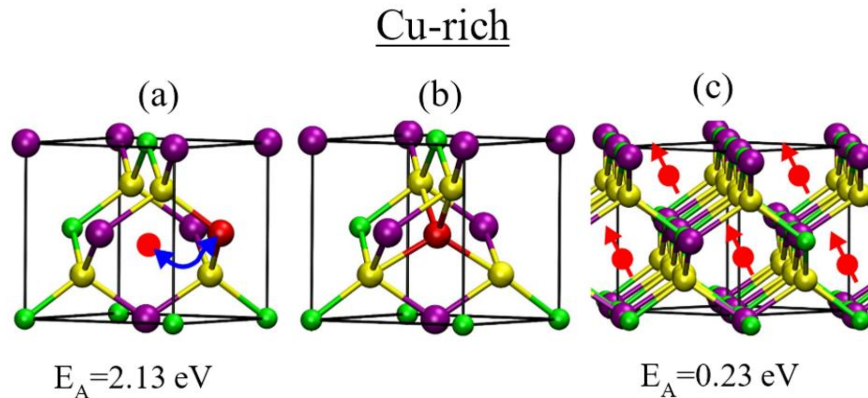

Figure 4.1 Diffusion mechanism of Cd impurities in "Cu-rich" $CuInSe_2$ absorber material. The Cd impurity is shown in red, the Cu, In and Se atoms are presented by green, purple and yellow spheres, respectively. (a) shows the Cd_{Cu} substitutional defect, from where Cd first moves (blue arrow) to a Cd_i interstitial position shown in (b). The Cd_i can diffuse along the hexagonal channels in $CuInSe_2$, indicated by red arrows shown in (c) [11].

a) Cd diffusion in the "Cu-rich" $CuInSe_2$ compound: They studied first the diffusion mechanism and the underlying activation barriers of Cd impurities in "Cu-rich" $CuInSe_2$ using the nudge elastic

band (NEB) method [123]. In this material, they investigated the formation energies of different Cd substitutional and interstitial defects. They found that the most stable energy configuration for Cd impurities is to occupy Cu positions in the +1 charge state (Cd_{Cu}^+). The formation energy of such a defect is −1.21 eV, where the negative formation energy suggests that a low concentration of Cd_{Cu}^+ defects can be formed spontaneously. Considering that the CIGSe absorber materials have preferentially a Cu-depleted surface in the monolayer scale [119], this means that even in the Cu-rich material there is a relatively high number of V_{Cu} defects present. Hence, one can expect that during the deposition of the CdS buffer layer such V_{Cu} vacancies will be first occupied by Cd impurities, forming highly stable Cd_{Cu}^+ defects [27]. Therefore, to simulate the material transport of Cd in the "Cu-rich" material, they carried out NEB calculations [123] in large supercells of $CuInSe_2$ consisting of 224 atoms, where a Cu atom was substituted by a Cd impurity.

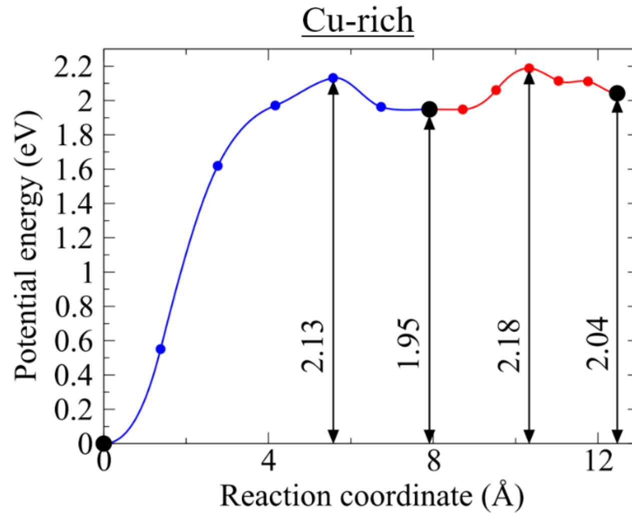

Figure 4.2 Activation energies for the diffusion of Cd in "Cu-rich" $CuInSe_2$ material. The reaction coordinate is the distance between the Cartesian coordinates of the Cd atom and its original starting position along the diffusion path. The first part of the path shown with blue corresponds to moving Cd from a substitutional to an interstitial position, and the second part schematized with red color shows the diffusion of Cd along the hexagonal channels [11].

The atomic structure for the Cd_{Cu}^+ defect is shown in Figure 4.1-(a). They investigated different diffusion paths, and they found that the most favorable is to transfer the Cd atom from the Cd_{Cu}^+ defect into a Cd_i interstitial defect. This migration path from the Cd_{Cu}^+ to Cd_i is schematized by the blue arrow in Figure 4.1-(a). The activation energy calculated for this part of the path is 2.13 (see the path shown in blue in Figure 4.2). The atomic structure of the Cd_i defect is presented in Figure

4.1-(b). Once Cd occupies the Cd_i position, it can diffuse rather easily along the hexagonal channels formed by three anions and three cations of the $CuInSe_2$ structure, which are running along the [110] direction in that crystal. The potential energy surface for the diffusion path along these hexagonal channels is rather flat (see the red path shown in Figure 4.2), and the reaction barrier is 2.18−1.95=0.23 eV.

b) Cd diffusion in the "Cu-poor" $CuIn_5Se_8$ compound: To assess the activation energies for the diffusion of Cd in the "Cu-poor" material, Kiss et al. [9–11] performed NEB calculations in the $CuIn_5Se_8$ phase. In comparison to the stoichiometric $CuInSe_2$, in the OVC phase there are ordered arrays of pristine V'_{Cu} defects present in that material [9] (see Figure 4.3-(a)).

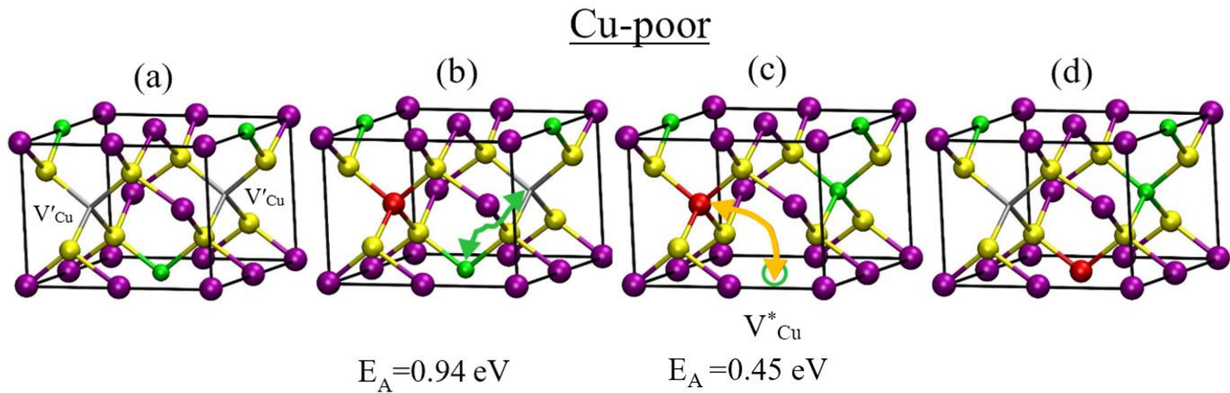

Figure 4.3 Diffusion mechanism of Cd impurities in "Cu-poor" $CuIn_5Se_8$ absorber material. The Cd impurity is shown in red, the Cu, In and Se atoms are presented by green, purple and yellow spheres, respectively. (a) shows the $CuIn_5Se_8$ OVC compound. (b) presents the Cd impurity sitting in a pristine V'_{Cu} site, which are shown by gray color. For the diffusion of Cd, first a Cu atom is displaced into a nearby V'_{Cu} position (indicated by the green arrow) leaving behind a V^*_{Cu} vacancy. Next, the Cd impurity occupies this V^*_{Cu} vacancy (c), which is indicated by an orange colored arrow. (d) presents the situation, where Cd sits in this V^*_{Cu} site [11].

In a doped system containing Cd impurities these empty sites can be occupied either by Cd or by Cu. A more detailed discussion regarding the structure of the OVC compounds and on the energetics of the Cd insertion is presented in [9]. Considering that V'_{Cu} defects are building blocks of the OVC phases, and there are two of these defects present in every formula unit, one can expect that Cd impurities originating from the CdS buffer layer will first populate these sites. Therefore, in the current work calculations have been carried out on a system, where one of these pristine V'_{Cu} sites are occupied by a Cd impurity (see Figure 4.3-(b)). The −2.08eV insertion energy of Cd at

this site calculated with the HSE functional [124] indicates that occupying V'_{Cu} sites by Cd is energetically highly favorable.

In the $CuIn_5Se_8$ OVC compound the diffusion mechanism of Cd was investigated in [10], and it was found that the diffusion of Cd is a two-step process. First, a Cu atom is displaced into one of the V'_{Cu} sites (see the green arrow in Figure 4.3-(b)), leaving behind a V^*_{Cu} vacancy (see Figure 4.3-(c)). The activation energy computed for this part of the diffusion path is 0.94 eV (see the part of the reaction path shown with green color in Figure 4.4). Compared to the ordered structures, the system with the V^*_{Cu} vacancy is 0.27 eV higher in energy in $CuIn_5Se_8$.

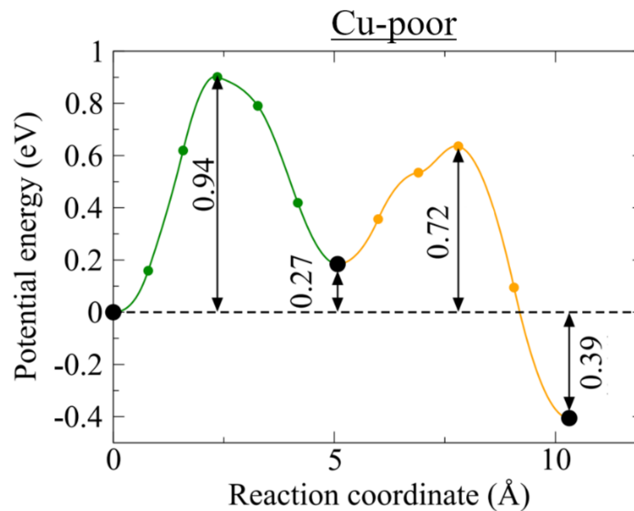

Figure 4.4 Activation energies calculated with the NEB method for the diffusion of Cd in the "Cu-poor" $CuIn_5Se_8$ material. The reaction coordinate is the distance between the Cartesian coordinates of the Cd atom and its original starting position along the diffusion path. Along the double-hump profile, the first part of the path shown with green corresponds to the displacement of a Cu atom to a V'_{Cu} site, leaving behind a V^*_{Cu} vacancy. The part in orange color depicts the diffusion path of Cd into this newly created V^*_{Cu} site [11].

In the second step, the Cd impurity will leave the V'_{Cu} site, and it moves into the V^*_{Cu} defect left behind by Cu (see the orange arrow in Figure 4.3-(c)). By repeating these two reaction steps, Cd diffuses along the "Cu-poor" OVC material. For the second reaction step, they calculated an activation energy of 0.45 eV (see the part of the diffusion path shown in orange color in Figure 4.4). The resulting defect complex, where Cd occupies a Cu substitutional site, and the Cu which

was originally sitting there now is located in a pristine V'_{Cu} site, is 0.39 eV lower in energy compared to the ordered $CuIn_5Se_8$ compound.

c) Comparison of Cd diffusion in "Cu-rich" and "Cu-poor" compounds: Kiss et al. [11] conducted the same theoretical calculations on the Cd diffusion into the counterpart materials containing Ga (i.e. $CuGaSe_2$ and $CuGa_5Se_8$). By comparing the reaction barriers along the Cd diffusion paths between the different materials, they concluded that the activation energies are rather similar between $CuInSe_2$ and $CuGaSe_2$. The same applies between $CuIn_5Se_8$ and $CuGa_5Se_8$. Nevertheless, there is a clear qualitative difference between the diffusion mechanism in the "Cu-rich" compared to the "Cu-poor" compounds. Namely, in the "Cu-rich" $CuInSe_2$ and $CuGaSe_2$ the Cu atoms are not directly involved in the diffusion, but they indirectly play a role as V_{Cu} defects, where Cd impurities are being incorporated. In contrast to the "Cu-rich" compounds, in the case of the "Cu-poor" $CuIn_5Se_8$ and $CuGa_5Se_8$ phases Cu atoms are being actively exchanged by Cd impurities during the diffusion process. In addition to the qualitative difference, the two diffusion mechanisms are also quantitatively well distinguishable from the perspective of the activation energies. This is because, in the "Cu-rich" compounds the rate limiting step of the diffusion is the transfer of Cd from the Cd_{Cu} substitutional sites to the Cd_i interstitial positions, with an activation energy in the order of 2.1 eV. For comparison, in the case of the "Cu-poor" materials the kinetics of the diffusion is controlled by the displacement of Cu atoms into the pristine V'_{Cu} positions. This process has an activation energy in order of 0.9 eV, which is half of that of the former process with activation energy of 2.1 eV. Hence, based on the calculated energy profiles, the theoretical calculations suggest that the diffusion of Cd can take place considerably easier in the "Cu-poor" phases compared to the "Cu-rich" materials.

In the following section, evidences of the above-presented DFT calculations on the Cd diffusion are shown using hard x-ray photoelectron spectroscopy.

4.2 Composition-Dependent Cd Diffusion into CIGSe Absorbers

In the standard production of a $Cu(In,Ga)Se_2$ (CIGSe)-based thin film solar cell, a CdS buffer layer is deposited by chemical bath deposition at around 60 °C [28,61] on top of the CIGSe absorber, which is usually grown by a three-stage coevaporation process at 550 °C [12,125]. In some cases, annealing of the CdS-containing cells at 200 °C was observed to improve the device efficiency

[126]. However, Kijima et al. [127] showed in an annealing experiment in vacuum that CIGSe solar cell devices with chemical bath deposited CdS buffer layers were stable only below 320 °C.

Despite the high efficiency of CIGSe-based solar cells, there is still a lack of information on the local chemical changes across the CIGSe/CdS interface, where the photo-generated charge carriers are separated. Using different spectroscopic techniques, many groups suggested that the CIGSe/CdS interface is highly intermixed [27,60,128,129]. It was shown that the CIGSe/CdS interface is Cu-depleted [118,130], which represents the Cu-poor phase of the absorber. The Cu-poor phase at the CIGSe surface is generally accepted to be ordered vacancy compound (OVC) of the CIGSe [15,120,121,131]. It was proposed that the best efficiencies can be achieved by growing the CIGSe absorber layer under Cu-poor conditions [39,118]. The structure and the depth of the strongly Cu-poor region in CIGSe solar cells is still under debate.

It was shown that the Cd atoms can be present in the Cu-poor phase even at low temperatures [9,27]. Additionally, deposition of CdS at elevated temperatures may induce an additional Cd diffusion into the Cu-poor absorber [129]. Similarly, the diffusion of Cd into the absorber is to be expected, when the CIGSe/CdS layers are annealed at elevated temperatures [62]. It was reported that the diffusion of Cd atoms into the CIGSe layer may result in an n type region, which can form a buried p-n junction in the CIGSe absorber layer [132]. It was observed that the excess diffusion of Cd further into the CIGSe absorber may degrade the device performance [127]. Since the underlying diffusion mechanisms of Cd in CIGSe are still unclear, a better understanding of the diffusion of the constituent atoms around the absorber/buffer interface is required for further optimization of the device properties. However, there is a limited data available in literature dealing with the diffusion mechanism of the dopants [133–137].

In the previous section, it was theoretically shown that the diffusion mechanisms of Cd into the CIGSe compounds differ fundamentally from each other depending on their Cu concentration. In order to investigate this phenomenon, the Cu-rich CIGSe+CdS and the Cu-poor CIGSe+CdS samples (i.e. sample #1 and sample #2 in Table 3.1, respectively) are investigated in this section using hard x-ray photoelectron spectroscopy. Details on the sample preparation process can be found in Section 3.1.3**.**

The diffusion of Cd into the CIGSe can take place through the grain (bulk diffusion) or along the grain boundaries (grain boundary diffusion). However, it was reported that the grain boundary

diffusion of Cd in CIGSe is negligibly small compared to the bulk diffusion of it [28,138]. For that reason and due to the limitations of the photoelectron spectroscopy method, grain boundary diffusion of Cd is not considered in the interpretation of the experimental data in the following.

In Figure 4.5, survey spectra of CdS covered CIGSe samples recorded at room temperature are shown in the binding energy range up to 2500 eV for an excitation energy of 3000 eV. The thickness of the CdS film is in the range of less than 10 nm.

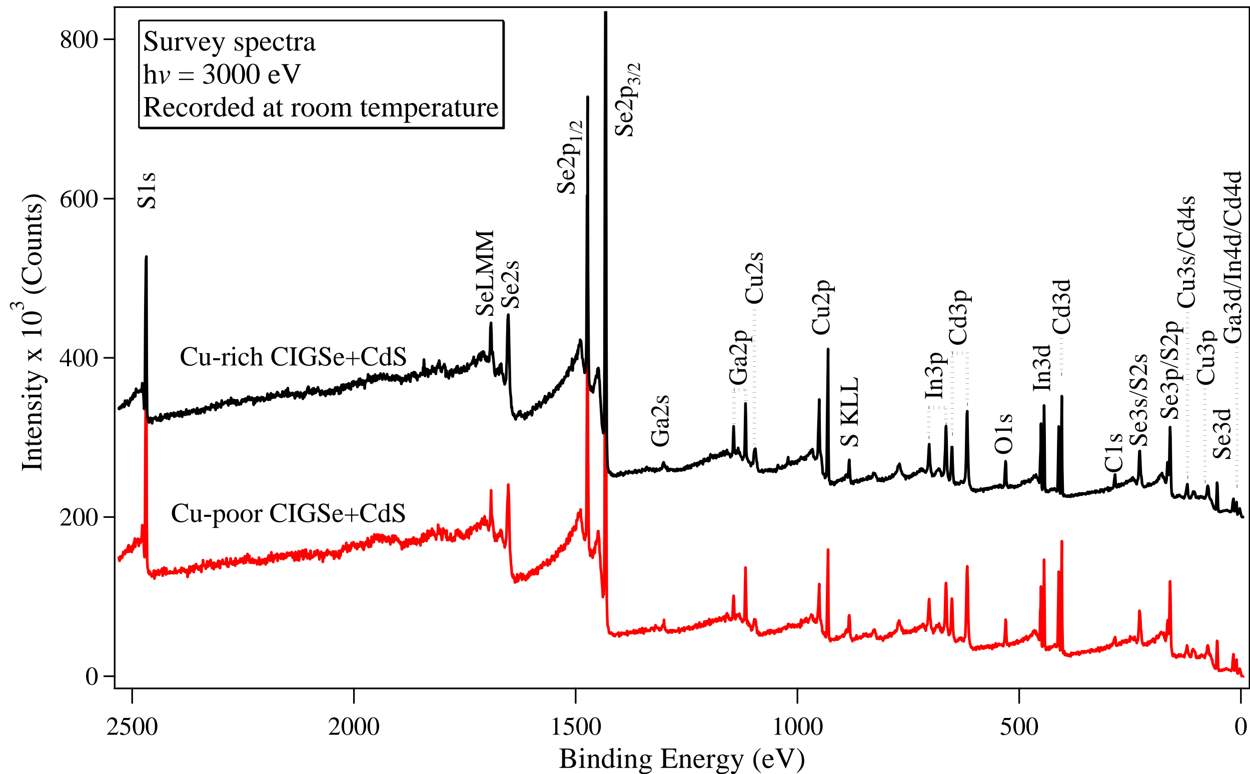

Figure 4.5 XP survey spectra of chemical bath deposited Cu-rich (black) and Cu-poor (red) CIGSe/CdS samples at 3000 eV excitation energy (corresponds to an information depth of between 4 nm and 12 nm depending on the core level signal), measured at room temperature.

Using the excitation energy of 3000 eV in Figure 4.5, results in an information depth of between 4 nm and 12 nm depending on the type of the core level signal (see Table 3.3). Two types of absorbers were investigated, namely Cu-poor and Cu-rich ones as already mentioned. Since the thickness of the CdS film is limited to a few nanometers only, photoemission signals originating from the CIGSe absorbers are present in both spectra due to the increased kinetic energy of the considered electrons that goes along with an increased information depth. In addition, cadmium and sulphur related peaks appear in the spectra as expected. Moreover, small quantities of carbon and oxygen are

detectable on the wet-chemically treated CIGSe/CdS samples due to the usage of aqueous solutions for the deposition of CdS - an indication that carbon and oxygen are incorporated into the CdS film during the growth. This aspect is not considered in the following, thus neglected.

Figure 4.6 shows top view images of bare Cu-poor (a) and Cu-rich (b) CIGSe samples as well as their CdS coated pendants (a1 and b1) obtained with SEM. These samples are similar to ones which are treated in this chapter but they were used for another annealing experiment [62]. However, they reflect similar surface properties, since they have surface concentrations of [Cu]/([In]+[Ga]) = 0.79 (Cu-poor) and 1.03 (Cu-rich) which are close to the ones of the samples that are used in this chapter.

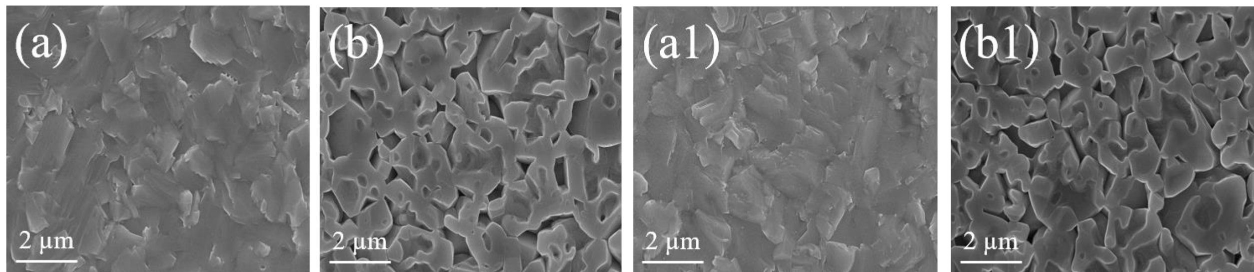

Figure 4.6 SEM top view images of (a): Cu-poor CIGSe, (b): Cu-rich CIGSe, (a1): Cu-poor CIGSe/CdS and (b1): Cu-rich CIGSe/CdS films. The images were taken after the last annealing step in UHV at 400 °C (after Ümsür et al. [62]).

As it can be clearly seen, the CIGSe samples are polycrystalline. In contrast to the Cu-poor sample, the Cu-rich sample shows an increased roughness attributed to the KCN-based etching process that is known to remove superficial Cu_xSe phases. The morphology of the Cu-rich sample is dominated by cavities surrounded by linked structures, which seem to be equally truncated on the same height. On closer inspection, the grains appear very large with dimensions of up to several µm and with grain boundaries forming deep valleys. The Cu-poor sample is less affected by the KCN etching process leaving facets, which are smoother but somehow stronger declined with respect to the surface on the microscopic scale. The truncation of the topmost layer as observed on the Cu-rich sample is not visible on the Cu-poor one. In both cases, step-like structures with several nm dilatations are observed, pointing to a [112] orientated faceting of Cu-poor areas on the grain [131]. With energy dispersive X-ray spectroscopy (EDX) attached to the SEM system, no Cd could be detected on the CdS coated CIGSe samples, indicating that the amount of Cd is below the detection threshold of the EDX system.

For a more detailed analysis of the XP spectra, the Cu $2p_{3/2}$, In $3d_{5/2}$, Ga $2p_{3/2}$, Se $2p_{3/2}$, Cd $3d_{5/2}$ and S 1s core level peaks were measured with higher resolution. In Figure 4.7, the according spectra are shown for room temperature (RT) and for various annealing steps ranging from 180 to 400 °C, all taken at 3000 eV excitation energy. Initially, XPS measurements were done at room temperature (RT). Then, the samples were heated up to 180 °C within approximately 10 min and kept at this temperature level while XP spectra were recorded. After the first annealing step, the temperature was ramped to the next level with about 5 °C/min where subsequent XPS measurements were performed in the same manner as before. All spectra were corrected with respect to their binding energy using the position of the Au $4f_{7/2}$ peak at 84.0 eV [75]. For an improved representation, all peaks were normalized to the background with some offsets added to separate the individual spectra. In Figure 4.7-(a), various Cu $2p_{3/2}$ spectra of the two samples (labelled in red and black) are presented together in one graph. Compared to the Cu-poor CIGSe/CdS sample, the black curves of the Cu-rich CIGSe/CdS sample exhibit an increased signal intensity for all annealing temperatures. In first view, the other constituents of the absorber own similar features in terms of the signal intensity and the energetic position in the course of the annealing process. For temperatures up to 260 °C, the dependency of the Cd $3d_{5/2}$ peak on the annealing process is similar for both, the Cu-poor (red lines) and Cu-rich (black lines) samples.

However, for temperatures above 260 °C the Cd $3d_{5/2}$ peaks of the Cu-poor sample decrease more rapidly and vanish completely at around 360 °C. For the Cu-rich sample, the Cd $3d_{5/2}$ peaks are only damped with ongoing annealing and they are still present even at 400 °C. In contrast to the Cd $3d_{5/2}$ signal, the S 1s peak intensities are less affected in both cases. There is still sulfur on the surface in a reasonable amount. However, compared to the other peaks, the energetic position of the S 1s peaks seems to be highly affected by the annealing process. This implies a variation of the chemical environment of the sulfur atoms. Together with other findings, this point is discussed in the Section 4.3 with a detailed analysis of the core level spectra given elsewhere in this work.

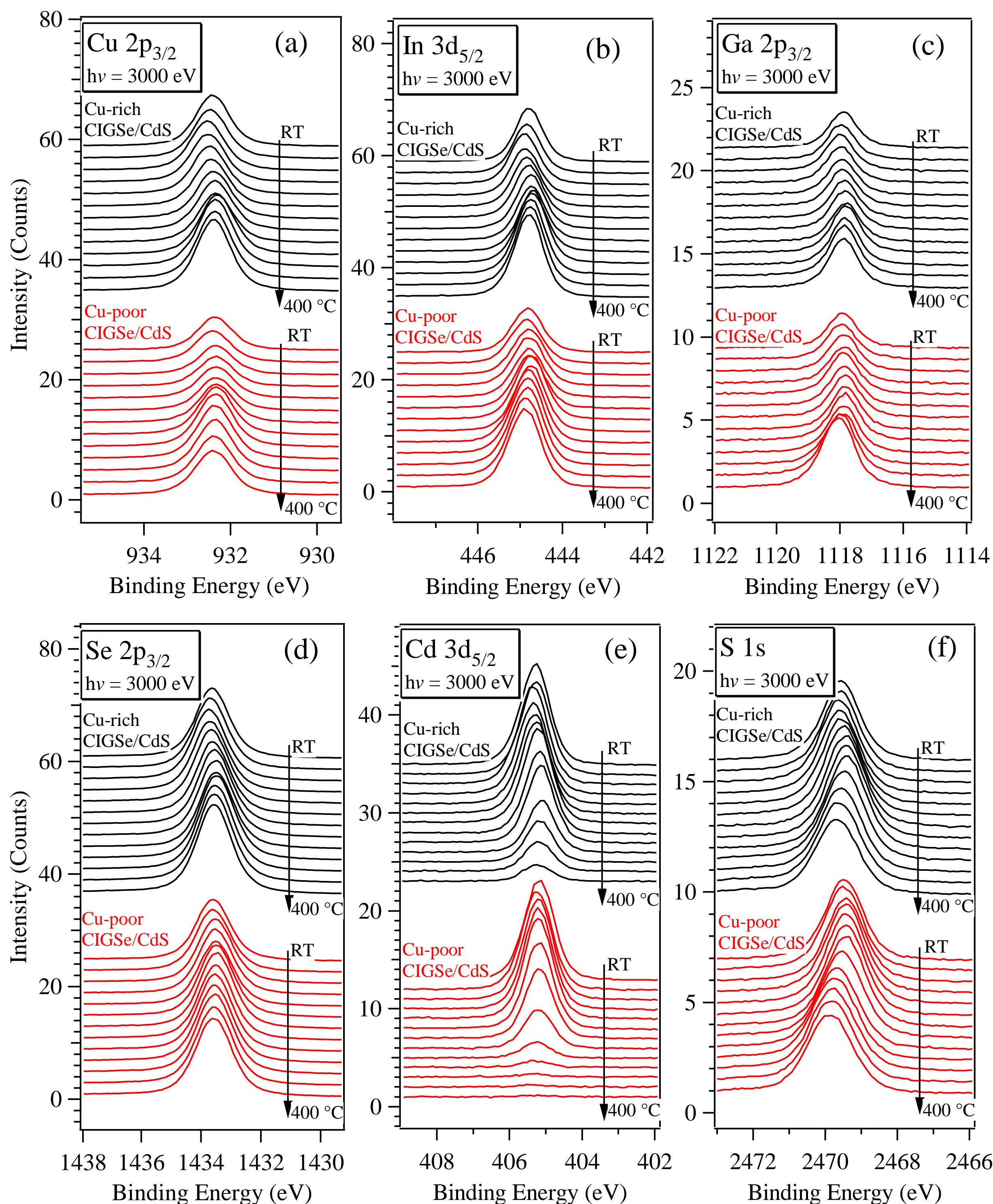

Figure 4.7 XP spectra of the (a) Cu $2p_{3/2}$, (b) In $3d_{5/2}$, (c) Ga $2p_{3/2}$, (d) Se $2p_{3/2}$, (e) Cd $3d_{5/2}$, and (f) S 1s photoemission signals of the CdS/CIGSe samples recorded at the HIKE end-station at BESSY II using 3000 eV excitation energy (see Table 3.3 for the information depths of this specific excitation energy). The measurements were performed at room temperature (RT) and after a series of in-situ annealing steps up to 400 °C in UHV.

Various spectra of the near valence band region for different annealing temperatures are presented in Figure 4.8-(a). The spectra are aligned according to the gold reference and they are normalized to the In $4d_{5/2}$ peak intensity for a better comparability.

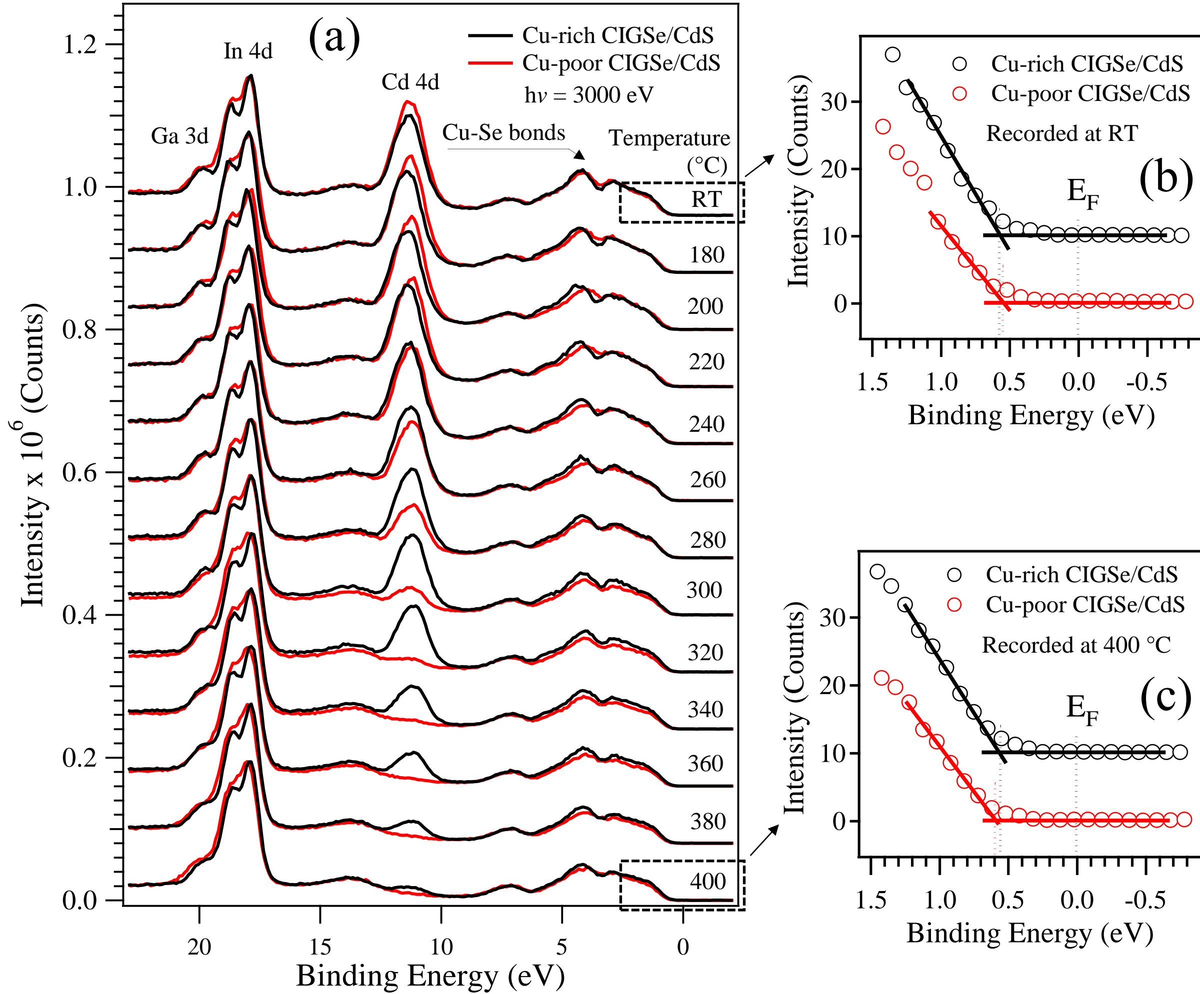

Figure 4.8 (a): XP spectra of In 4d, Ga 3d, Cd 4d, and valence bands for CIGSe in the course of the in-situ heating experiment. All spectra are recorded at hν = 3000 eV and they are normalized to the In $4d_{5/2}$ peak for better comparability. (b)-(c): Magnification of the valence band onsets with linear extrapolations, as two examples to show how the E_{VBM}-E_F values are determined, which are visualized in Figure 4.14 (g). The spectra in (b) and (c) are first normalized to zero and then some offset is added between two spectra for better visibility.

At a first glance, the shape and the position of the In 4d/Ga 3d peak as well as the structure of the valence band up to 8 eV (composed of mainly Cu-Se bonds) look similar in Figure 4.8-(a). Assuming the same In concentration in both samples, the Cd 4d peak of the Cu-poor sample appears

to be slightly higher in the near surface region than the one of the Cu-rich sample. This difference might be interpreted in terms of a more pronounced Cd diffusion into the Cu-poor CIGSe absorber, which already takes place at an early stage of the chemical bath deposition process of CdS at about 35 °C. Liao et al [129] reported that the Cd diffusion into $CuInSe_2$ during the CBD process is negligible. However, Nakada et al [27] found a direct evidence of Cd diffusion into $Cu(In,Ga)Se_2$ thin films during the CBD process of CdS films, being more pronounced in the Cu-poor phase of the substrate; which supports the above interpretation. In the course of the ongoing annealing process, the intensity difference in the Cd 4d diminishes at about 240 °C, indicating a higher mobility of Cd in the Cu-poor sample, which already happens at relatively low annealing temperatures. Continuing the annealing process, the Cd 4d photoemission signal of the Cu-poor sample decreases much faster compared to the one of the Cu-rich sample and vanishes completely towards the end of the annealing process, whereas traces of Cd on the Cu-rich sample still can be detected at 400 °C. This finding is directly connected to a significant dependence of the Cd diffusivity on the composition of the CIGSe absorber [27].

The resolution of HAXPES measurements in Figure 4.8-(a) is sufficient to assign the valence band maximum (VBM) with respect to the Fermi level. It was determined by linear extrapolation of the valence band onset with respect to the background level assuming a maximum error of ± 0.05 eV that strongly depends on the shape of the valence band edge. Two examples for the determination of the VBM with respect to the Fermi level are given in Figure 4.8-(b) and (c) for room temperature and 400 °C. The variation in the energetic position of the VBM will be discussed together with the binding energy position of the core level peak in Section 4.3.

Figure 4.9 represents atomic concentrations of the near surface elements Cu, In, Ga, Se, Cd, and S for all applied annealing steps in both samples. They were calculated from the corresponding photoemission core level peaks obtained for 3000 eV excitation energy assuming a homogeneous element distribution in the detected volume close to the surface. Under the assumption of a homogeneous element distribution; the depth, from where the concentration values were obtained was calculated to be approximately 12 nm, which is the information depth of In $3d_{5/2}$ photoelectrons (see Table 3.3). Before starting the evaluation, all spectra were corrected with respect to their binding energy using the position of the Au $4f_{7/2}$ peak at 84.0 eV [75]. After subtraction of a Shirley background, the spectra were integrated to determine the respective line intensities. Then, they were normalized to the corresponding inelastic mean free path λ (calculated by the TPP-2M

formula [106] using the QUASES code [107]), the transmission function of the analyzer *T*, the partial subshell photoionization cross-sections *dσ/dΩ*, which are tabulated in [111,112], and the intensity of the exciting x-ray beam I_0 to make them comparable to each other. This approach yields the normalized intensity of the corresponding photoemission peaks and eliminates all the energy-dependent factors, which allows the calculation of the respective atomic concentrations in a given depth.

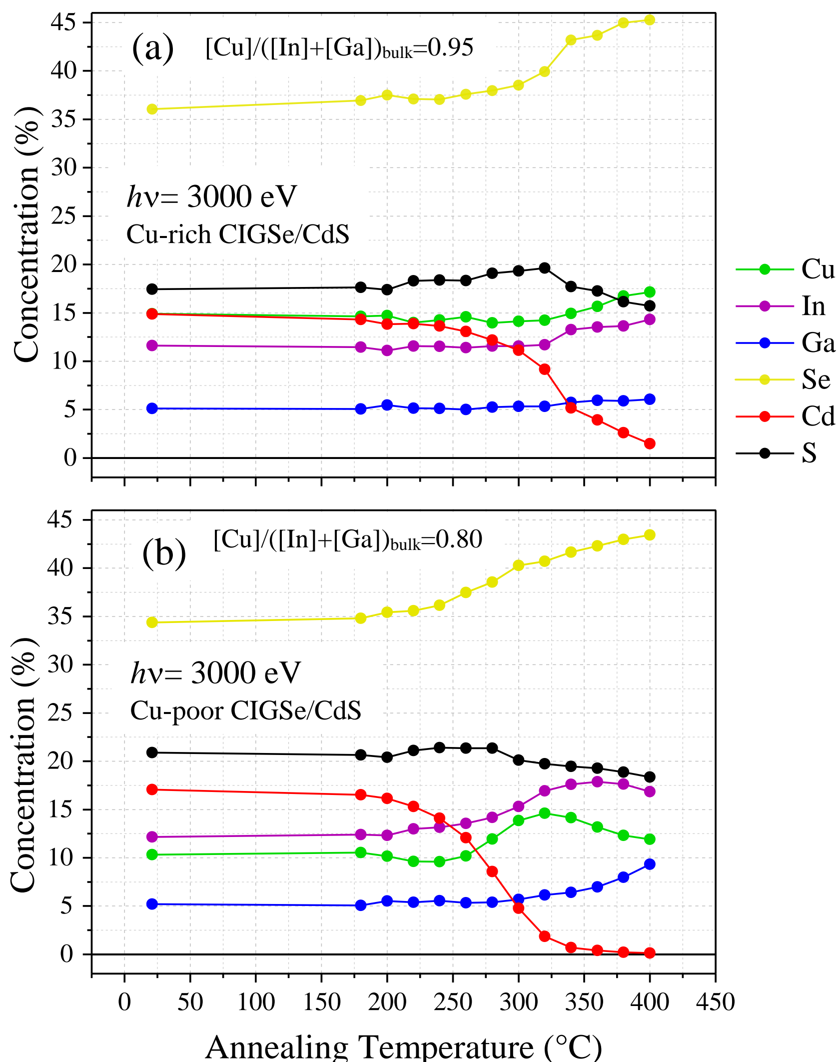

Figure 4.9 Concentrations of the Cu, In, Ga, Se, Cd and S species of the CdS coated, (a) Cu-rich and (b) Cu-poor CIGSe samples. The concentration values were calculated from the line intensities of the corresponding core level peaks which were recorded at 3000 eV excitation energy. The concentrations are so calculated that the sum of them gives 100 %. Assuming a homogeneous element distribution in the detected volume, the concentration values are obtained from a depth of about 12 nm. Solid lines are guides for the eye only.

Another representation of the atomic concentration of the near surface elements is given in Figure 4.10. There, the evolution of the atomic concentration of each species is shown with respect to their concentration at room temperature, where the concentration of each species was set to 100%.

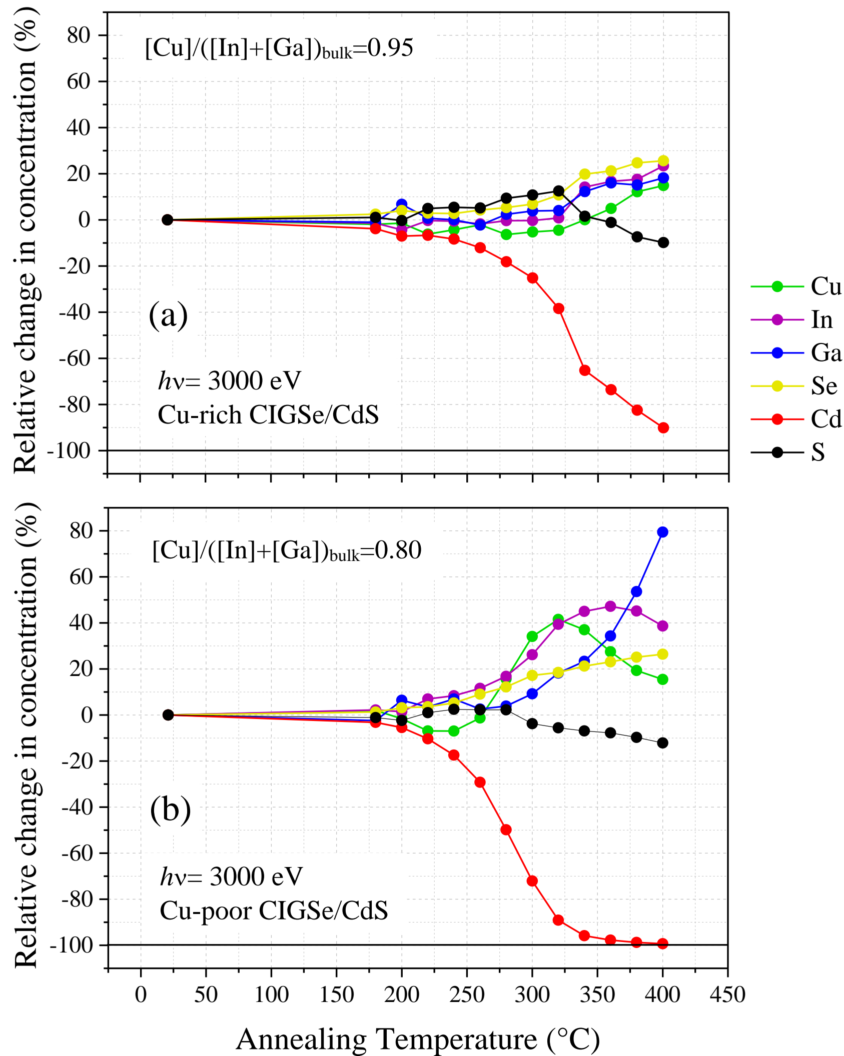

Figure 4.10 Evolution of atomic concentration of the Cu, In, Ga, Se, Cd and S species of the CdS coated, a) Cu-rich and b) Cu-poor CIGSe samples with respect to the room temperature measurements as the reference. Solid lines are guides for the eye only.

The most striking result is the complete disappearance of the cadmium signal from the CdS-coated, Cu-poor CIGSe surface after annealing at about 340 °C. This is in strong contrast to the observation on the Cu-rich surface, where Cd remains even after annealing at 400 °C. Since both samples were prepared simultaneously and heated under the same conditions, which gives rise to an identical CdS buffer layer thickness, this can be ruled out to explain the different temperature dependence

of the disappearance of the Cd signal. In addition, desorption is unlikely since the applied annealing temperatures are far away from the evaporation temperature of CdS which is strongly correlated to the partial pressure of the material that is insignificant at 400 °C [139]. This argumentation is also supported by the presence of sulfur on both samples, which then should also vanish like Cd since CdS is known to evaporate congruently. Therefore, it is assumed that the disappearance of Cd on the CIGSe surface is due to the diffusion of Cd into the CIGSe bulk material of the Cu-poor grown sample where Cd ions are believed to occupy empty Cu sites. On the Cu-rich sample, the density of Cu vacancies is smaller, allowing less Cd to penetrate into the bulk region of the absorber. Thus, the disappearance of Cd on the Cu-poor surface is interpreted as a dilution process of Cd up to a concentration of about 0.1 at.%, which is not detectable by XPS anymore [140]. In contrast, Cd is still visible on the surface of the Cu-rich sample within the detection limit of XPS. The diffusion of Cd into CIGSe is subject of several papers, both theoretical [3,9,10,141,142] and experimental [15,27,28,59,120,128,129,138,143–156], and it is assumed that the occupation of Cu^{+}-sites by Cd^{2+} is an important step within the interface formation [51].

In order to visualize the dependence of the Cd diffusion on the type of the substrate within the selected temperature regime, Figure 4.11 shows the first derivative of the Cd concentration curves for the Cu-poor and Cu-rich CIGSe+CdS samples over the annealing temperature.

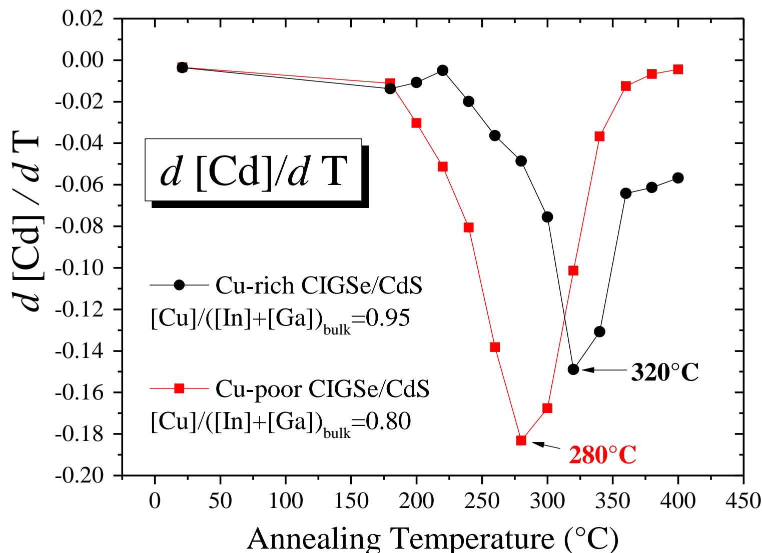

Figure 4.11 Derivative of the Cd concentration curve of the Cu-poor and Cu-rich CIGSe+CdS samples over the annealing temperature. Solid lines are guides for the eye only.

The red curve representing the derivative of the Cd concentration/temperature curve of the Cu-poor CIGSe+CdS sample has a minimum at 280 °C, which represents the point of inflection of the original curve (see the red curve in Figure 4.9-(a)). In comparison, the black curve of the Cu-rich CIGSe+CdS sample has its minimum at 320 °C, which is significantly higher. Using a simple estimation based on the ideal gas equation, these temperature values can be converted into a “free” energy using E=kT with k as Boltzmann constant. By doing this, energy values of 48 meV and 51 meV are obtained for the Cu-poor and Cu-rich CIGSe+CdS sample, respectively. Although the energy difference at 3 meV is small, a clear tendency for an increased activation energy of Cd diffusing into the Cu-rich sample compared to the Cu-poor sample is concluded. It is evident that the Cd diffusion strongly depends on the [Cu]/([In]+[Ga]) ratio.

In Figure 4.9 and Figure 4.10, the concentrations of the Se and S species vary within their corresponding information depth in a similar way during the annealing of both the Cu-poor and Cu-rich CIGSe+CdS samples. However, the concentration curves of the Ga, In and Cu species behave differently for Cu-poor and Cu-rich samples.

The Ga concentrations for both samples are almost constant at 5 % up to 280 °C and increase to 9 % and 6 % after the final annealing step at 400 °C for the **Cu-poor** and **Cu-rich** sample, respectively (Figure 4.9). This corresponds to an annealing induced increase in Ga concentration by 80 % (Cu-poor) and 10 % (Cu-rich) relative to the room temperature measurement, as it can be clearly seen in Figure 4.10. At this point, it is clear that the Ga atoms within two different samples at hand behave fundamentally different, which is probably influenced by the Cu content of the substrate material like in the case of Cd diffusion. Different scenarios for Ga diffusion in both samples and possible binding partners after the diffusion processes will be discussed later on in this chapter together with the shift in binding energy of Ga 2p and the variation of its full width at half maximum (FWHM).

The In concentration of both samples is 12 % at room temperature. It increases continuously with temperature to 17 % for **Cu-poor** sample when annealing up to 320 °C (Figure 4.9-(b)). This corresponds to a relative increase of about 40 % (Figure 4.10-(b)). Further annealing up to 400 °C does not influence the In concentration that much and it remains almost constant at 17 %. In case of the **Cu-rich** sample, a significant variation in the In concentration is not observed between room temperature and 320 °C and it slightly increases to 14 % at 400 °C (Figure 4.9-(a)). Besides, the

evolution line of the In concentration in Figure 4.10-(a) follows the shape of the Ga line. Accordingly, the slight increase in In concentration between 320 and 400 °C is attributed to a dilution of the CdS overlayer, which attenuates the XPS signals of the substrate. Therefore, a significant diffusion of In in this specific Cu-rich sample is not expected. On the other hand, many research groups [128,143,149,151] reported In diffusion from $CuIn(Ga)Se_2$ into the CdS layer, whereas Soo et al. [147] observed no In migration in a heterojunction between CdS and $CuInSe_2$ single crystals. That means there is a strong correlation between the In diffusion and the type of the substrate material, like it is shown in Figure 4.9 and Figure 4.10 at least at the interface between Cu-poor/Cu-rich CIGSe and CdS and between the selected temperature regime up to 400 °C.

The Cu concentration of the **Cu-rich** sample is about 15 % for the measurement at RT and remains almost constant up to 320 °C. Afterwards, the Cu concentration starts to increase slightly and reaches a value of about 17 % towards the end of annealing process at 400 °C (Figure 4.9-(a)). On closer inspection, the evolution line for the Cu concentration in Figure 4.10-(a) exhibits a smoother transition than the In and Ga lines during the annealing, especially between 320 °C and 400 °C, which can be a marker for a tendency of the formation of a Cu-poor surface in a thermodynamically unbalanced state. The Cu concentration of the **Cu-poor** sample starts at about 10 % under RT conditions, which is significantly smaller than on the Cu-rich sample. Indeed, the Cu concentration (green line in Figure 4.9-(b)) behaves unexpectedly during the annealing process. At the beginning (180 °C) it has the same value as for the RT measurement and in the following it remains almost constant until 240 °C. Starting from 240 °C, the Cu concentration increases continuously and reaches a maximum value of 15 % at 320 °C. Then, it starts to decrease after 320 °C and finally drops down to 12 % at 400 °C. The unexpected behavior of the Cu concentration on the Cu-poor sample during the annealing process is discussed in the following together with the Cd diffusion and the variation of Ga concentration in the last stage of the annealing process.

Figure 4.12 compares the [Cu]/([In]+[Ga]) (CGI) and [Ga]/([In]+[Ga]) (GGI) ratios as a function of annealing temperature for both samples under investigation. In case of the Cu-rich sample, the CGI and the GGI remain almost constant (0.88 and 0.31) between 180 °C and 400 °C, which stands for a constant Cu/III and Ga/III distribution within the probed depth. In case of the Cu-poor CIGSe+CdS sample, the CGI ratio follows a wave, similar to the evolution of the Cu concentration with increasing annealing temperature (see Figure 4.9-(a)). The GGI ratio of the Cu-poor sample has almost a constant value of 0.3 up to 240 °C and decreases slightly to 0.26 at 320 °C.

Surprisingly, the GGI value starts to increase continuously after 320 °C and reaches a value of 0.36 at the end of the annealing process at 400 °C. This increase in GGI is due to the increase of the Ga concentration (see Figure 4.10-(a)) and it is probably because of a Ga diffusion towards the CIGSe surface during the last stage of the annealing process. If this is the case, this would also explain the reduction of the partial Cu concentration on the surface (see Figure 4.9-(a)) and thus give a reason for the wave-like shape of the CGI ratio of the Cu-poor sample (see Figure 4.12 (left)). However, these unexpected findings concerning the Ga concentration and the according CGI values can be also explained by a diffusion of Cu towards the back-contact region of the thin film solar cell.

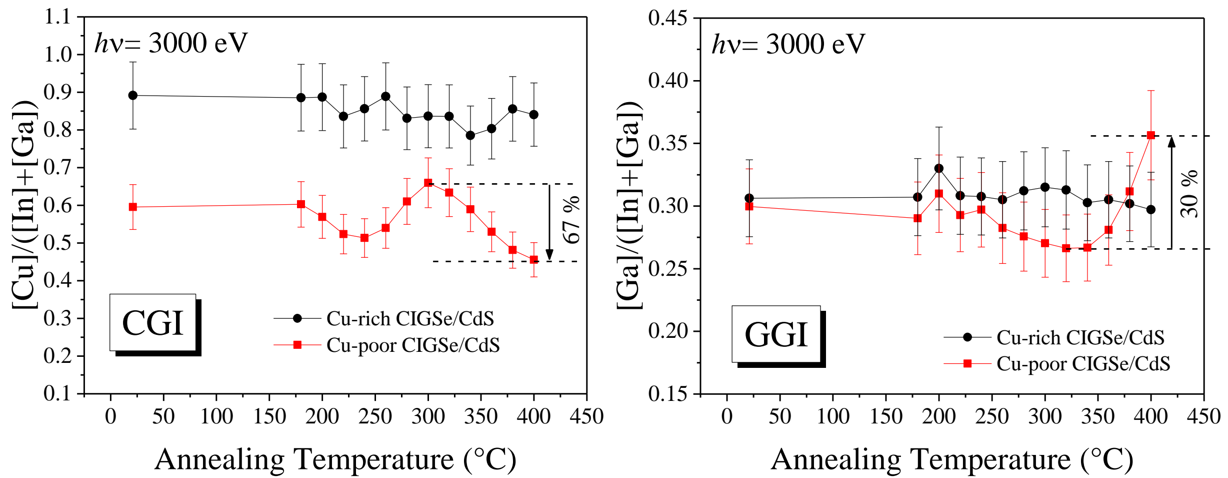

Figure 4.12 Selected concentration ratios as derived from normalized intensities. [Cu]/([In]+[Ga]) (CGI) (left) and [Ga]/([In]+[Ga]) (GGI) (right) obtained with an excitation energy of 3000 eV as a function of the annealing temperature. Solid lines are guides for the eye only.

Schröder et al. [157] studied the Ga diffusion in epitaxial $Cu(In_x,Ga_{1-x})Se_2$ layers on (111)B-oriented GaAs as a function of the Cu/In ratio. They used the GaAs substrate as Ga source and performed the CISe deposition without any direct Ga supply from effusion cells. They found a higher Ga diffusivity in the CISe material when moving the Cu/In ratio away from the stoichiometric point into the Cu-poor regime. They claimed that in case of Cu-poor (Cu/In < 1.0) CISe, Ga atoms occupy Cu-vacancies forming Ga_{Cu}^{+} defects, which in turn causes the formation of further V_{Cu}^{-} defects in order to maintain charge neutrality. These findings also explain the different evolution of the Ga concentration in our experiment during the annealing process depending on the usage of Cu-poor or Cu-rich CIGSe (Figure 4.10).

In case of the Cu-rich sample, the CGI ratio is very close to one - there are not enough Cu vacancies for Ga available to diffuse into the bulk. For that reason, the Ga concentration in Figure 4.9-(a) and the CGI-GGI ratios in Figure 4.12 are more or less unchanged during the annealing. In case of the Cu-poor sample, two stages can be identified. In the first stage (up to 320 °C) the Ga concentration remains constant and the Cu-vacancies are mainly occupied by Cd atoms, forming Cd_{Cu}^{+} defects. In the second stage (between 320 °C and 400 °C), Cd atoms diffuse further into the "bulk" leaving the initial Cu-vacancies behind. Now, Ga atoms occupy the new V_{Cu}^{-} sites by diffusion towards the surface. On the other hand, although the 30 % increase (from 0.27 to 0.35) of the GGI ratio in the second stage (Figure 4.12) can be explained by the diffusion of Ga into V_{Cu}^{-} sites, the 67 % decrease (from 0.66 to 0.44) of the CGI ratio cannot be explained only by the Ga diffusion process. For that reason, although highly speculative at this point, it can be concluded that the Ga diffusion towards the CIGSe surface causes the formation of new V_{Cu}^{-} defects as discussed by Schröder et al. [157].

The wave-like evolution of the Cu concentration in the Cu-poor sample in Figure 4.9-(a) and Figure 4.10-(a) can be explained in the light of the theoretical investigation, which is presented in Section 4.1. Namely, in the first stage of the annealing process up to 320 °C, the high number of pristine Cu vacancies (V'_{Cu}) at the near-surface region are occupied by the Cu atoms originating from the *near-bulk region*[1] and leave behind newly created Cu vacancies (V^{*}_{Cu}). This is reflected in Figure 4.9 and Figure 4.10 with an increase of Cu concentration in the near-surface region. The decrease in Cd concentration implies that the Cd atoms diffuse into the newly created V^{*}_{Cu} vacancies in the near-bulk region. As a result, the Cu atoms accumulate in the near-surface, whereas the Cd atoms diffuse into the near-bulk region, so the Cd concentration in the near-surface region reduces from 17 % to 2 %. Between the annealing temperatures 320 and 400 °C, the Cd atoms diffuse further into the bulk via Cu vacancies or through the hexagonal channels like in the case of the Cu-rich sample and the Cd concentration in the near-surface becomes 0 %. As the Cd atoms leave their site (V^{*}_{Cu}), the accumulated Cu atoms diffuse back into their original positions, which is reflected as a decrease in Cu concentration from 15 % to 12 % in Figure 4.9-(a). Now, the Cu vacancies are again free to host other diffusing atoms, for instance Ga atoms [157]. The experimental findings are summarized in a schematic diagram in Figure 4.13.

[1] The term "near-bulk region" is used here to describe the nearest region to the near-surface, exceeding the detection limit of the surface sensitive XPS.

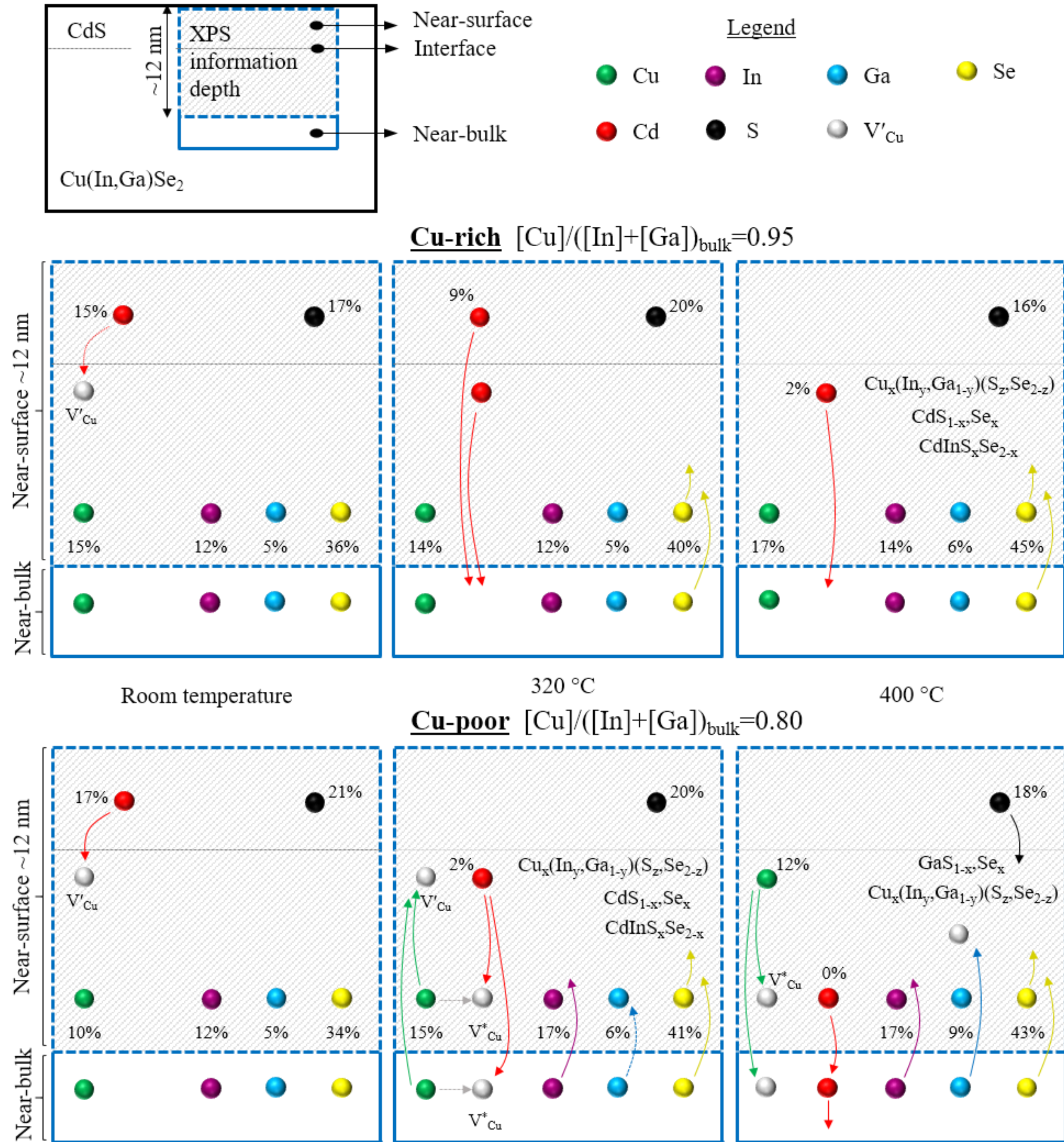

Figure 4.13 Schematic diagram summarizing the diffusion processes at three critical temperatures (room temperature, 320 °C and 400 °C, respectively) in case of Cu-rich and Cu-poor CIGSe/CdS samples. The % atomic concentrations are indicated close to the corresponding spheres, which were previously shown in Figure 4.9. The compounds that are possibly formed due to the diffusion processes are indicated as well close to the interface region, which is the subject of the Section 4.3. Assuming a homogeneous element distribution, the detection depth was calculated to be about 12 nm, which is shown by a dashed rectangle. The thickness of the CdS overlayer is less than 10 nm.

4.3 Chemical Changes at the Cu-rich and Cu-poor CIGSe/CdS Interface upon Annealing

In this section, in order to study the possible chemical changes at the Cu-rich and Cu-poor CIGSe/CdS interfaces upon the annealing process, the positions of the binding energy of the CIGSe- and CdS-related core level peaks are analyzed in detail.

Figure 4.14 summarizes the positions of binding energy of the CIGSe- and CdS-related core level peaks (Figure 4.14 (a)-(f)) and the valence band maximum with respect to the Fermi level (Figure 4.14-(g)) in the course of the annealing process of the Cu-poor and Cu-rich CIGSe/CdS sample. Figure 4.14 will be discussed in detail in the following together with Figure 4.15, where the relative shifts in binding energy (ΔE) of the corresponding core level peaks and the valence band maximum with respect to the room temperature measurements are depicted. The green-highlighted dashed-lines in Figure 4.15 show the general trend in the relative shift of the binding energy of the corresponding peaks with a separation of about 0.1 eV, being the uncertainty in the determination of the peak positions.

In case of the Cu-rich sample (Figure 4.14, black lines), all the absorber- and the buffer-related core levels (except S 1s) and valence band maxima are shifting more or less similarly within the annealing process. This is clearly shown in Figure 4.15-(b) with the dashed lines as a trend of the core level shift. These shifts point to a slight band bending at the Cu-rich CIGSe/CdS surface induced by the heat treatment.

In case of the Cu-poor sample, the last three data points of the Cd $3d_{5/2}$ peak are missing in the graph (Figure 4.14-(e)) because of the disappearance of the Cd signal at elevated annealing temperatures above 360 °C (see Figure 4.7-(e)). Similar to the Cu-rich sample, Cu-poor CIGSe/CdS-related core levels (except S 1s) and valence band maxima shift in a similar way over the whole annealing process pointing to a dedicated band bending at the Cu-poor CIGSe/CdS surface as well (see the dashed lines in Figure 4.15-(a)).

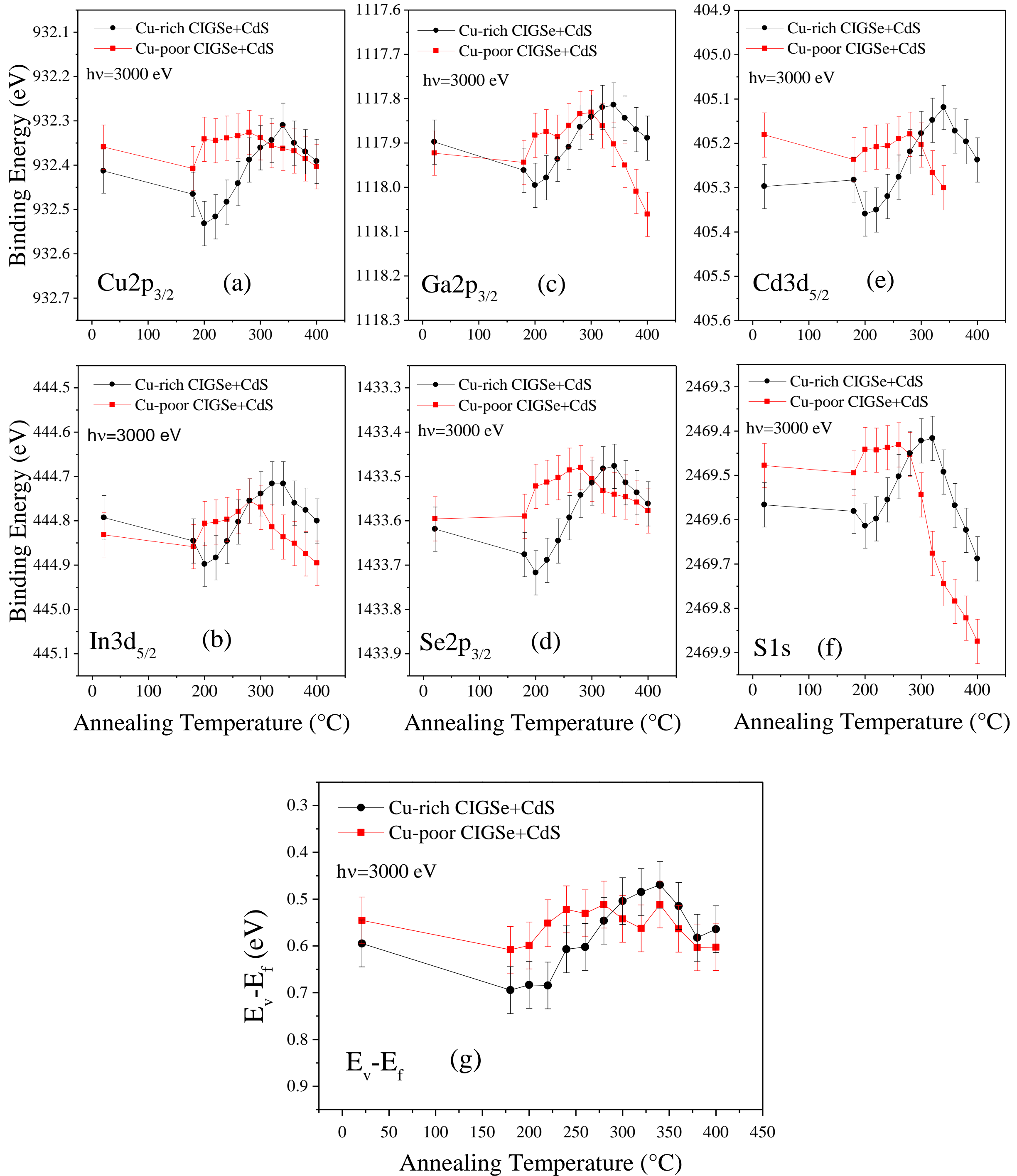

Figure 4.14 Comparison of the binding energies of the considered peaks (a-f) and the valence band maxima (g) in the course of the annealing process in case of Cu-rich (black) and Cu-poor (red) CIGSe/CdS samples (sample #1 and sample #2 in the Table 3.1, respectively). The measurements are performed at 3000 eV excitation energy (corresponds to an information depth of between 4 nm and 12 nm depending on the core level signal) and the error is assumed to be ±0.1 eV. Solid lines are guides for the eye only.

For the Cu-rich sample, the evolution of the binding energy of the S 1s peak over the annealing temperature goes along with the one of the Cu-poor sample up to 360 °C, where the concentration of Cd starts to fall under 5 %. Since the sulphur concentration is only weakly influenced by the annealing process, although the Cd concentration tends to decrease to zero, the shift in the binding energy of the S 1s peak can be considered as an indicator for a change in the chemical environment of sulphur after respective annealing temperatures have been applied. This can be seen more clearly in Figure 4.15, where the relative shift in S 1s binding energy drops out of the band bending region between the dashed lines, pointing to a change in its chemical environment, which is more prominent for the Cu-poor sample. The shift in the binding energy of the S 1s signal in the Cu-poor sample already starts at lower annealing temperatures around 280 °C (see Figure 4.15). This is probably due to the fact that the Cd diffusion also starts at lower temperatures for the Cu-poor sample (see Figure 4.9) changing the chemical environment of sulphur by forming other compounds than CdS. Additionally, the overall shift of the S 1s signal on the Cu-poor sample is with about 0.4 eV larger than on the Cu-rich sample (Figure 4.15). This is probably because of the complete disappearance of the Cd from the surface, where the remaining sulphur forms a completely Cd-free compound.

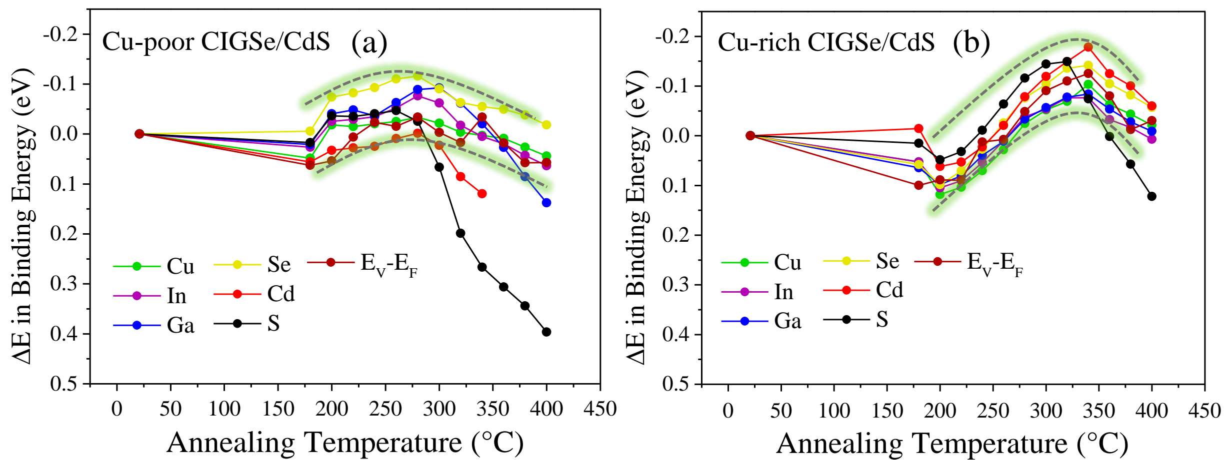

Figure 4.15 Relative shifts of the binding energies of the considered core level peaks and the valence band maximum of the Cu-poor and Cu-rich CIGSe/CdS samples with respect to the room temperature measurements as the reference. The measurements are performed at 3000 eV excitation energy and the error is assumed to be ±0.1 eV. The error bars are not included in the graphs for the clarity. Solid lines are guides for the eye only.

On closer inspection of Figure 4.15-(a), comparing the dashed lines and the blue points, it can be seen that the relative shift in binding energy of Ga 2p drops down sharper than the general trend of the band bending. This is another indication that the Ga atoms diffuse towards the near-surface in the last stage of the annealing process (as discussed above) and form a new compound.

Since the S 1s core level electrons have a binding energy in the range of 2470 eV and thus cannot be excited with standard laboratory x-ray sources (Mg Kα and Al Kα), there are limited reference data available in the literature for S 1s binding energies for different compounds. However, the reference data for S 2p binding energies, which is widely available in literature, can also give a hint about the binding state of the rest of the sulphur after the complete Cd diffusion at the end of the annealing process. The reference data for the binding energies of some core levels is listed in Table 7.2 in Appendices. The binding energy of the S $2p_{3/2}$ core level lies between 161.0 eV and 162.2 eV. However, statistically, a higher number of references measured the binding energy between 161.4 eV and 161.8 eV. Landry et. al. [158] compared the S $2p_{3/2}$ binding energy for two different compounds, namely $CuInS_2$ and CuInSSe and they measured 161.8 eV and 162.0 eV, respectively. That means, the addition of Se into the compound shifts the binding energy of the S 2p to higher values. This finding can explain the slight shift of the S 1s signal to higher binding energies and point to the formation of a $CdS_{1-x}Se_x$ compound at the last stage of the annealing process of the Cu-rich sample. This compound formation was also shown by Heske et. al. [128] using a combination of x-ray emission spectroscopy and x-ray photoelectron spectroscopy. Additionally, Melitesta et al. [159] observed a S $2p_{3/2}$ binding energy of 161.9 eV for the $CdIn_2S_2Se_2$ compound, which is statistically a higher value than that of the CdS compound. Heske et al. [128] showed also this mixed compound to be formed as an intermediate layer. Although the chemical shift in S1s binding energy is in the order of 0.1 eV at 400 °C for the Cu-rich sample (Figure 4.14-(f) and Figure 4.15-(b)), it can be taken as a sign for an annealing-induced formation of a highly intermixed interface containing $CdS_{1-x}Se_x$- and/or $CdIn_2S_2Se_2$-like compounds (see Table 4.1 for the formation of some possible compounds as described by Guillemoles et al. [3].

The above discussion is valid also for the Cu-poor sample up to 320 °C. In this case, the S 1s signal shows a shift of 0.4 eV after the last annealing step at 400 °C, with respect to its initial state at room temperature. The disappearance of Cd points to the formation of a Cd-free compound. In addition, a continuously increasing Se concentration implies a Se-containing compound. Together with the Ga-enrichment within the probed depth and the reference data in Table 7.2 in Appendix,

a $GaS_{1-x}Se_x$ compound [160] seems to be very likely formed, although the formation of a mixed compound $Cu_x(In_y,Ga_{1-y})(S_z,Se_{1-z})$ cannot be excluded. The Cu concentration in the mixed compound tends to decrease with increasing temperature after 320 °C (Figure 4.9 and Figure 4.12). Therefore the formation of a completely Cu-free compound in the very near surface region [131,157], like $(In_y,Ga_{1-y})(S_z,Se_{1-z})$ should be also considered.

An additional way to get a hint about the changed chemical environment of the corresponding species is to refer the full width at half maximum (FWHM) values of the considered core level peaks in the course of the annealing process. These are tabulated in Table 7.3 in Appendix for both Cu-poor and Cu-rich samples and the variation of them during the annealing is shown in Figure 4.16.

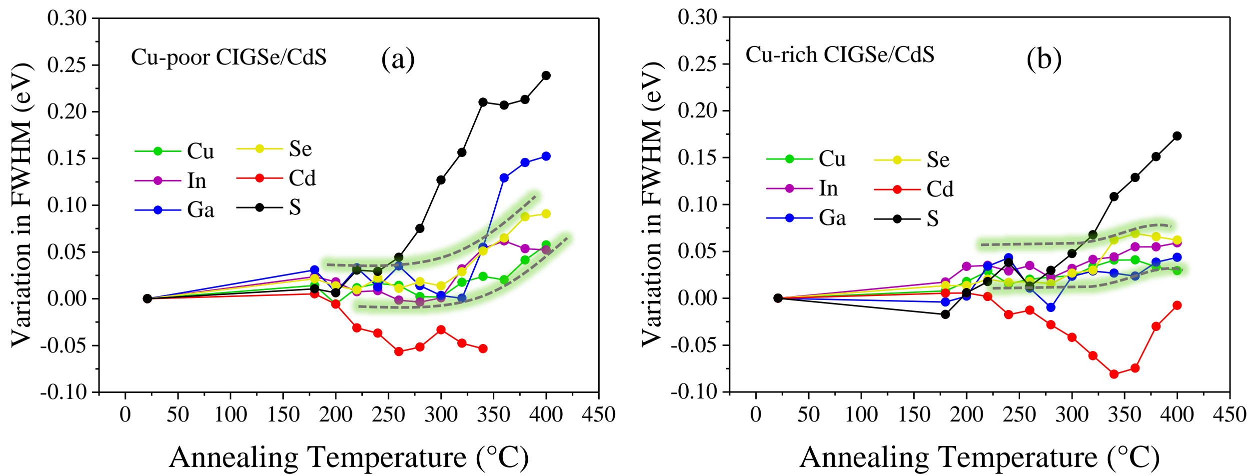

Figure 4.16 Variation in full width at half maximum (FWHM) values of the considered core level peaks in the course of the annealing process in case of (a) Cu-poor and (b) Cu-rich CIGSe/CdS samples. All values at room temperature are set to 0 for a clear presentation. Solid lines are guides for the eye only.

The general trend of the variation in FWHM is indicated with the dashed lines. The FWHM values of Cd 3d and S 1s for both samples are highly influenced by the annealing process as expected, since the Cd atoms diffuse into the substrate, leaving behind the S atoms to form Cd-free compounds. Additionally, Figure 4.16-(a) shows that the FWHM value of Ga 2p deviates strongly from its original value starting from 320 °C in case of the Cu-poor sample. This finding supports the above discussion, that the Ga atoms diffuse towards the CIGSe surface (see Figure 4.9-(b) and Figure 4.10-(b)) and fill the Cu vacancies at elevated temperatures between 320 °C and 400 °C, so

that the Ga atoms form a $GaS_{1-x}Se_x$ secondary phase in the near-surface region. The possibility of the formation of a $GaS_{1-x}Se_x$ compound is also thermodynamically supported by Guillemoles et al. [3] (see Table 4.1) as will be discussed in the following.

Guillemoles et al [3,142] studied the stability of the CIGSe/CdS interface thermodynamically. They calculated free energies of reaction for some of the relevant reactions at the CIGSe/CdS interface at room temperature, which are given in the first column of the Table 4.1. The other free energies of the reactions at elevated temperatures up to 800 K are calculated using the standard free energies (G°) of the corresponding compounds that are listed in Table 7.4 in Appendix [161]. Accordingly, the formation of Ga-containing compounds, rather than their In-containing counterparts, such as Ga_2S_3 is highly expected, depending upon the Ga concentration. The low free energy of about −78 kJ/mol for the reaction #3 suggests an additional explanation for the tendency of the Ga diffusion towards CIGSe surfaces in the second stage of the annealing (between 320 °C−400 °C) in case of the Cu-poor sample to form a $GaS_{1-x}Se_x$ secondary phase at the near-surface. The other reactions in the Table 4.1 suggest that the formation of $CdS_{1-x}Se_x$, $CdIn_2S_2Se_2$ and $GaS_{1-x}Se_x$ compounds is at least thermodynamically not forbidden (for the growth and some properties of these compounds, refer to [162–165]), as it was discussed above in terms of the shift in the binding energy of the S 1s core level (Figure 4.14-(f) and Figure 4.15) and the variation in the FWHM values (Figure 4.16).

Table 4.1 Free energies of reaction for some of the relevant reactions at the CIGSe/CdS interface at different temperatures. Adopted from [3,161].

		ΔG kJ/mol						
#	Reaction \ Temperature (K)	298	300	400	500	600	700	800
1	$Cu_2Se + CdS \rightarrow Cu_2S + CdSe$	−5.6	−5.6	−5.7	−5.3	−5.1	−5.0	−5.2
2	$In_2Se_3 + 3CdS \rightarrow 3CdSe + In_2S_3$	0.1	0.1	1.4	3.8	7.3	11.4	15.8
3	$Ga_2Se_3 + 3CdS \rightarrow 3CdSe + Ga_2S_3$	−78.1	−78.1	−77.1	−75.9	−74.5	−72.9	−71.2
4	$In_2Se_3 + CdSe \rightarrow CdIn_2Se_4$	<0	−	−	−	−	−	−
5	$In_2Se_3 + CdS \rightarrow CdIn_2SeS_3$	<−11.9	−	−	−	−	−	−

4.4 Summary

In this chapter, ab-initio density functional theory (DFT) calculations on the correlation between the diffusion properties of Cd atoms with the copper contents of the CIGSe compounds are presented. The DFT calculations were carried out by the ComCIGS-II project partners J. Kiss and H. Mirhosseini from the Max-Planck-Institute for Chemical Physics of Solids [11]. The experimental proof of the theoretical considerations is done using a photoelectron spectroscopy method, i.e. HAXPES. The experimental findings of this chapter together with the main results of the DFT calculations are summarized in the following.

The Cd diffusion of a CdS top layer into the differently grown Cu-poor and Cu-rich $Cu(In,Ga)Se_2$ materials was investigated upon the annealing process in UHV, at temperatures ranging from 180 to 400 °C in steps of 20 °C. For this purpose, ultrathin CdS layers with an estimated thickness of less than 10 nm were deposited by CBD on both absorbers.

HAXPES measurements using an excitation energy of 3000 eV (resulting in an information depth up to ~12 nm) revealed that the Cd atoms can diffuse into the CIGSe material already during the CBD process, where they occupy the pristine Cu vacancies (V'_{Cu}), thus more prominent in Cu-poor samples. Moreover, DFT calculations indicated that the diffusion mechanism of Cd differs fundamentally with respect to the Cu concentration of the CIGSe absorber material. Namely, the Cd diffusion in Cu-poor CIGSe is a two-step process, where Cu atoms are actively exchanged by Cd impurities during the diffusion process. The Cu-assisted, two-step diffusion process of Cd is reflected in the concentration profile of Cu upon the annealing process in the HAXPES measurements. In contrast to Cu-poor CIGSe, in case of the Cu-rich sample, the Cu atoms are not directly involved in the diffusion process but they indirectly play a role as V_{Cu} defects, where Cd impurities are being incorporated.

In addition, DFT calculations showed that the two diffusion mechanisms in Cu-poor and Cu-rich CIGSe/CdS interfaces are also quantitatively well distinguishable from the perspective of the activation energies (0.94 eV and 2.13 eV, respectively). By having the lower activation energy for Cd diffusion in the Cu-poor sample, no trace of Cd was detected by HAXPES at the near surface

region after the final annealing temperature 400 °C, whereas a small amount of Cd could be still measured within the same depth of the Cu-rich sample after the same annealing process.

Another distinct difference in the interface formation of Cu-poor and Cu-rich CIGSe/CdS samples upon the annealing process between the corresponding annealing temperatures is the Ga diffusion towards the CIGSe surface, forming secondary phases. In case of the Cu-rich sample, an indication for a Ga enrichment at the CIGSe/CdS interface was not observed. In contrast, a significant Ga diffusion towards the CIGSe surface was observed in case of the Cu-poor sample at elevated temperatures between 320 and 400 °C, where they probably occupy V_{Cu} sites. Together with the exchange process of S-Se at the interface, the variation in the binding energy and the FWHM of the S 2p and Ga 2p core levels pointed to the formation of a $GaS_{1-x}Se_x$-like compound at the interface. The high band gap of that compound in the range of 2.0-2.5 eV [166] may be one of the reasons for the efficiency degradation of the high efficiency solar cells (CGI≈0.8 and GGI≈0.3 in this study) at high annealing temperatures [127], as it would create a high conduction band offset at the heterojunction, being a barrier for electron transfer.

5 Impact of KF Post-Deposition Treatment on the $Cu(In,Ga)Se_2$/CdS Interface

Recent developments in $Cu(In,Ga)Se_2$ (CIGSe)-based thin film solar cells reported improvements in power conversion efficiencies when KF had been applied onto CIGSe absorbers [8,167–174]. Up to now, the underlying mechanism responsible for these efficiency improvements is unknown. Some groups reported grain boundary passivation due to the potassium fluoride post-deposition treatment (KF-PDT) [70,168], whereas other groups observed a general defect passivation [167,172]. Pianezzi et al. and Reinhard et al. showed a Cu-depleted CIGSe surface, resulting in a stronger near-surface type inversion from p to n-type conductivity [170,173]. Additionally, Chirilă et al. observed a much stronger Cu and Ga depletion of the near-surface region compared to the untreated absorber using surface sensitive x-ray photoelectron spectroscopy (XPS) [8]. They concluded that the increased Cu depletion at the CIGSe surface leads to an enhanced Cd diffusion into the absorber during the chemical bath deposition (CBD) of the CdS buffer layer even at low process temperatures. This phenomenon is also supported by theoretical studies conducted by Kiss et al. [9,10]. It was also demonstrated in the previous chapter that the amount of Cd diffusing into the interface region of the absorber during the CBD of the CdS is dependent on the Cu concentration [62]. By applying the approach of KF-PDT, Mansfield et al. [175] could obtain an efficiency increase from 17.1 % to 18.6 % in CIGSe solar cells made from the two-step selenization process. Beside these findings, Pistor et al. [38] and similarly Handick et al. [176] measured a shift in the valence band maximum towards higher binding energies with respect to the Fermi level by means of XPS. They explained this shift as a result of a band gap widening due to the Cu-depletion in the near-surface region of the CIGSe absorber because of KF-PDT. However, none of these

above-mentioned investigations have studied directly the impact of the KF-PDT on the CIGSe/CdS interface using a non-destructive analysis method.

In this chapter, first, the impact of the KF-PDT on the CIGSe/CdS absorber/buffer interface is investigated by means of non-destructive, hard x-ray photoelectron spectroscopy (HAXPES). The depth-resolved HAXPES is used here to gain a depth-dependent distribution of the constituent atoms, which form the interface.

Second, the ammonia etching of the CIGSe and the CIGSe+KF samples during the CBD process is investigated by means of XPS and UPS in order to distinguish the effect of KF-PDT and the deposition of CdS in an ammonia-containing solution (CBD) on the surface properties of CIGSe absorbers.

5.1 Analysis of CIGSe+KF/CdS and CIGSe/CdS Interfaces by Depth-Resolved HAXPES

The impact of KF post-deposition treatment (KF-PDT) on the Cu(In,Ga)Se_2/CdS interface is studied in this section. The CIGSe/CdS and the CIGSe+KF/CdS samples (i.e. sample #3 and sample #4, respectively, as presented in Table 3.1) are investigated using hard x-ray photoelectron spectroscopy at the HIKE end station. For the HAXPES measurements, excitation energies of 2030, 3000, 4000, 5000 and 6000 eV were used (for the information depths of the corresponding excitation energies and core level photoelectrons, see Table 3.3).

In Figure 5.1, survey spectra of the CdS covered standard and the KF-PDT treated CIGSe samples are shown for 6000 eV excitation energy in the binding energy range from 0 to 2500 eV. Since the thickness of the CdS film is limited to less than 10 nm, photoelectrons originating from the CIGSe absorber region still can be detected due to their increased kinetic energy, which goes along with an increased information depth of 16 nm to 24 nm as compared to standard XPS (see Section 3.2.1). In addition, cadmium and sulfur related peaks appear in the spectra as expected. Moreover, small quantities of carbon and oxygen are detected on both samples due to air contact after the absorber growth and due to the usage of aqueous solutions for the CBD of CdS. At first glance, both spectra look very similar, which emphasizes the high quality of the sample preparation. The fact that both,

deposit (CdS) and substrate (CIGSe) peaks are visible in the spectra, allows the investigation of the CIGSe/CdS interface with depth resolving HAXPES.

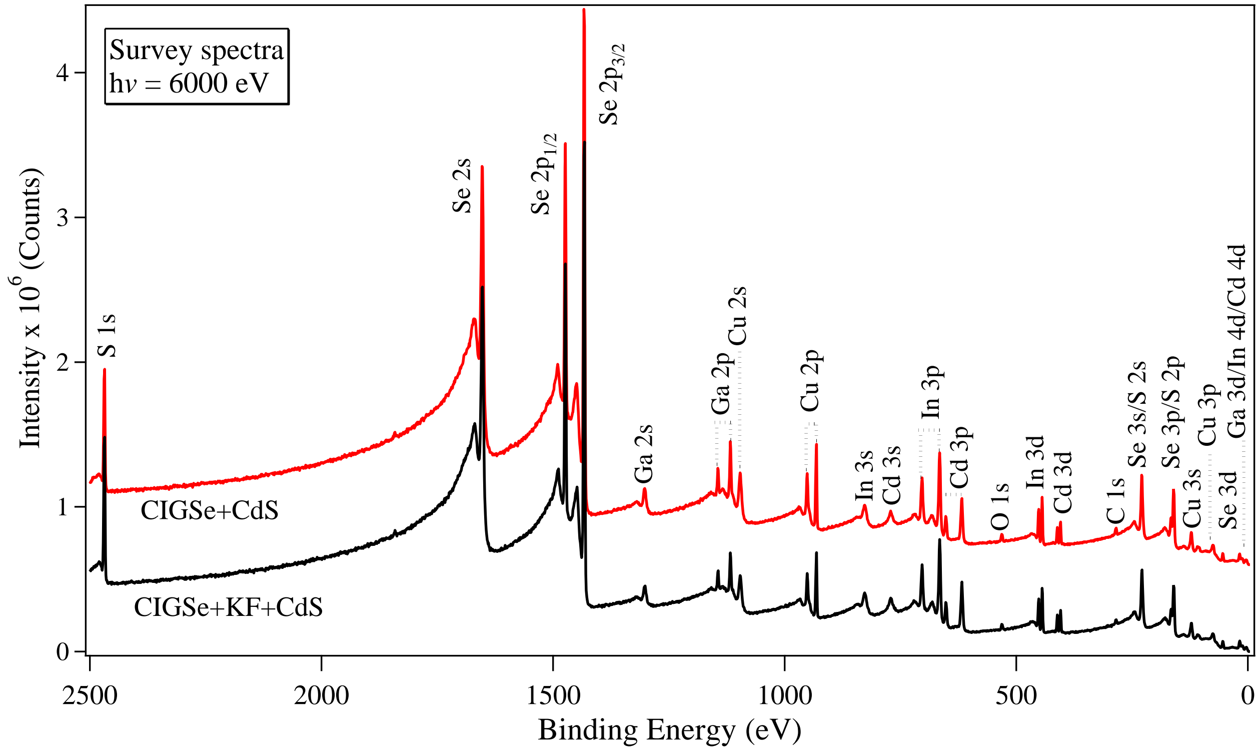

Figure 5.1: XP survey spectra of the standard CIGSe/CdS (red) and CIGSe+KF/CdS (black) sample measured at 6000 eV excitation energy (after Ümsür et al. [177]).

Figure 5.2 shows top view images of the standard CIGSe/CdS (a) and CIGSe+KF/CdS (b) samples obtained with SEM. The morphology of both samples appears very similar with homogenous crystalline structures up to a size of 500 nm, which can be related to different grains. The topmost CdS layer is not visible since the layer thickness is too small to be resolved with SEM. However, it is assumed that the CdS layer covers homogeneously the CIGSe absorber independent from morphology and structure of the surface due to the nature of the wet chemical deposition process [156] and due to the very small lattice mismatch between CIGSe and CdS, leading to an epitaxial structure [27]. Thus, the surface in the images mainly represents that of the bare CIGSe absorber. On a closer inspection, small precipitations with a diameter of less than 20 nm can be observed on the standard CIGSe/CdS sample (see Figure 5.2-(a)), which consist of $Cd(OH)_2$ according to [178]. In contrast, these entities are not visible on the KF-PDT CIGSe/CdS sample (see Figure 5.2-(b)). It seems that this phenomenon is related to the composition change at the CIGSe surface due to the

KF treatment, which leads to a lower near-surface Cu concentration as well as a higher near-surface Cd and S concentration as shown later. In the following, similar aspects are discussed on an electronic level based on the HAXPES spectra.

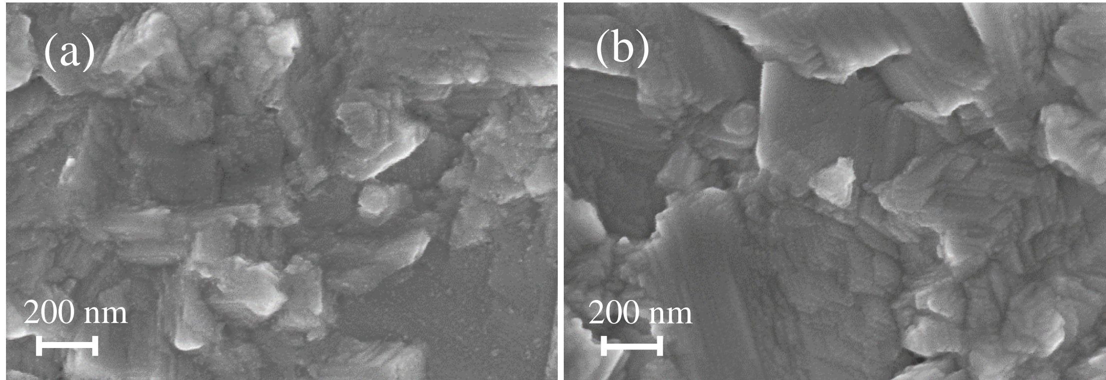

Figure 5.2: SEM top view images of the (a): standard CIGSe/CdS and (b): CIGSe+KF/CdS (sample #3 and sample #4, respectively, in Table 3.1), which were also measured with HAXPES (see Figure 5.1) (after Ümsür et al. [177]).

Figure 5.3 shows a compilation of normalized intensities derived from the Cu $2p_{3/2}$, In $3p_{3/2}$, Ga $2p_{3/2}$, Se $2p_{3/2}$, Cd $3d_{5/2}$, and S 1s peaks of the standard and the KF-PDT CIGSe/CdS sample. The shown values are calculated from the corresponding photoemission lines, which were measured with HAXPES at different excitation energies. Before starting the evaluation, all spectra were corrected with respect to their binding energy according to the position of the Au $4f_{7/2}$ peak located at 84.0 eV [75]. After subtraction of a Shirley background, the spectra were integrated in order to determine the respective line intensities. Then, they were normalized to the corresponding inelastic mean free path λ (calculated by the TPP-2M formula [106] using the QUASES code [107]), the transmission function of the analyzer T, and the partial subshell photoionization cross-section $d\sigma/d\Omega$ as tabulated in references [111,112]. The parameters λ, T, and $d\sigma/d\Omega$ depend on the kinetic energy and therefore they vary for different excitation energies. The normalization procedure takes this dependency into account, thus allowing the direct comparison of normalized intensities of one species measured with different excitation energy. Additionally, the top horizontal axis of each graph shows the information depth (ID) for the corresponding core level signals which correlates to the excitation energy and which is estimated using the formula $ID \approx 3\lambda$ [75]. The values vary approximately from 4 to 24 nm.

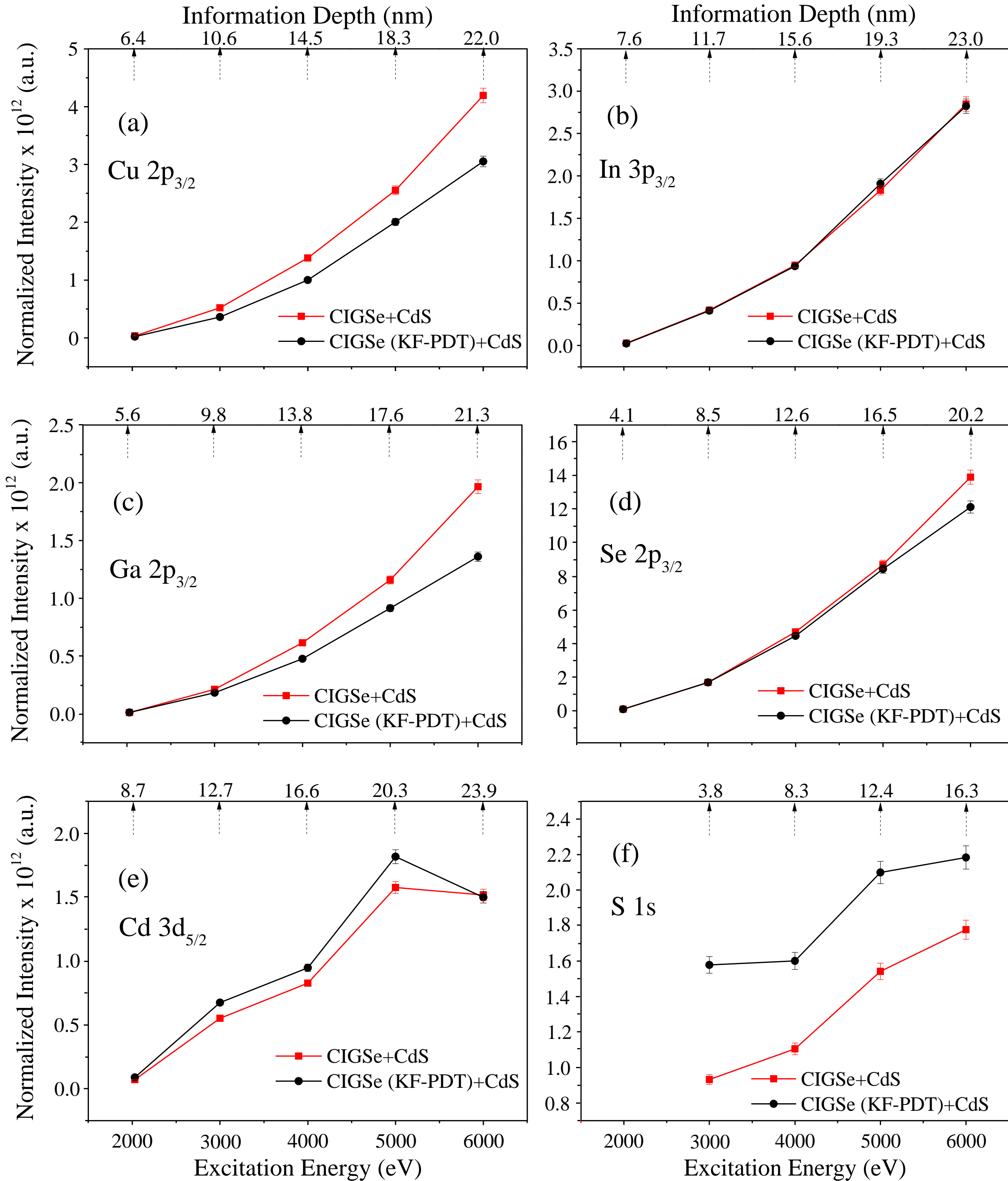

Figure 5.3: Normalized intensities (the normalization procedure is explained in the text) of absorber and buffer components as a function of excitation energy for the CIGSe/CdS (red) and the CIGSe+KF/CdS (black) samples. The top axis shows the according information depth. For 2030 eV, the normalized intensity values are missing for the S1s related core levels since they cannot be excited with this energy (after Ümsür et al. [177]). Solid lines are guides for the eye only.

In the considered information depth regime, the normalized core level line intensities of the In and Se species are almost identical for both, the standard (red) and the KF-PDT (black) CIGSe/CdS samples, whereas the line intensities of the Cu and Ga species clearly differ from each other with increased values of the standard (red) CIGSe/CdS sample compared to the KF-PDT (black) CIGSe/CdS sample. In addition, the buffer layer species Cd and S of both samples are compared in Figure 5.3-(e) and (f), respectively. Within the given information depth, the KF-PDT CIGSe/CdS sample shows a higher line intensity for both, the Cd and S species with the latter one being more significant. In a first approximation, this can be interpreted in terms of diffusion with Cu and Ga being repelled by the KF-PDT from the CIGSe/CdS interface and pushed further into the CIGSe bulk material while Cd and S are penetrating into the CIGSe interface region.

In Figure 5.4, another presentation of the same data is given by the ratio $I_{CIGSe(KF\text{-}PDT)+CdS}/I_{CIGSe+CdS}$ over the excitation energy for all involved species.

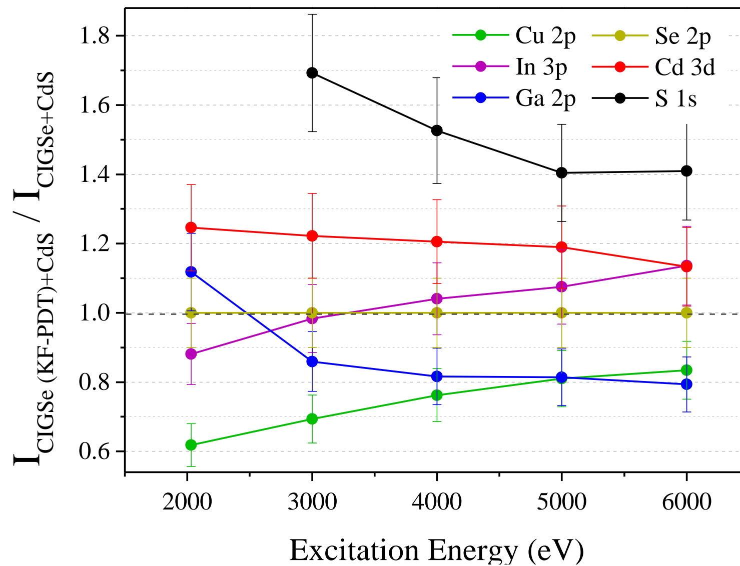

Figure 5.4: Ratio of different core level intensities of the CIGSe+KF/CdS and the CIGSe/CdS samples (sample #4 and sample #3, respectively, in Table 3.1). All values are referred to the Se related signal, which by definition is set to one for each excitation energy value (after Ümsür et al. [177]). Solid lines are guides for the eye only.

The shown values in Figure 5.4 are referred to the Se related signal, which by definition is set to one, assuming that the KF-PDT does not affect the Se concentration at the CIGSe surface as demonstrated in Figure 5.3-(d). The advantage of this approach is to avoid the dependency on λ, T, and $d\sigma/d\Omega$ due to cancelling, which otherwise might falsify the evaluation due to wrong

assumptions or systematical errors. In the energy range from 2000 to 6000 eV the Cu 2p signal steadily rises from 0.6 to 0.8 without crossing the reference line at one. This means that the Cu concentration in the KF-PD treated sample is always lower than in the standard sample. The fact that the Cu 2p signal is not constant over the given energy range even implies that the Cu deficiency is more pronounced in the topmost region of the CIGSe material. On the other hand, the Cd 3d signal behaves conversely and decreases steadily from 1.3 to 1.1 within the same energy range, which means that there is more Cd on the KF-PD treated CIGSe surface than on the standard one. Moreover, within an assumed error of ± 10 %, the In 3p value appears more or less constant and close to 1, which points to an equal near-surface distribution of In in both samples, similar to the Se case. However, a slight tendency for an In enrichment for higher excitation energies and thus deeper regions cannot be denied. A similar behavior but with an opposite effect can be found for the Ga 2p signal. There, an initial Ga excess turns into a significant depletion for higher energies. This is attributed to specific interface reactions during the CIGSe/CdS heterojunction formation. Nevertheless, the most pronounced difference is observed for the S 1s signal, which steadily goes from 1.7 to 1.5 within the given energy range of 3000 to 6000 eV. This means that on the KF-PD treated CIGSe sample, the amount of S is much higher than on the standard sample. This can be only explained by unknown effects during the CdS formation, which might be influenced by the Cu and Ga depletion. This point will be discussed later on together with other findings.

Figure 5.5 compares the [Cu]/([In]+[Ga]) (CGI), the [Ga]/([In]+[Ga]) (GGI), and the [Cd]/[Cu] ratios as a function of excitation energy for both samples under investigation based on normalized intensities. In case of the standard CIGSe/CdS sample, the CGI (see Figure 5.5-(a)) varies only slightly between 0.82 and 0.88, which stands for a homogeneous Cu/III distribution over the probed depth. On the other hand, the GGI (see Figure 5.5-(b)) rises strongly from 0.29 to 0.40 below 4000 eV before it stabilizes. In contrast, this behavior is completely different for the KF-PDT CIGSe/CdS sample.

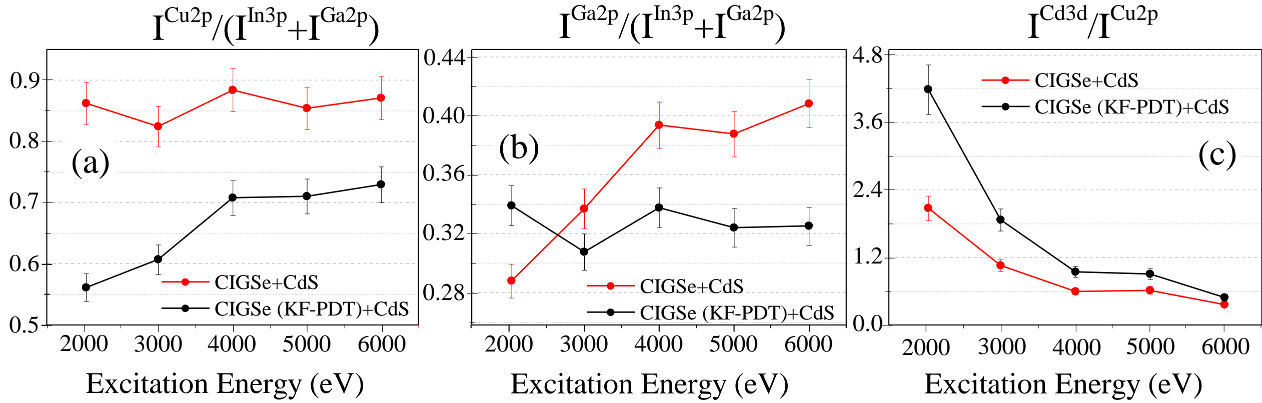

Figure 5.5: Selected concentration ratios as derived from normalized intensities. (a) [Cu]/([Ga]+[In]) (CGI), (b) [Ga]/([Ga]+[In]) (GGI), and (c) [Cd]/[Cu] as a function of excitation energy (after Ümsür et al. [177]). Solid lines are guides for the eye only.

The CGI in Figure 5.5 starts at a relatively low value of 0.55 before it stabilizes at 0.71 whereas the GGI remains almost constant with a value of 0.32 over the considered sample depth range. On closer examination, it seems that there is a correlation between both parameters (CGI and GGI). While for the standard CIGSe/CdS sample the CGI rises and the GGI is constant with increasing depth, the same parameters behave in the opposite way for the KF-PDT CIGSe/CdS sample on a lower level. On both samples, the CGI affects the GGI and vice versa. Considering the shape of the Cd/Cu ratio, this is similar for both samples. In the lower excitation energy range it starts at 4.2 and 2.1 for the KF-PDT and the standard CIGSe/CdS sample, respectively. For higher excitation energies, it approaches zero, which implies a depth-limited diffusion of Cd into the CIGSe absorber.

In Figure 5.6, various spectra of the near valence band region at different excitation energies are shown. The spectra are calibrated according to the gold reference and they are normalized to the In $4d_{5/2}$ peak intensity for a better comparison. With increasing photon energy, which is equivalent to an increasing information depth, a relative decrease of the Cd 4d signal compared to the In 4d signal is observed. In general, the height of the Cd 4d peak of the KF-PDT sample (black curve) exceeds that of the standard sample (red curve) but the difference decreases with increasing excitation energy. This is in accordance with the behavior shown in Figure 5.4. In addition, a distinct shift of the core levels and the valence band edges of the KF-PDT sample towards lower binding energies compared to the standard sample is visible.

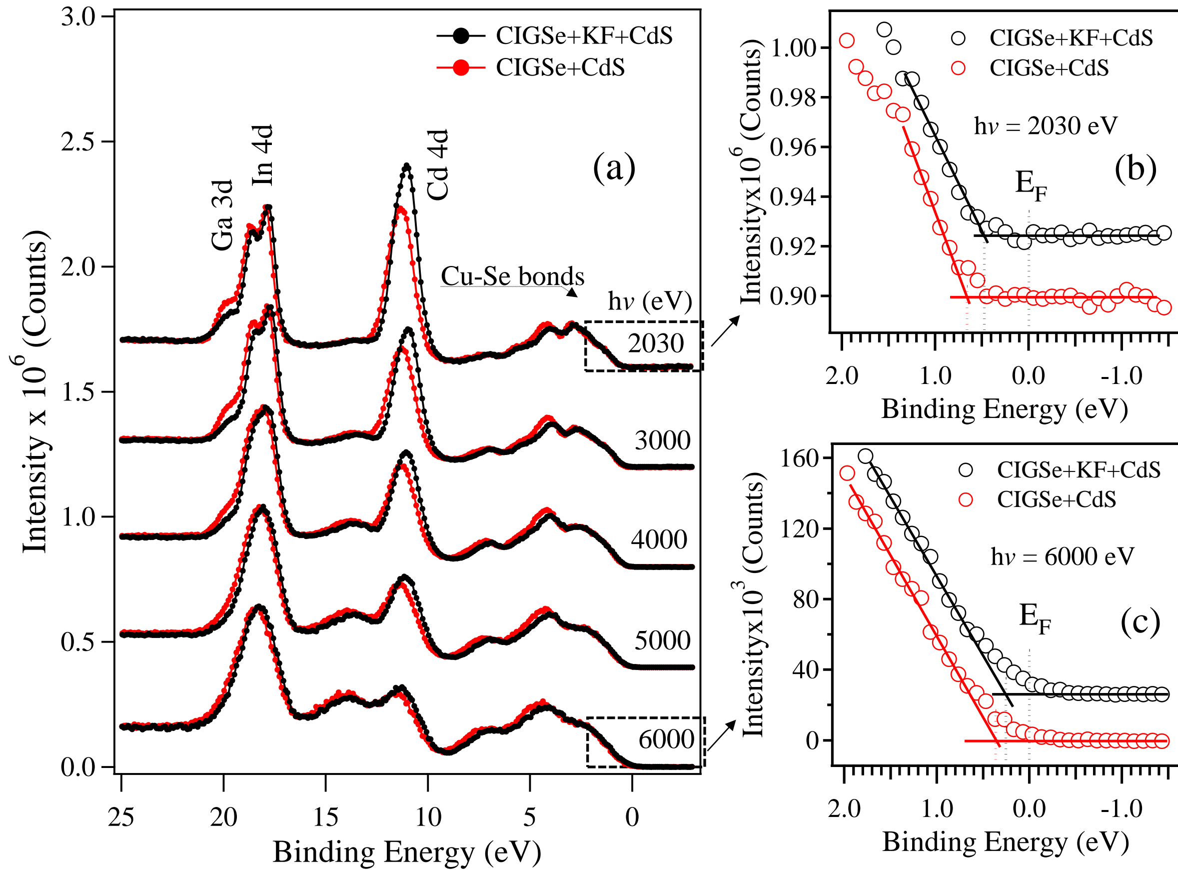

Figure 5.6: (a): XP spectra of the near valence band region of the standard CIGSe/CdS (red) and KF-PDT CIGSe/CdS (black) sample measured for various excitation energies. All spectra are normalized to the In $4d_{5/2}$ signal. (b)-(c): Onsets of the valence band data of CIGSe+KF+CdS and CIGSe+CdS samples measured with 2030 eV and 6000 eV excitation energies, as two examples to demonstrate how the E_{VBM}-E_F values are determined with linear extrapolations. The data of CIGSe+KF+CdS sample (black) are vertically shifted for a better visibility. The E_{VBM} values are visualized in Figure 5.7 (after Ümsür et al. [177]).

The resolution of HAXPES measurements in Figure 5.6-(a) is sufficient to assign the valence band maximum with respect to the Fermi level for different excitation energies. It was determined by linear extrapolation of the valence band onset with respect to the background level assuming a maximum error of ± 0.05 eV that strongly depends on the shape of the valence band edge. Two examples for the determination of the valence band maximum with respect to the Fermi level are given in Figure 5.6-(b) and (c) for the excitation energies of 2030 eV and 6000 eV, respectively. The depth-resolved valence band maximum values with respect to the Fermi level are shown in

Figure 5.7 with a schematic representation of the CIGSe/CdS heterocontact on the top of the graph that correlates with the detection depth using different excitation energies.

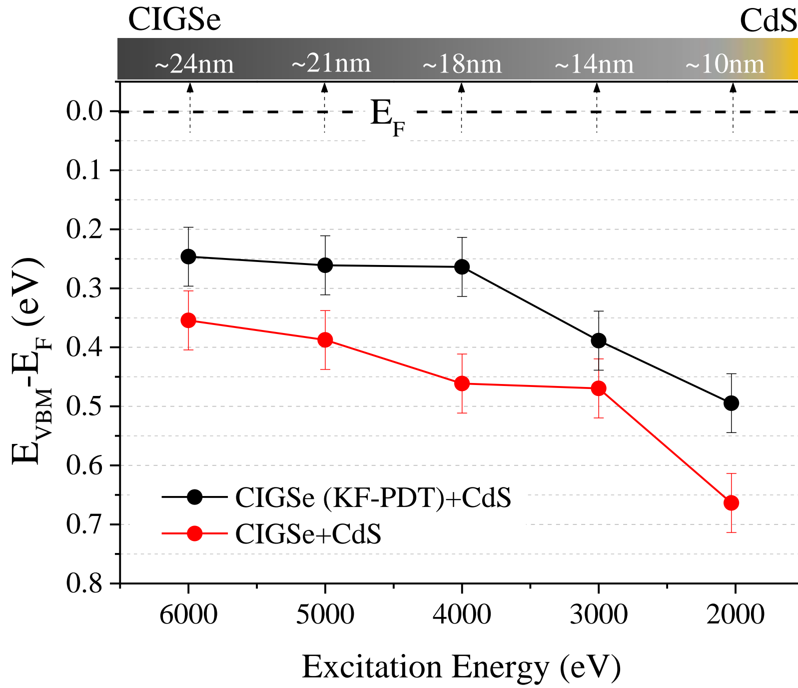

Figure 5.7: The position of the valence band maxima with respect to the Fermi level measured at different excitation energies providing depth dependent information with an estimated uncertainty of ± 0.05 (after Ümsür et al. [177]). Solid lines are guides for the eye only.

The dashed line in the graph represents the energetic position of the Fermi level. However, it is important to know that the measured valence band offset belongs to CIGSe although this material is covered by CdS. This is due to the fact that the band gap of CIGSe is much smaller than the band gap of CdS, thus hiding it. Furthermore, the amount of CdS is small compared to CIGSe, which leads to a weaker valence band signature. In general, the binding energy in the valence band region is low, resulting in a comparatively large kinetic energy of the considered photoelectrons originating from this region. This means that the information depth is even larger, which further explains the dominance of the CIGSe valence band in the spectra. As can be clearly seen in the graph, there is a distinct shift of the valence band maximum to lower values for the KF-PDT sample of about 0.15 eV. In addition, a pronounced band bending downwards in the near-surface region is observed on both samples with a shift of 0.3 eV between the first and the last data point at 2030 eV and 6000 eV, respectively.

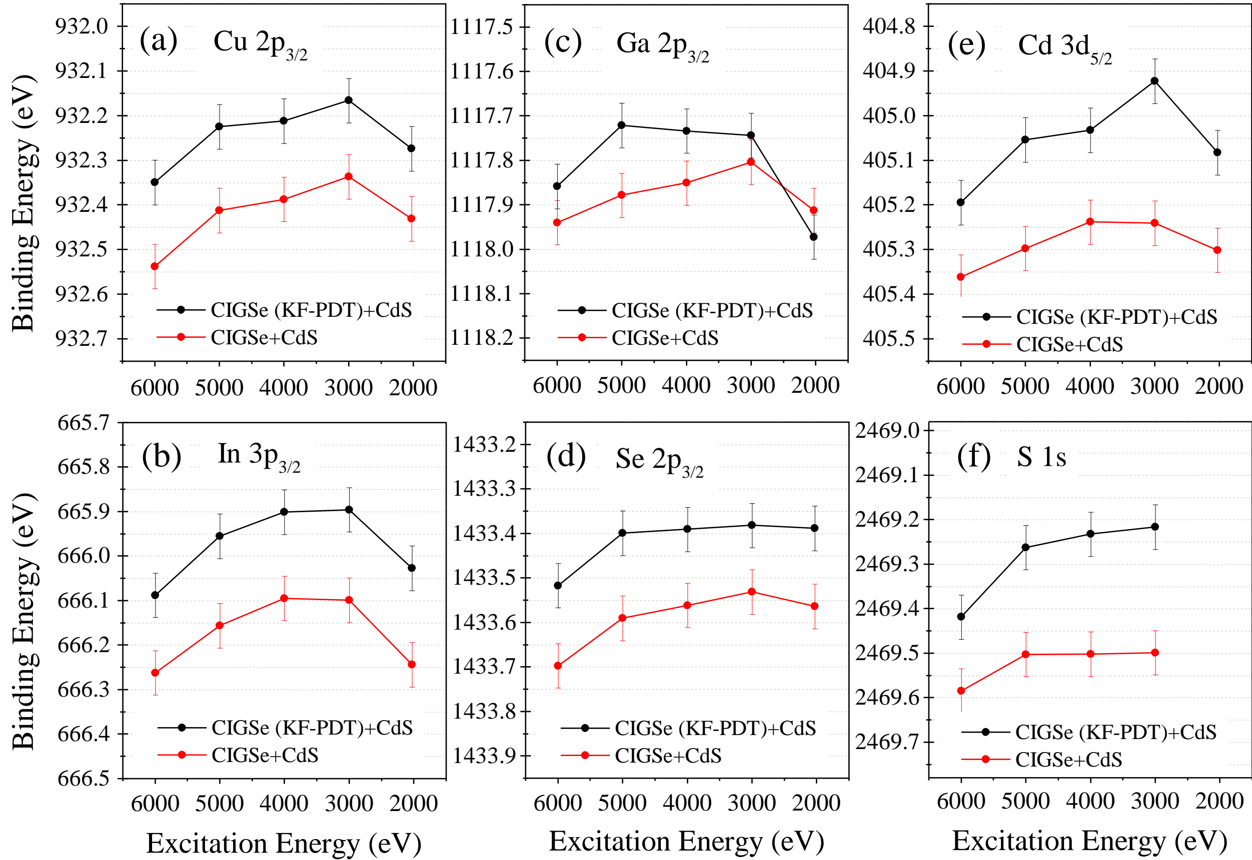

Figure 5.8: Binding energy positions of selected core level peaks as a function of excitation energy (a-f) (after Ümsür et al. [177]). Solid lines are guides for the eye only.

In Figure 5.8, a compilation of the binding energy positions of selected core level peaks is shown with respect to the excitation energy. All values are referred to the Fermi level; thus, the graphs can be directly compared to the valence band maximum shown in Figure 5.7. Except for the value of the Ga $2p_{3/2}$ peak in the near-surface region at 2030 eV, there is a more or less constant shift of about 0.2 eV of the KF treated CIGSe sample towards lower binding energies compared to the untreated sample. In contrast to the course of the valence band over the excitation energy, the binding energy values of the core levels show a bow-like behavior. The Cu, In, Ga, and Cd peaks initially follow the course of the valence band with increasing thickness towards higher binding energies, whereas the “anionic” species S and Se stay on a constant level. However, the first binding energy value of the S1s peak is unknown since the S1s transition is not accessible at 2030 eV. With increasing excitation energy, the core level peaks shift again to higher binding energies forming the above-mentioned bow. The fact that the valence band and the core levels are not shifting equally with excitation energy, cannot be explained by band bending. It is important to emphasize that the

shape of the curves (core level peaks and valence band maximum) and the constant shift between both samples are due to different effects.

Discussion of the experimental findings

- The fact that the measured valence band offset of the KF treated CIGSe/CdS sample is smaller compared to that of the untreated one (see Figure 5.7) first causes some irritations, since the opposite behavior is expected according to reference [38]. The deviation can only be explained by the presence of a thin CdS layer affecting the interface properties of the CIGSe/CdS contact. The valence band maximum of the untreated CIGS/CdS sample in the near interface region recorded at 2030 eV is 0.7 ± 0.05 eV (see Figure 5.7), which is in the range of previously reported values [151] for the same material system. This agreement gives a positive assessment of the reliability of the approach, including the measurement of the KF treated sample showing its valence band maximum at 0.55 ± 0.05 eV, which is roughly 0.15 eV above that of the untreated sample. Moreover, the observed behavior is independent of the excitation energy with a more or less constant offset of 0.15 eV, which follows the course of the valence band with increasing information depth. A similar shift is also observed for the core level peaks of all involved species except for gallium and sulphur in the near interface region. There is obviously a consistent shift of all the spectral features of the KF treated CIGSe sample to lower binding energies due to the incorporation of a negative charge into the interface region or due to the formation of an interfacial dipole (see Figure 5.9-(a)). For simplification, the binding energy positions of the core level peaks are represented as straight lines. Furthermore, in the near surface regime the binding energy of the Ga $2p_{3/2}$ peak is higher and that of the S 1s peak is lower than expected compared to the untreated sample (see Figure 5.8-(c) and (f)). This finding goes along with increased intensities for both species as can be seen in Figure 5.4 for an excitation of 2030 eV. Possibly, an additional, intermediate, and ultrathin Ga_xS_y phase was formed on the KF treated CIGSe sample during the deposition of CdS, which now affects the band alignment. In addition, the interface of the KF treated sample seems to be changed (see Figure 5.2) so that binding states of interlinked species forming the heterojunction become visible [179]. However, due to charge neutrality reasons it is difficult to explain that CdS related peaks also shift into the same direction on the KF treated sample. Hence, other reasons than the

formation of an interface dipole must be responsible for this shift, which is still related to electrostatic fields induced by additional charge.

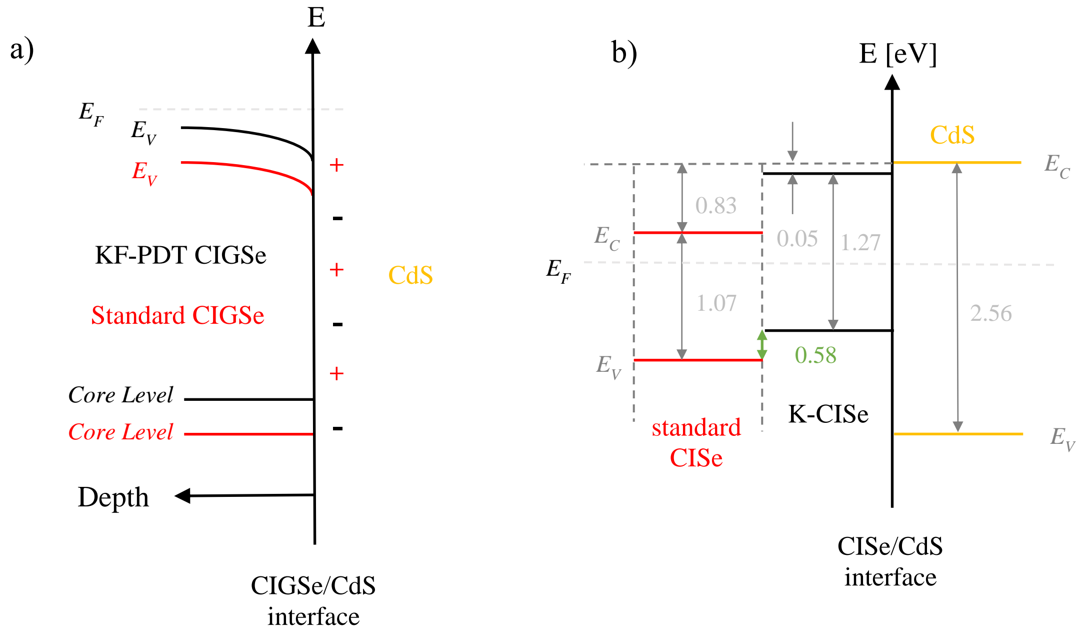

Figure 5.9: a) Scheme of the CIGSe/CdS interface showing the relative positions of the valence band and the core level peaks for the standard (red) and the KF-treated (black) CIGSe samples. b) Theoretical band alignment of Cu-poor CISe ($CuInSe_2$) and Cu-poor K containing CISe with respect to CdS according to [180].

In Figure 5.9-(b), a theoretical scheme of the band alignment of Cu-poor CISe (red) and Cu-poor K containing CISe (black) with respect to CdS is shown according to reference [180].

The calculation in Figure 5.9-(b) used hybrid DFT functionals (B3PW91, [181]) yielding good estimates for chalcopyrite band gaps. As basis, $Cu_5In_9Se_{16}$/CdS(110) and $K_2Cu_3In_9Se_{16}$/CdS(110) super cells are used to determine the band discontinuities of the Cu-poor CISe/CdS and K-CISe/CdS heterocontacts. By applying the transitivity rule [182], it turns out that the valence band maximum of the potassium containing, copper poor CISe absorber is located 0.58 above the standard CISe absorber in contact to CdS and this is what we see by trend in our measurements.

Although the theoretical work is only related to CISe and not to CIGSe, the obtained results demonstrate that it is possible to have a lower valence band maximum at the interface due to the incorporation of K. However, the increased amount of S causes a larger absorber band gap at the interface, pointing to a decreased conduction band discontinuity when considering the pure CIGSe

absorber in contact to the CdS buffer. Unfortunately, the conduction band is not accessible within the given experimental setup so that this phenomenon cannot be proven further.

- Another issue is the development of the CGI and GGI ratios on both samples with increasing thickness (see Figure 5.5). On the KF-treated CIGSe absorber, the overall concentration of Cu is smaller than on the non-treated absorber. Additionally, there is a gradient in the near-surface regime pointing to an enhanced Cu-depletion. In contrast to this, the standard CIGSe absorber is less Cu-poor and the CGI ratio shows a constant behavior over the whole thickness range within the error limit. So far it is assumed that the bare CIGSe surface is stronger Cu-depleted at the very-near surface than in the bulk, which might be attributed to the occurrence of an ordered defect compound (ODC) phase [29] or to the reconstruction of the topmost CIGSe layer [10]. Following the results of our measurements, this can be only confirmed for the KF treated sample. Possibly, this effect correlates with the GGI ratio, which shows an opposite behavior. While for the KF-treated absorber the GGI ratio is nearly constant (~0.32) over the complete energy range, it starts from a lower value for the standard sample, steadily increasing and ending up at ~0.4. The near-surface depletion of Cu appears on the KF-treated CIGSe absorber, whereas the Ga depletion appears in the near-surface region of the non KF-treated CIGSe absorber. In addition, the Cd concentration is much higher for the KF-treated sample compared to the non KF-treated sample. The fact that the CdS films were deposited on both KF-treated and the non-treated CIGSe absorbers under the same conditions (i.e. a simultaneous deposition), the higher Cd concentration for the KF-treated absorber implies that the Cd atoms diffuse much easier into the KF-treated CIGSe absorber. This goes along with an increased S concentration over the complete thickness range (see Figure 5.4), which could be explained by a stronger interdiffusion at the interface of the KF-treated CIGSe sample or a higher sulphur concentration in the CdS buffer layer at all. Indeed Lepetit et al. reported an enhanced sulfurization of the CIGSe surface during the CBD of CdS [94,183]. Besides this argumentation, it is also possible that the total amount of CdS is higher on the KF-treated sample because the growth conditions for CdS are apparently improved. Moreover, it seems that the KF-PDT has an additional impact on the heterocontact formation by changing the pristine CIGSe surface and its concentration ratios accordingly, e.g. by a higher Ga or S content in the near surface regime of the CIGSe absorber, which influences the band gap.

- In parallel, a strong Cu depletion at the surface should lead to a band gap widening by lowering the onset of the upper valence band due to the missing repulsing effect of the Cu 3d valence states [184]. This behavior can be directly observed in Figure 5.7 with a pronounced course of the valence band maximum over the excitation energy in both cases, the KF-treated as well as the non KF-treated CIGSe absorber, respectively. This band bending downwards is attributed to a decreasing Cu concentration towards the surface and not to the formation of a space charge region, which would go several 100 nm into the depth. Since the variation of the valence band maximum is strongest in the excitation energy range between 2000 to 4000 eV, it is assumed that the Cu depletion at the interface is limited to a thickness of 2-5 nm only. In this thickness regime, the change of the onset of the upper valence band is most pronounced.

- In addition to the enhanced Cu depletion on the KF treated CIGSe sample, which was reported earlier [8] and which was also found in this work as shown in Figure 5.4 and Figure 5.5, an enrichment of Cd is observed in the interface region. This is ascribed to the fact that Cd diffuses into the CIGSe absorber and occupies the Cu vacancies as published before [62]. This finding is also supported by the deviation of the concentration levels of these two species, which are of the same order of magnitude in both samples (see Figure 5.4). In other words, the lack of Cu in the KF treated sample is almost fully compensated by the presence of Cd. But what is the impact of the surplus of Cd atoms in CIGSe? It is assumed that the optimum CIGSe absorber surface for highly efficient solar cells is Cu-poor and already inverted, thus changing from p-type conduction in the bulk to n-type conduction at the surface [120]. Therefore, additional Cd, which acts as donor in CIGSe [185] can release further electrons into the conduction band as free charge carriers. These electrons then migrate as majority carriers along the conduction band towards the interface. If now the conduction band discontinuity between the CIGSe absorber and the CdS buffer layer as a barrier is not too large, they are able to overcome this barrier and accumulate at the CdS surface as negative charges. The amount of this charge is directly correlated to the Cd concentration in the CIGSe absorber. The given explanation reflects exactly, what has been measured. In addition, it is concluded that the barrier in the conduction band at the heterocontact is small enough; otherwise the accumulation would take place in the interface region. With an extrapolated value of the valence band discontinuity between CIGSe and CdS of about 0.9 eV [59,186], a valence band offset of 0.5 eV at the KF treated CIGSe surface as measured and shown in Figure 5.7, and a band gap of the CdS buffer layer of 2.5 eV [187], a

widening of the CIGSe band gap up to a value of 1.6 eV at the interface due to the incorporation of S and Ga leads to a negligible conduction band discontinuity. A smaller value than 1.6 eV, as well as a larger one would imply either a band bending downwards or upwards on the chalcopyrite side of the junction, which for a fixed conduction band position of the CdS layer with respect to the Fermi level would lead in both cases to a potential barrier affecting the electron transfer through the interface. However, further simulations are necessary to consolidate this assumption, but the experimental data strongly point into this direction.

- Besides the ongoing discussion, there is another aspect, which is worth to be mentioned, and this is the morphology of the CdS layer. In contrast to the KF treated CIGSe sample, there are small precipitations visible on the standard sample (Figure 5.2) directing to a slightly different growth mechanism when applying the CBD and, which hints to a less ordered interface or to an increased lattice misfit. The lattice parameter of CIGSe (a = 0.56 - 0.58 nm depending on the Ga content); is in the range of that of CdS (a = 0.58 nm) [188]. This means that stress induced defect formation in the initial growth of the CdS due to lattice mismatch is unlikely. Obviously, the standard CIGSe absorber has more surface defects, which are acting as nucleation centers during the subsequent CdS deposition forming additional precipitations. Further investigations concerning this aspect are necessary.

5.2 Surface Properties of CIGSe and CIGSe+KF Absorbers and the Influence of Ammonia Etching during the CBD Process

As it was mentioned in the previous section, the smaller valence band offset of the KF treated CIGSe/CdS sample compared to that of the untreated one exhibits the opposite behavior than was expected according to reference [38]. The deviation was explained by the presence of the thin CdS layer affecting the interface properties of the CIGSe/CdS contact. In order to check the validity of this explanation, the standard and KF treated bare CIGSe samples without thin CdS layers are measured with XPS and UPS under laboratory conditions, i.e. using the Al Kα (Mg Kα) and He I excitation sources, respectively. The results are shown in the following.

The surface properties of bare CIGSe and CIGSe+KF and the effect of the usage of an NH_3-containing solution in the chemical bath for CdS deposition are studied in this section. Details on the samples under investigation (i.e. sample #5 to sample #8) can be found in Table 3.1.

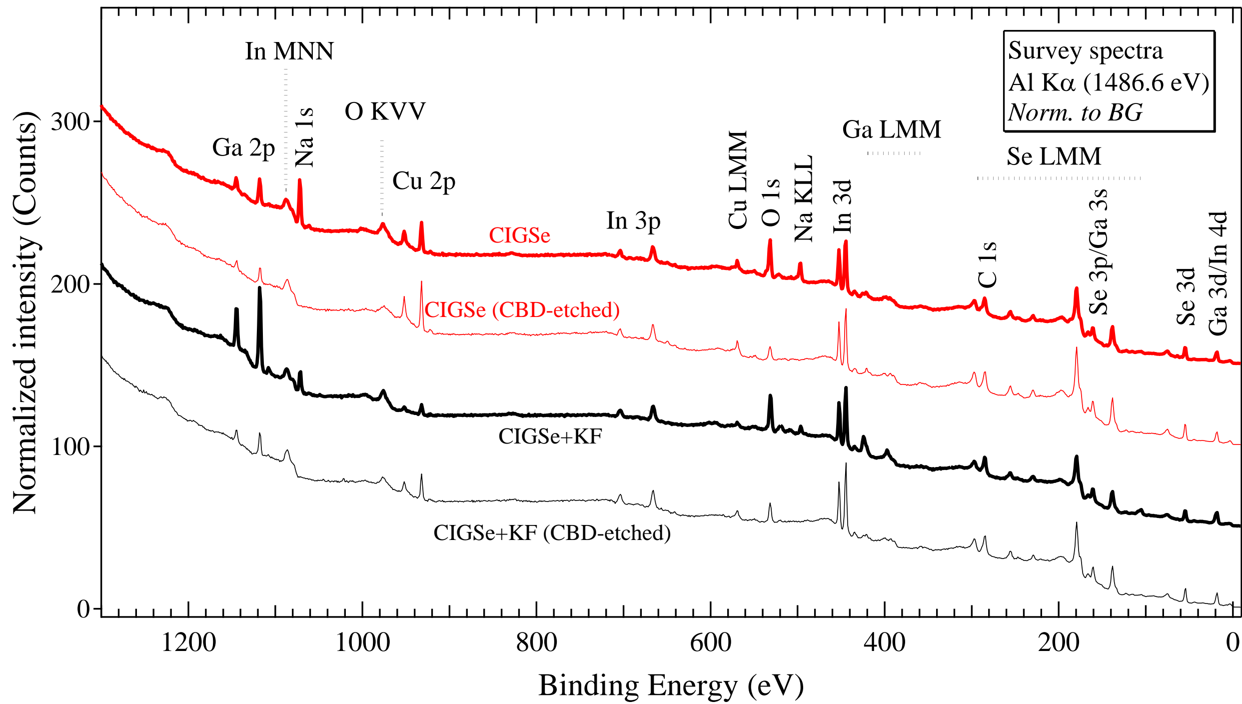

Figure 5.10 XP survey spectra of the standard CIGSe (red) and KF-PDT CIGSe (black) samples, before and after the etching process in NH_3-based aqueous solution.

The survey spectra of the uncovered CIGSe samples with and without KF-treatment, before and after CBD-etching are shown in Figure 5.10 for Al Kα excitation source in the binding energy range from 0 to 1300 eV. It can be seen that the survey spectra contain the characteristic core level and the Auger peaks of the CIGSe material. Moreover, significant quantities of carbon and oxygen are present on both samples, with the oxygen being partially removed by the CBD-etching. One reason for the relatively high carbon and oxygen contamination is the usage of the aqueous solution for the CBD etching. Another reason can be the storage environment and the storage time for the samples that were packed in a plexiglass box after the previous HAXPES measurements, although they were stored under N_2-atmosphere in a glovebox. Comparing the survey spectra to the one shown in Figure 5.1, one can see that the intensity of the carbon and oxygen peaks compared to the main peaks are higher. The reason for that is the usage of the Al Kα excitation source, which results in a more surface sensitive measurement than the one with 6000 eV excitation energy. Additionally, the sodium related signal Na 1s can be seen for both samples at the binding energy of 1071 eV,

which implies a sodium diffusion from the SLG to the CIGSe surface probably because of the air exposure of the samples. Apparently, the sodium on the surface is completely removed by the CBD etching. The potassium related core level signal K 2p on the KF treated sample cannot be seen in the survey spectra, because it overlaps with the Se LMM Auger peak at around 239 eV binding energy when measuring with this specific excitation energy (Al Kα).

In order to check the effect of the KF treatment of the CIGSe absorber on the valence band maximum, the UPS measurements of the valence band edges for both standard and KF-PDT CIGSe samples are shown in Figure 5.11 at 21.2 eV excitation energy (He I).

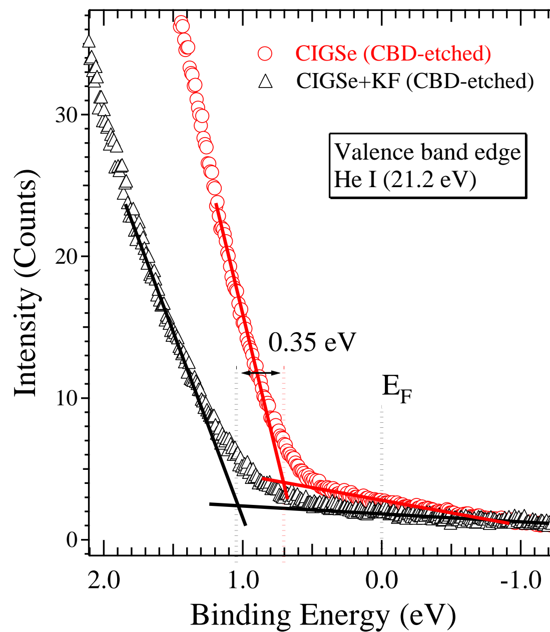

Figure 5.11 Valence band edges of the $Cu(In,Ga)Se_2$ samples with (black) and without (red) KF-PDT after the etching process in the NH_3-based aqueous solution, measured with He I source.

The graph in Figure 5.11 represents the relative energetic distance of the valence band maxima of the CBD-etched samples. It makes no sense to show the UPS of the non-etched samples here, since the UPS is very surface sensitive and does not give useful results on oxidized samples. The CBD-etched samples here are in the state, where the effect of the CdS overlayer is eliminated. It can be clearly seen that the KF-PDT causes a significant shift of 0.35 eV in the valence band maximum to higher binding energies with respect to the one of the untreated sample. This is a similar amount and the same direction (i.e. higher binding energy side) of the shift of the valence band edge within

the uncertainty due to KF-PDT, which was found in reference [38]. This finding proves the validity of the fact that the presence of the CdS overlayer strongly affects the interface properties of the CIGSe/CdS contact, so that the valence band maximum of the KF-treated sample appears at a lower binding energy than that of the untreated one with 0.15 eV (see Figure 5.7).

In order to understand possible reasons for the corresponding shift in VBM of the KF-PDT sample, one should additionally consider the XPS core level measurements. For a detailed analysis of the XP spectra of the CIGSe samples with and without KF-PDT, the O 1s, C 1s, Cu $2p_{3/2}$, Cu LMM, In $3d_{5/2}$, In MNN, Ga $2p_{3/2}$, Ga LMM and Se 3d core level and Auger peaks were measured with higher resolution. In Figure 5.12, the respective spectra are shown for the as-grown samples and after the dedicated CBD-etching process, all taken at 1486.6 eV (Al Kα) excitation energy, except C 1s, which is taken at 1253.6 eV (Mg Kα) to separate the K 2p core level and the Se LMM Auger peak from each other. All spectra were corrected with respect to their binding energy using the position of the Au $4f_{7/2}$ peak at 84.0 eV. For a better comparability, all peaks were normalized to the background (Norm. to BG). The core levels are given in binding energy, whereas the Auger peaks are given in kinetic energy by convention.

- Figure 5.12-(a) shows that both KF treated and non-treated samples are highly oxidized with the first one being more pronounced, probably because of the hydroscopic nature of the potassium species. The CBD-etching process has apparently a beneficial effect on both samples by partially removing H_2O and OH^- related compounds from the surface. Additionally, as the Figure 5.12-(b) implies, the ammonium-containing bath etches away some hydrocarbons, which appear at a binding energy of around 290 eV. In both figures (a) and (b), the intensity of O 1s and C 1s peaks of the KF treated sample remain slightly higher than that of non-treated samples after the etching process, which is strongly related to the oxidation degree and the corresponding etching time. In addition to the carbon signal, Figure 5.12-(b) shows that the K 2p doublet is measurable with the Mg Kα source only on the KF treated sample. The NH_3-based solution completely removes the potassium from the surface, although different results are found in reference [170], where they show with XPS a remnant of almost half of the potassium after the ammonium etching.

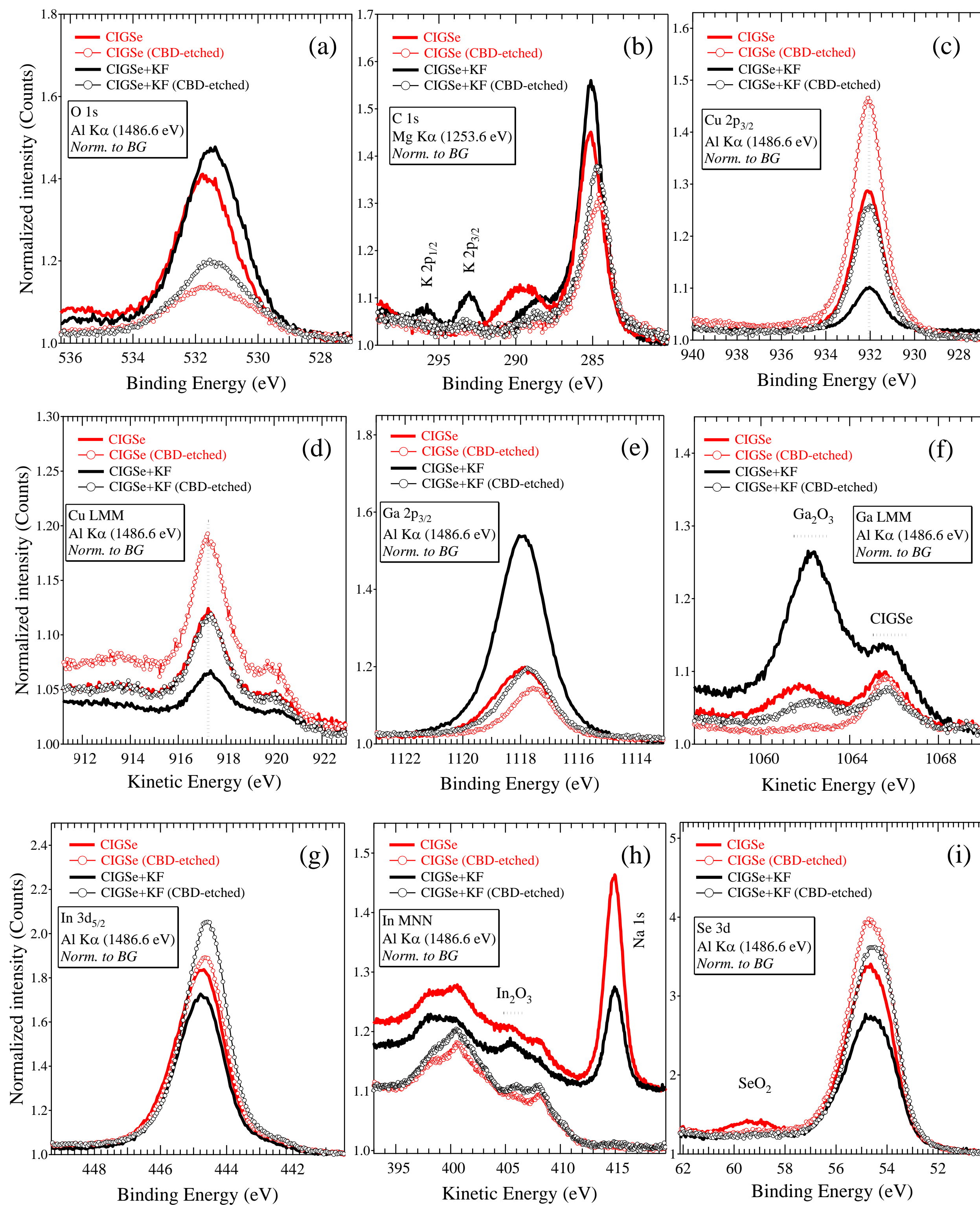

Figure 5.12 XP spectra of the (a) O 1s, (b) C 1s, (c) Cu $2p_{3/2}$, (d) Cu LMM, (e) In $3d_{5/2}$, (f) In MNN, (g) Ga $2p_{3/2}$, (h) Ga LMM and (i) Se 3d photoemission signals of the CIGSe and CIGSe+KF-PDT samples before and after CBD-etching process. The measurements are performed at the CISSY setup using Al Kα and Mg Kα excitation sources.

- In Figure 5.12-(c), the Cu $2p_{3/2}$ core level peaks are shown at a binding energy of 932 eV. The strong Cu depletion due to KF-PDT can be clearly seen as it was previously reported [8,38,170,176] and similarly measured within the HIKE experiments in the previous section. The unchanged core level position together with the Cu LMM Auger peak (see Figure 5.12-(d)) after the CBD etching, results in a constant modified Auger parameter of α'=BE (Cu $2p_{3/2}$) + KE (Cu LMM) = 1850.80 eV. It is an indication that both the KF-PDT and CBD-etching do not change the chemical environment of the Cu species. The increase in the signal intensity of both samples after the CBD-etching is due to the removal of the contaminant over-layer in the chemical bath.

- The Ga concentration of the KF-treated sample is measured much higher than that of the standard sample as it can be seen from the Ga $2p_{3/2}$ peak in Figure 5.12-(e). However, the opposite behaviour was expected according to references [8,170] and the other measurements in this chapter. It becomes clear by considering the Ga LMM Auger peak in Figure 5.12-(f) that Ga species on both samples are highly oxidized and form Ga_2O_3 compounds. The oxidation of Ga occurs more prominently in case of the KF-treated sample due to the higher adsorption of oxygen species because of the air exposure of the CIGSe samples with and without KF-PDT. The formation of the Ga_2O_3 compound causes an overlapping of two Ga $2p_{3/2}$ contributions in Figure 5.12-(e), i.e. Ga $2p_{3/2}$ (of Ga_2O_3) and Ga $2p_{3/2}$ (of CIGSe) and creates the significant difference in peak intensities. As it can be clearly seen in the Ga LMM Auger peak, the huge oxide overlayer of Ga_2O_3 is partially removed by CBD-etching in case of KF-treated sample, whereas it is completely etched away in case of the standard sample. It is obviously a matter of the total amount of oxidized species and the etching time, which was kept constant for both samples. The remaining Ga_2O_3 contribution to the Ga $2p_{3/2}$ peak in Figure 5.12-(e) even after the CBD-etching, makes the signal intensity at the KF-treated sample still higher. When discussing the Ga excess in the near surface region of the KF-treated sample, shown in Figure 5.4, it was mentioned that the Ga excess was attributed to specific interface reactions during the CIGSe/CdS heterojunction formation. Together with the unexpected shift of Ga $2p_{3/2}$ in the near surface of the KF-treated sample, shown in Figure 5.8-(c), and with the tendency of an increased concentration of sulphur towards the surface region, shown in Figure 5.4, it was concluded that possibly an intermediate ultrathin Ga_xS_y phase was formed on the KF-treated sample during the CdS deposition. While the above conclusion still remains valid, the observed unexpected results

related to Ga species can be due to the formation of Ga_2O_3 in addition to Ga_xS_y. That means, the above mentioned intermediate layer consists of probably not only Ga_xS_y but a mixture of it with Ga_xO_y. The fact that the oxidation of Ga species was observed to be increased in CIGSe with KF-PDT and the NH_3-containing CBD bath could only partially remove the Ga oxides, suggests that the time between the CIGSe growth and the CdS deposition by CBD should be kept as short as possible, especially when KF was applied on the CIGSe.

- It was previously shown in Figure 5.4 that the In concentration at the CIGSe/CdS interface is not strongly affected by the KF-treatment. Although the samples here have no CdS over layer, they present more or less the same properties. In $3d_{5/2}$ core level peaks of the treated and non-treated CIGSe samples are shown in Figure 5.12-(g). Its signal intensity for the KF-treated sample appears to be slightly smaller than for the non-treated sample. It can be attributed to the attenuation effect of the ultrathin Ga_2O_3 overlayer that is especially formed on the KF-treated sample. Since the Ga_2O_3 overlayer was etched away by the CBD solution, the In $3d_{5/2}$ signal intensity becomes almost 1.2 times higher for the KF-treated sample, whereas it increases only by a factor of 1.03 for the non-treated sample. When comparing the signal intensities of the core level, one should consider also the formation of In-related oxide compounds. Figure 5.12-(h) shows the In MNN Auger peaks of both samples. It can be seen that aside from Ga, In species are also oxidized and similarly form In_2O_3 compounds. A stronger In_2O_3 formation can be observed at the KF-treated sample because of the same reasons as discussed for Ga. On closer inspection, one can see that the In_2O_3 compounds are not etched away completely or as strongly as Ga_2O_3 by the CBD solution [85], thus still affecting the signal intensity of In $3d_{5/2}$ core level.

- In Figure 5.12-(h), the sodium related core level peak Na 1s appears at a kinetic energy of about 415 eV, which is measured with Al Kα excitation source. Interestingly, the intensity of the Na 1s peak of the non-treated sample is found to be much higher than that of the treated one. This is probably correlated to the presence of potassium on the treated sample. It implies that the presence of potassium on the sample somehow limits the amount of sodium diffusion from the soda lime glass. In other words, the addition of KF on the CIGSe removes Na from the surface towards the back of the sample as it was proposed in references [8,170] with an ion exchange mechanism. In order to check if there is a direct relation between the total concentration of the alkaline metals available on the surface, the concentrations of sodium and potassium are calculated using the integrated area of the core level peaks Na 1s and K $2p_{3/2}$, respectively. The

calculation is performed taking the correction factors into account. A relative concentration ratio of total alkaline metals ([Na]+[K]) $_{\text{KF-treated}}$ / ([Na]) $_{\text{non-treated}}$ ≈ 0.5 was obtained. This indicates that the potassium species occupy only half of the free sites, which are left behind by the Na removal due to KF-PDT, and the remaining half of the sites remains unoccupied and free for other diffusion partners. Obviously, both alkaline related peaks Na 1s and K 2p have completely disappeared due to the CBD etching.

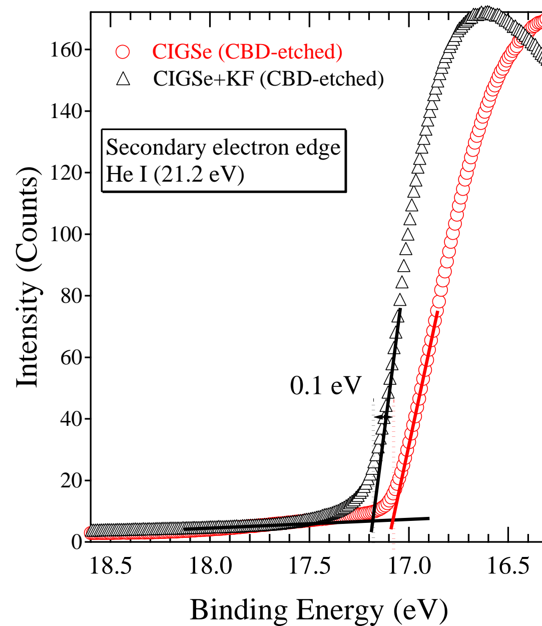

Figure 5.13 (a) Secondary electron edges of the standard CIGSe (red) and KF-PDT CIGSe (black) bare samples after the etching process in the NH_3-based aqueous solution, measured with a He I source. (b) Schematic energy diagram showing the shifts in valence band maximum and the work function of the CIGSe surface due to the incorporation of KF-PDT.

- Besides the formation of In and Ga oxides, Se species are slightly oxidized only on the CIGSe sample without KF-PDT, forming SeO_x compounds as shown in Figure 5.12-(i) and they are completely removed by CBD-etching (details on the CBD-etching process can be found in Section 3.1.2). The attenuation effect of the Ga oxide overlayer can be observed also on the Se 3d signal intensity. The maximum of the Se 3d signal increases by a factor of 1.33 due to CBD-etching in case of KF-treated sample, whereas it becomes only 1.18 times higher in case of the standard sample. The removal of the Ga and In oxide layers result in a higher increase of the Se 3d signal of the KF-treated sample.

- The fact that the Cu $2p_{3/2}$ core level has the same binding energy for both samples and the small shifts in the other core levels are attributed to chemical changes implies that the distinct shift of 0.35 eV in the valence band maximum can be ascribed to a band gap widening due to the KF-PDT by inducing a strong Cu-depletion as reported in [38,176]. In addition to the band gap widening, KF-PDT induces a slight shift of 0.1 eV at the secondary electron edge towards higher binding energies, as shown in Figure 5.13. This implies a reduction of the work function of 0.1 eV due to KF-PDT. Indeed, it was proposed by Reinhard et al. that the incorporation of K could reduce the surface work function of CIGSe [189].

5.3 Summary

In this chapter, the impact of the KF-PDT on CIGSe/CdS interface is investigated by means of depth resolved hard x-ray photoemission spectroscopy in the near surface region. Two CIGSe absorbers are used with one being treated by potassium fluoride prior to the chemical bath deposition of an ultrathin CdS layer while the other was not. During this study, all parameters are tried to be kept the same except the KF-PDT in order to carve out the impact of this treatment.

It turns out that besides strong chemical changes in the CIGSe/CdS interface region, namely a Cu depletion that goes along with a Cd accumulation, the electronic properties of the heterocontact are significantly affected and influenced by the KF-PDT. This is attributed to an enhanced doping effect, which is induced by additional Cd in the near surface region and, which releases free electrons into the conduction band of the CIGSe absorber. These electrons are able to follow the band downwards to the surface where they accumulate. It is assumed that this process starts already during the deposition of CdS and that excessive electrons are able to overcome the potential barrier formed at the CIGSe/CdS interface. By this effect, the band alignment of the CIGSe/CdS heterojunction is obviously improved; leading to better efficiencies of the CIGSe based thin film solar cell devices.

It is found that the CIGSe/CdS interface is strongly intermixed and that the variation of the valence band in the very near surface region of CIGSe of both samples is basically of chemical nature and not only due to band bending. However, a significant increase of the sulfur concentration is observed on the KF treated CIGSe/CdS compared to the untreated CIGSe/CdS sample. It is assumed that this phenomenon leads to a band gap widening, which mainly affects the position of

the conduction band in such a way that the height of the barrier at the conduction band within the interface is reduced. However, since the conduction band cannot be probed with XPS, this prediction remains speculative and needs further experimental proof.

6 Summary

The goal of this thesis was to gain a deeper insight into the interface properties between $Cu(In,Ga)Se_2$ (CIGSe) absorber and CdS buffer layers, which are the main components of the state of the art high efficiency CIGSe-based thin film solar cells. Firstly, the interface formation between the CIGSe and the CdS is analyzed with respect to the Cu concentration of the CIGSe by focusing especially on the Cd diffusion from the buffer into the absorber side. Secondly, the chemical and electronic impact of the KF post-deposition treatment (KF-PDT) on the interface properties of the CIGSe/CdS material system is analyzed in detail. In the following, the most important results and conclusions are summarized.

DFT calculations by project partners in the Max-Planck-Institute for Chemical Physics of Solids have shown in the first part of the Chapter 4 that there is a clear qualitative difference between the Cd diffusion in the Cu-poor CIGSe compared to that of the Cu-rich compounds. Cd diffusion in Cu-poor samples is a two-step process, where Cu atoms are actively exchanged by Cd impurities during the diffusion process. In case of Cu-rich samples, the Cu atoms are not directly involved in the diffusion process but they indirectly play a role as Cu vacancy defects, where Cd impurities are being incorporated.

In addition to the qualitative differences, DFT calculations revealed quantitative differences in the two diffusion mechanisms in terms of the activation energies (E_A) for the Cd diffusion in Cu-poor and Cu-rich compounds. In the Cu-rich CIGSe, an activation energy of ~2.1 eV was calculated for the transfer of Cd from Cd_{Cu} substitutional sites to the Cd_i interstitial positions. Since the Cd diffusion after this step occurs relatively easy with an E_A of 0.2 eV, the rate limiting E_A in Cu-rich CIGSe compounds was found to be on the order of 2.1 eV. In case of Cu-poor compounds, the diffusion of Cd is controlled by the displacement of the Cu atoms into the pristine Cu vacancies.

The activation energy for this process was calculated to be ~0.9 eV. The E_A for the Cd diffusion into the newly created Cu vacancy, which was left behind after the Cu diffusion, was found to be approximately 0.7 eV. Therefore, the rate limiting E_A in Cu-poor compound appears to be on the order of 0.9 eV, which is half of that of the former process with an E_A of 2.1 eV. Hence, theoretical calculations suggested that the diffusion of Cd takes place considerably easier in the Cu-poor phases compared to the Cu-rich compounds.

The experimental proof of the theoretical calculations on the Cd diffusion was performed using hard x-ray photoelectron spectroscopy (HAXPES). For this study, Cu-poor and Cu-rich CIGSe samples with Cu/In+Ga ratios of 0.80 and 0.95, respectively, are covered with a thin film of CdS in the same chemical bath. The Cu-poor and Cu-rich CIGSe/CdS heterostructures were measured with an excitation energy of 3000 eV at room temperature as well as up to elevated temperatures of 400 °C. By having the lower activation energy for Cd diffusion in the Cu-poor compound, no trace of Cd was detected at the near surface region after the final annealing temperature of 400 °C. On the other hand, small amounts of Cd could be still measured within the same depth of the Cu-rich sample after an identical annealing process.

HAXPES measurements have shown that Cu atoms are directly involved in the diffusion process of Cd in the Cu-poor compound. While the Cd concentration during the annealing process was steadily decreasing, the relative Cu concentration in the near surface region was found to be increasing up to 320 °C, where Cu and Cd atoms are actively exchanged. At elevated temperatures between 320 °C and 400 °C, it was measured that the Cd signal from the Cu-poor CIGSe surface decreased first rapidly and completely vanished at the end of the annealing period; whereas at the same time, a significant Ga diffusion towards the CIGSe/CdS heterostructure surface was observed, where they occupy V_{Cu} sites, which were first occupied by Cd impurities.

The exchange process of S-Se atoms at the interface of the Cu-poor CIGSe/CdS heterostructure and the variation in the binding energy positions of the core levels pointed to the formation of a $GaS_{1-x}Se_x$-like compound at the interface. A highly-intermixed interface of the Cu-poor CIGSe/CdS heterostructure having a high concentration of Ga due to elevated temperatures is concluded to be one of the reasons for the degradation of the conversion efficiencies at elevated temperatures because of the formation of a high conduction band offset.

The impact of the KF post-deposition treatment on the chemical and electronic properties of the CIGSe/CdS interface was analyzed by means of depth-resolved HAXPES. For this purpose, two similar CIGSe absorbers were prepared with one being treated by KF prior to the deposition of an ultrathin CdS film while the other was not. HAXPES studies in the near surface region have shown that besides a strong Cu depletion and accordingly a Cd accumulation in the CIGSe/CdS interface region, the electronic properties of the heterocontact are considerably influenced by the KF-PDT. It was argued that additional Cd atoms in the near surface region release free electrons into the conduction band of the inverted CIGSe absorber. These electrons accumulate at the surface by following the downwards shape of the conduction band. By this effect, the band alignment at the CIGSe/CdS heterojunction is improved, leading to better efficiencies of the CIGSe-based thin film solar cells.

Depth-resolved HAXPES measurements have revealed that the CIGSe/CdS interface is strongly intermixed. Therefore, the downwards bending of the valence bands of the treated and the non-treated absorbers is attributed to not only the band bending but also to chemical variations at the interface. Additionally, a significant increase in the sulfur concentration was observed on the KF treated sample compared to the untreated sample. It was assumed that the better sulfurization of the CIGSe surface during the deposition of the CdS due to the KF-PDT leads to a distinct band gap widening, which mainly affects the position of the conduction band minimum. This would reduce the height of the barrier at the CIGSe/CdS interface, being a reason for the improvement of the conversion efficiencies due to KF-PDT, however this assumption remains speculative and needs further experimental proof, since the conduction band cannot be probed with XPS. Other experimental methods, such as x-ray absorption spectroscopy or inverse photoelectron spectroscopy can be used to probe directly the conduction band and to prove the above-mentioned assumption.

7 Appendices

7.1 Nomenclature of the Photoelectrons

In the spectroscopic notation of photoelectrons, the state of electrons is labeled with (1) the principle quantum number n = 1, 2, 3, 4..., (2) the angular momentum l = 0, 1, 2, 3... (correspondingly s, p, d, f...) and (3) the total angular momentum $j = l + s$, where s is the spin quantum number of electron and takes values $s = \pm 1/2$. As an example, the notation of Cu $2p_{3/2}$ describes the copper electrons with quantum numbers $n = 2$, $l = 1$ and $j = 3/2$ (i.e. $s = +1/2$).

Table 7.1 Some examples of x-ray notation and their counterpart in spectroscopic notation.

X-ray notation	Spectroscopic notation	X-ray notation	Spectroscopic notation
K	1 s	M_5	3 $d_{5/2}$
L_1	2 s	N_1	4 s
L_2	2 $p_{1/2}$	N_2	4 $p_{1/2}$
L_3	2 $p_{3/2}$	N_3	4 $p_{3/2}$
M_1	3 s	N_4	4 $d_{3/2}$
M_2	3 $p_{1/2}$	N_5	4 $d_{5/2}$
M_3	3 $p_{3/2}$	N_6	4 $f_{5/2}$
M_4	3 $d_{3/2}$	N_7	4 $f_{7/2}$

In the x-ray notation of Auger lines, the principle quantum number n = 1, 2, 3, 4... is expressed by capital letters K, L, M, N... It is followed by suffixes 1, 2, 3, 4..., which represent the various contributions of increasing l and j, i.e. $l = 0$ and $j = 1/2 \rightarrow 1$, $l = 1$ and $j = 1/2 \rightarrow 2$, l=1 and $j = 3/2 \rightarrow 3$.

Some examples of this notation and their counterpart in spectroscopic notation are listed in Table 7.1. The combination of the three energy levels involved in the Auger process is used to label Auger electrons. An example of an Auger peak In MNN can be seen in the XPS survey spectrum in Figure 3.4. The peak in there has two contributions of overlapped peaks, namely In $M_5N_{4,5}N_{4,5}$ and In $M_4N_{4,5}N_{4,5}$ with kinetic energies of about 401 eV and 408 eV, respectively. If the first one is considered, M_5 indicates that the photoelectron is ejected from the In $3d_{5/2}$ level and filled up by an electron of In $4d_{3/2}$ or In $4d_{5/2}$ (N_4 or N_5). And the Auger electron is ejected from the same level N_4 or N_5. The doublet separation of In $3d_{5/2}$-$3d_{3/2}$ (M_4-M_5) with about 8 eV is directly reflected in the difference in the kinetic energy of Auger electrons, since this is exactly the same difference in the energy of secondary x-rays ($h\nu'$).

7.2 Reference Data for XPS

Table 7.2 Reference data for some selected core levels adopted from the NIST database [98].

Core Level	Compound	Binding Energy	Reference
S $2p_{3/2}$	CdS	161.00	[190]
S $2p_{3/2}$	CdS	161.40	[191]
S $2p_{3/2}$	CdS	161.60	[192]
S $2p_{3/2}$	CdS	161.70	[192]
S $2p_{3/2}$	CdS	161.70	[193]
S $2p_{3/2}$	CdS	161.80	[192]
S $2p_{3/2}$	CdS	161.80	[191]
S $2p_{3/2}$	CdS	161.80	[194]
S $2p_{3/2}$	CdS	162.16	[195]
S $2p_{3/2}$	CdS	162.20	[196]
S $2p_{3/2}$	$CdIn_2S_2Se_2$	161.90	[159]
S $2p_{3/2}$	$CdS_{0.62}Se_{0.38}$	161.30	[197]
S $2p_{3/2}$	$CuGaS_2$	161.90	[198]
S $2p_{3/2}$	$CuInS_2$	161.80	[158]
S $2p_{3/2}$	CuInSSe	162.00	[158]
S $2p_{3/2}$	In_2S_3	161.20	[193]
S $2p_{3/2}$	In_2S_3	161.85	[199]
S $2p_{3/2}$	Ga_2S_3	162.20	[200]
Cd $3d_{5/2}$	CdS	405.10	[192]
Cd $3d_{5/2}$	CdS	405.20	[191]
Cd $3d_{5/2}$	CdS	405.30	[201]
Cd $3d_{5/2}$	CdS	405.30	[192]
Cd $3d_{5/2}$	CdS	405.40	[194]
Cd $3d_{5/2}$	CdS	405.40	[191]
Cd $3d_{5/2}$	CdS	405.40	[202]

Cd $3d_{5/2}$	CdS	405.50	[192]
Cd $3d_{5/2}$	CdS	405.73	[195]
Cd $3d_{5/2}$	$CdSe$	405.00	[203]
Cd $3d_{5/2}$	$CdSe$	405.20	[204]
Cd $3d_{5/2}$	$CdSe$	405.30	[201]
Cd $3d_{5/2}$	$CdIn_2S_2Se_2$	405.80	[159]
Ga $2p_{3/2}$	Ga_2O_3	1116.90	[205]
Ga $2p_{3/2}$	Ga_2O_3	1117.50	[206]
Ga $2p_{3/2}$	Ga_2O_3	1117.80	[99]
Ga $2p_{3/2}$	Ga_2O_3	1119.00	[207]
Ga $2p_{3/2}$	$GaSe$	1117.60	[208]
Ga $2p_{3/2}$	Ga_2Se_3	1118.00	[57]
Ga $2p_{3/2}$	$CuGa_5Se_8$	1118.10	[57]
In $3d_{5/2}$	$CuInSe_2$	444.10	[209]
In $3d_{5/2}$	$CuInSe_2$	444.70	[210]
In $3d_{5/2}$	$CuInSe_2$	444.80	[158]
In $3d_{5/2}$	$CuInS_2$	444.60	[158]
In $3d_{5/2}$	$CuInS_2$	444.80	[211]
In $3d_{5/2}$	$CuInS_2$	445.50	[211]
In $3d_{5/2}$	$CuInSSe$	444.90	[158]
In $3d_{5/2}$	In_2O_3	444.30	[212]
In $3d_{5/2}$	In_2O_3	444.50	[213]
In $3d_{5/2}$	In_2O_3	445.30	[214]
In $3d_{5/2}$	In_2Se_3	444.50	[209]
In $3d_{5/2}$	In_2Se_3	444.80	[77]
In $3d_{5/2}$	In_2Se_3	445.10	[210]
Cu $2p_{3/2}$	CuS	931.90	[198]
Cu $2p_{3/2}$	CuS	931.90	[192]
Cu $2p_{3/2}$	CuS	932.10	[215]
Cu $2p_{3/2}$	CuS	932.20	[211]

Cu $2p_{3/2}$	CuS	932.20	[216]
Cu $2p_{3/2}$	CuS	932.30	[217]
Cu $2p_{3/2}$	CuS	932.30	[218]
Cu $2p_{3/2}$	CuS	932.50	[219]
Cu $2p_{3/2}$	CuS	935.00	[220]
Cu $2p_{3/2}$	Cu_2S	932.10	[192]
Cu $2p_{3/2}$	Cu_2S	932.20	[221]
Cu $2p_{3/2}$	Cu_2S	932.40	[198]
Cu $2p_{3/2}$	Cu_2S	932.40	[220]
Cu $2p_{3/2}$	Cu_2S	932.50	[206]
Cu $2p_{3/2}$	Cu_2S	932.50	[215]
Cu $2p_{3/2}$	Cu_2S	932.60	[217]
Cu $2p_{3/2}$	Cu_2S	932.70	[219]
Cu $2p_{3/2}$	Cu_2S	932.90	[222]
Cu $2p_{3/2}$	Cu_2S	932.90	[223]
Cu $2p_{3/2}$	$CuInS_2$	932.30	[211]
Cu $2p_{3/2}$	$CuInS_2$	932.40	[198]
Cu $2p_{3/2}$	$CuInS_2$	932.40	[211]
Cu $2p_{3/2}$	$CuInS_2$	933.00	[211]
Cu $2p_{3/2}$	$CuGaS_2$	932.10	[198]
Cu $2p_{3/2}$	$CuSe$	932.00	[216]
Cu $2p_{3/2}$	Cu_2Se	931.90	[216]
Cu $2p_{3/2}$	Cu_2Se	931.90	[198]
Cu $2p_{3/2}$	Cu_2Se	932.50	[209]
Cu $2p_{3/2}$	$CuInSe_2$	931.80	[209]
Cu $2p_{3/2}$	$CuInSe_2$	931.90	[210]
Cu $2p_{3/2}$	$CuInSe_2$	932.49	[224]
Cu $2p_{3/2}$	$CuIn_3Se_5$	932.70	[57]
Cu $2p_{3/2}$	$CuGa_5Se_8$	932.50	[57]

7.3 Supporting Material for Chapter 4

Table 7.3 Full width at half maximum (FWHM) values of the considered core level peaks in the course of the annealing process in case of Cu-poor and Cu-rich CIGSe/CdS samples, obtained by peak fitting in the quantitative analysis in Chapter 4.

	Cu-poor CIGSe/CdS												
T(°C) / Δ (eV)	**RT**	**180**	**200**	**220**	**240**	**260**	**280**	**300**	**320**	**340**	**360**	**380**	**400**
Cu $2p_{3/2}$	0.96	0.97	0.95	0.97	0.97	0.97	0.96	0.96	0.97	0.98	0.98	1.00	1.01
In $3d_{5/2}$	0.86	0.89	0.88	0.87	0.87	0.86	0.86	0.86	0.89	0.92	0.92	0.92	0.91
Ga $2p_{3/2}$	1.10	1.13	1.10	1.13	1.11	1.13	1.11	1.10	1.10	1.15	1.23	1.24	1.25
Se $2p_{3/2}$	1.36	1.38	1.37	1.36	1.38	1.37	1.37	1.37	1.38	1.41	1.42	1.44	1.45
Cd $3d_{5/2}$	0.98	0.98	0.97	0.95	0.94	0.92	0.93	0.95	0.93	0.93	-	-	-
S 1s	1.25	1.26	1.26	1.28	1.28	1.30	1.33	1.38	1.41	1.46	1.46	1.47	1.49
	Cu-rich CIGSe/CdS												
Cu $2p_{3/2}$	0.92	0.93	0.94	0.95	0.94	0.94	0.95	0.95	0.96	0.96	0.96	0.96	0.95
In $3d_{5/2}$	0.77	0.78	0.8	0.8	0.79	0.8	0.79	0.8	0.81	0.81	0.82	0.82	0.82
Ga $2p_{3/2}$	1.05	1.05	1.05	1.09	1.1	1.06	1.04	1.08	1.08	1.08	1.08	1.09	1.1
Se $2p_{3/2}$	1.33	1.34	1.34	1.35	1.35	1.35	1.35	1.36	1.36	1.39	1.4	1.4	1.39
Cd $3d_{5/2}$	0.97	0.98	0.98	0.98	0.96	0.96	0.95	0.93	0.91	0.89	0.9	0.94	0.97
S 1s	1.25	1.23	1.25	1.26	1.28	1.26	1.28	1.29	1.31	1.35	1.37	1.4	1.42

Table 7.4 Standard free energies (G°) of some compounds relevant to the CIGSe/CdS system at different temperatures. Adopted from [3,161]. The listed values are used for the calculation of the free energies of reactions (ΔG), which are shown in Table 4.1 in Chapter 4.

	G° kJ/mol						
Compound \ T(K)	298	300	400	500	600	700	800
CdS	−176.8	−176.9	−185.1	−194.6	−205.1	−216.5	−228.7
CdSe	−170.7	−170.9	−180.1	−190.5	−202.0	−214.4	−227.6
Cu_2S	−115.5	−115.8	−129.4	−146.1	−164.7	−185.0	−206.6
Cu_2Se	−103.9	−104.2	−118.6	−136.7	−156.6	−177.9	−200.4
Ga_2S_3	−558.7	−559.0	−574.9	−593.5	−614.5	−637.4	−662.1
Ga_2Se_3	−462.4	−462.8	−482.6	−505.4	−530.8	−558.2	−587.6
In_2S_3	−404.4	−404.7	−423.0	−444.3	−468.2	−494.3	−522.5
In_2Se_3	−386.4	−386.7	−409.2	−435.9	−466.3	−499.5	−535.0

7.4 List of Abbreviations and Symbols

Table 7.5 List of abbreviations

A	Acceptor
BE	Binding Energy
BESSY	Berliner Elektronenspeicherring-Gesellschaft für Synchrotronstrahlung
BG	Back Ground
CBD	Chemical Bath Deposition
CBM	Conduction Band Minimum
CGI	[Cu]/([Ga]+[In])
CGSe	$CuGaSe_2$
CHA	Concentric Hemispherical Analyzer
CIGSe	$Cu(In,Ga)Se_2$
CISe	$CuInSe_2$
CISSY	Copper Indium Sulfide + Synchrotron
D	Donor
DFT	Density Functional Theory
EDX	Energy Dispersive X-ray spectroscopy
ESCA	Electron Spectroscopy for Chemical Analysis
FWHM	Full Width of Half Maximum
GGI	[Ga]/([Ga]+[In])
HAXPES	Hard X-ray Photoelectron Spectroscopy
HIKE	High Kinetic Energy
ID	Information Depth
IMFP	Inelastic Mean Free Path
KCN	Potassium cyanide
KE	Kinetic Energy
NIST	National Institute of Standards and Technology
ODC	Ordered Defect Compound
OVC	Ordered Vacancy Compound

PDT	Post-Deposition Treatment
PVD	Physical Vapor Deposition
RT	Room Temperature
SEM	Scanning Electron Microscopy
SLG	Soda-lime Glass
TCO	Transparent Conductive Oxide
UHV	Ultra-High Vacuum
UPS	Ultraviolet Photoelectron Spectroscopy
VB	Valence Band
VBM	Valence Band Maximum
XPS	X-ray Photoelectron Spectroscopy

Table 7.6 List of symbols

ΔE_C	Conduction band offset
ΔE_V	Valence band offset
ΔG	Free energy of reaction
ΔH	Formation enthalpy
b	Bowing coefficient
C	Concentration
d	Thickness
$d\sigma/d\Omega$	Partial subshell photoionization cross section
E_C	Conduction band minimum
E_F	Fermi level
E_g	Band gap energy
E_{kin}	Kinetic energy level
E_{pass}	Pass energy
E_V	Valence band maximum
E_{vac}	Vacuum level
$G°$	Standard free energy

h	Planck constant
$h\nu$	Photon energy
k	Boltzmann constant
n	Number of scans
R_0	Radius of hemispherical analyzer
s	Width of entrance slit of analyzer
T	Transmission function of spectrometer
α'	Modified Auger parameter
λ	Inelastic mean free path
ν	Frequency of photon
W	Work function
χ	Electron affinity

References

[1] A. V. Herzog, T.E. Lipman, D.M. Kammen, Renewable energy sources, Encycl. Life Support Syst. Forerunner (2001).

[2] S.W. Glunz, R. Preu, D. Biro, Crystalline silicon solar cells: State-of-the-art and future developments, Compr. Renew. Energy. 1 (2012) 353–387.

[3] J.F. Guillemoles, L. Kronik, D. Cahen, U. Rau, A. Jasenek, H.W. Schock, Stability issues of $Cu(In,Ga)Se_2$-based solar cells, J. Phys. Chem. B. 104 (2000) 4849–4862.

[4] M.A. Green, K. Emery, Y. Hishikawa, W. Warta, E.D. Dunlop, Solar cell efficiency tables (Version 45), Prog. Photovoltaics Res. Appl. 23 (2015) 1–9.

[5] E.A. Alsema, Energy Pay-back Time and CO2 Emissions of PV Systems, Prog. Photovolt Res. Appl. 8 (2000) 17–25.

[6] M. Powalla, W. Witte, P. Jackson, S. Paetel, E. Lotter, R. Wuerz, et al., CIGS cells and modules with high efficiency on glass and flexible substrates, IEEE J. Photovoltaics. 4 (2014) 440–446.

[7] R. Kamada, T. Yagioka, S. Adachi, A. Handa, K.F. Tai, T. Kato, et al., New World Record $Cu(In,Ga)(Se,S)_2$ Thin Film Solar Cell Efficiency Beyond 22%, 43rd IEEE Photovolt. Spec. Conf. (2016) 1287–1291.

[8] A. Chirilă, P. Reinhard, F. Pianezzi, P. Bloesch, A.R. Uhl, C. Fella, et al., Potassium-induced surface modification of $Cu(In,Ga)Se_2$ thin films for high-efficiency solar cells., Nat. Mater. 12 (2013) 1107–1111.

[9] J. Kiss, T. Gruhn, G. Roma, C. Felser, Theoretical study on the structure and energetics of Cd insertion and Cu depletion of $CuIn_5Se_8$, J. Phys. Chem. C. 117 (2013) 10892–10900.

[10] J. Kiss, T. Gruhn, G. Roma, C. Felser, Theoretical Study on the Diffusion Mechanism of Cd in the Cu-Poor Phase of $CuInSe_2$ Solar Cell Material, J. Phys. Chem. C. 117 (2013) 25933–25938.

[11] Personal discussions with Janos Kiss and Hossein Mirhosseini, Unpublished results, 2015.

[12] C.A. Kaufmann, A. Neisser, R. Klenk, R. Scheer, Transfer of $Cu(In,Ga)Se_2$ thin film solar cells to flexible substrates using an in situ process control, Thin Solid Films. 480–481 (2005) 515–519.

[13] S. Siebentritt, Alternative buffers for chalcopyrite solar cells, Sol. Energy. 77 (2004) 767–775.

[14] D. Liao, A. Rockett, Epitaxial growth of $Cu(In,Ga)Se_2$ on GaAs(110), J. Appl. Phys. 91 (2002) 1978.

[15] D. Liao, A. Rockett, Cu depletion at the $CuInSe_2$ surface, Appl. Phys. Lett. 82 (2003) 2829.

[16] H. Möller, Semiconductors for solar cells, Artech House, New York, 1993.

[17] J.L. Shay, J.H. Wernick, Ternary chalcopyrite semiconductors: Growth, electronic properties, and applications, Pergamon Press, 1975.

[18] B.J. Stanbery, Copper Indium Selenides and Related Materials for Photovoltaic Devices, Crit. Rev. Solid State Mater. Sci. 27 (2002) 73–117.

[19] H. Mönig, Hochenergie-Photoelektronenspektroskopie und winkelabhängige Röntgen-emissionsspektroskopie zur tiefenabhängigen Untersuchung von polykristallinen $Cu(In,Ga)Se_2$-Schichten, PhD Thesis, Freie Univ. Berlin. (2009).

[20] N. Rega, Photolumineszenz von epitaktischen $Cu(In,Ga)Se_2$-Schichten, PhD Thesis, Freie Univ. Berlin. (2004).

[21] A. Luque, S. Hegedus, Handbook of Photovoltaic Science and Engineering, 2003.

[22] T. Gödecke, T. Haalboom, F. Ernst, Phase equilibria of Cu-In-Se I. Stable states and nonequilibrium states of the In_2Se_3-Cu_2Se subsystem, Zeitschrift Für Met. 91 (2000) 622–634.

[23] H. Rodriguez-Alvarez, A. Weber, J. Lauche, C.A. Kaufmann, T. Rissom, D. Greiner, et al., Formation of $CuInSe_2$ and $CuGaSe_2$ thin-films deposited by three-stage thermal co-evaporation: A real-time X-ray diffraction and fluorescence study, Adv. Energy Mater. 3 (2013) 1381–1387.

[24] S.B. Zhang, S.-H. Wei, A. Zunger, Stabilization of Ternary Compounds via Ordered Arrays of Defect Pairs, Phys. Rev. Lett. 78 (1997) 4059–4062.

[25] S. Wei, S.B. Zhang, A. Zunger, Effects of Ga addition to $CuInSe_2$ on its electronic, structural, and defect properties, Appl. Phys. Lett. 72 (1998) 3199.

[26] C. Persson, Y.J. Zhao, S. Lany, A. Zunger, n-Type doping of $CuInSe_2$ and $CuGaSe_2$, Phys. Rev. B - Condens. Matter Mater. Phys. 72 (2005) 1–14.

[27] T. Nakada, A. Kunioka, Direct evidence of Cd diffusion into $Cu(In,Ga)Se_2$ thin films during chemical-bath deposition process of CdS films, Appl. Phys. Lett. 74 (1999) 2444.

[28] K. Hiepko, J. Bastek, R. Schlesiger, G. Schmitz, R. Wuerz, N. A. Stolwijk, Diffusion and incorporation of Cd in solar-grade $Cu(In,Ga)Se_2$ layers, Appl. Phys. Lett. 99 (2011) 234101.

[29] S.B. Zhang, S.-H. Wei, A. Zunger, H. Katayama-Yoshida, Defect physics of the $CuInSe_2$ chalcopyrite semiconductor, Phys. Rev. B. 57 (1998) 9642–9656.

[30] R. Scheer, H.-W. Schock, Chalcogenide Photovoltaics Physics, Technologies, and Thin Film Devices, Wiley-VCH Verlag GmbH & Co. KGaA, Weinheim, Germany, 2011.

[31] J.E. Jaffe, A. Zunger, Electronic structure of the ternary chalcopyrite semiconductors $CuAlS_2$, $CuGaS_2$, $CuInS_2$, $CuAlSe_2$, $CuGaSe_2$, and $CuInSe_2$, Phys. Rev. B. 28 (1983) 5822.

[32] T. Nakada, Invited Paper: CIGS-based thin film solar cells and modules: Unique material properties, Electron. Mater. Lett. 8 (2012) 179–185.

[33] C. Persson, Anisotropic hole-mass tensor of $CuIn_{1-x}Ga_x(S,Se)_2$: Presence of free carriers narrows the energy gap, Appl. Phys. Lett. 93 (2008) 10–13.

[34] S.H. Wei, A. Zunger, Band offsets and optical bowings of chalcopyrites and Zn-based II-VI alloys, J. Appl. Phys. 78 (1995) 3846–3856.

[35] S. Chichibu, T. Mizutani, K. Murakami, T. Shioda, T. Kurafuji, H. Nakanishi, et al., Band gap energies of bulk, thin-film, and epitaxial layers of $CuInSe_2$ and $CuGaSe_2$, J. Appl. Phys. 83 (1998) 3678.

[36] M.I. Alonso, K. Wakita, J. Pascual, M. Garriga, N. Yamamoto, Optical functions and electronic structure of $CuInSe_2$, $CuGaSe_2$, $CuInS_2$, and $CuGaS_2$, Phys. Rev. B. 63 (2001) 75203.

[37] M. Turcu, I.M. Kötschau, U. Rau, Composition dependence of defect energies and band alignments in the $Cu(In_{1-x}Ga_x)(Se_{1-y}S_y)_2$ alloy system, J. Appl. Phys. 91 (2002) 1391.

[38] P. Pistor, D. Greiner, C.A. Kaufmann, S. Brunken, M. Gorgoi, A. Steigert, et al., Experimental indication for band gap widening of chalcopyrite solar cell absorbers after potassium fluoride treatment, Appl. Phys. Lett. 105 (2014) 63901.

[39] U. Rau, H.W. Schock, Electronic properties of Cu(In,Ga)Se_2 heterojunction solar cells–recent achievements, current understanding, and future challenges, Appl. Phys. A - Mater. Sci. Process. 69 (1999) 131–147.

[40] M. Bär, S. Nishiwaki, L. Weinhardt, S. Pookpanratana, O. Fuchs, M. Bär, et al., Depth-resolved band gap in Cu(In,Ga)$(S,Se)_2$ thin films, Appl. Phys. Lett. 93 (2008) 244103.

[41] M. Bär, S. Pookpanratana, L. Weinhardt, R.G. Wilks, B. A. Schubert, B. Marsen, et al., Soft X-rays shedding light on thin-film solar cell surfaces and interfaces, J. Electron Spectros. Relat. Phenomena. 190 (2013) 47–53.

[42] S. Adachi, Handbook on Physical Properties of Semiconductors, II-VI Compound Semiconductors, Kluwer Academic Publishers, Boston, 2004.

[43] O. Madelung, U. Rössler, M. Schulz, Cadmium sulfide (CdS) crystal structure, modifications, Springer-Verlag Berlin Heidelberg, 1999.

[44] A.L. Fahrenbruch, Fundamentals of solar cells, Academic Press, 1983.

[45] R.C. Sharma, Y.A. Chctng, The Cd-S system (Cadmium-Sulfur), J. Phase Equilibria. 17 (1996) 425–431.

[46] H.. Woodbury, Measurement of the Cd-CdS Liquids, J. Phys. Chem. Solids. 24 (1963) 881–884.

[47] I.A. Sysoev, E.K. Raiskin, V.R. Gurev, Measurement of the melting point of sulfides, selenides and tellurides of Zn and Cd, Inorg. Mater. 3 (1967) 341–342.

[48] P. Würfel, U. Würfel, Physics of solar cells, Wiley-VCH, Weinheim, 2009.

[49] T. Minemoto, T. Matsui, H. Takakura, Y. Hamakawa, T. Negami, Y. Hashimoto, et al., Theoretical analysis of the effect of conduction band offset of window/CIS layers on performance of CIS solar cells using device simulation, Sol. Energy Mater. Sol. Cells. 67 (2001) 83–88.

[50] I. Hengel, A. Neisser, R. Klenk, M.C. Lux-steiner, Current transport in

$CuInS_2$:Ga/CdS/ZnO-solar cells, Thin Solid Films. 361–362 (2000) 458–462.

[51] R. Klenk, Characterisation and modelling of chalcopyrite solar cells, Thin Solid Films. 387 (2001) 135–140.

[52] M.A. Contreras, M.J. Romero, B. To, F. Hasoon, R. Noufi, S. Ward, et al., Optimization of CBD CdS process in high-efficiency Cu(In,Ga)Se_2-based solar cells, Thin Solid Films. 403–404 (2002) 204–211.

[53] J. Kessler, K.O. Velthaus, M. Ruckh, R. Laichinger, H.W. Schock, D. Lincot, et al., Chemical Bath Deposition of CdS on CIS, etching effects and growth kinetics, in: 6th Int. Photovolt. Sci. Eng. Conf., 1992: pp. 1005–1010.

[54] Y. Hashimoto, T. Satoh, T. Minemoto, S. Shimakawa, T. Negami, High efficiency CIGS solar cell with extremely thin CdS buffer layer, in: Proc. 17th Eur. Photovolt. Sol. Energy Conf., 2001: pp. 1225–1228.

[55] R. Hunger, M. V. Lebedev, K. Sakurai, T. Schulmeyer, T. Mayer, A. Klein, et al., Junction formation of $CuInSe_2$ with CdS: A comparative study of “dry” and “wet” interfaces, Thin Solid Films. 515 (2007) 6112–6118.

[56] K. Kushiya, H. Hakuma, H. Sano, A. Yamada, M. Konagai, Effects of post-deposition heat treatments on ZnO/CdS/$CuInSe_2$ thin film solar cells studied by photoluminescence measurements, Sol. Energy Mater. Sol. Cells. 35 (1994) 223–229.

[57] D. Schmid, M. Ruckh, H.W. Schock, Photoemission studies on Cu(In,Ga)Se_2 thin films and related binary selenides, Appl. Surf. Sci. 103 (1996) 409–429.

[58] D. Schmid, M. Ruckh, F. Grunwald, H.W. Schock, Chalcopyrite/defect chalcopyrite heterojunctions on the basis of $CuInSe_2$, J. Appl. Phys. 73 (1993) 2902.

[59] T. Löher, W. Jaegermann, C. Pettenkofer, Formation and electronic properties of the CdS/$CuInSe_2$ (011) heterointerface studied by synchrotron-induced photoemission, J. Appl. Phys. 77 (1995) 731.

[60] D. Abou-Ras, G. Kostorz, A. Romeo, D. Rudmann, A.N. Tiwari, Structural and chemical investigations of CBD- and PVD-CdS buffer layers and interfaces in Cu(In,Ga)Se_2-based thin film solar cells, Thin Solid Films. 480–481 (2005) 118–123.

[61] T. Nakada, Nano-structural investigations on Cd-doping into Cu(In,Ga)Se_2 thin films by chemical bath deposition process, Thin Solid Films. 361–362 (2000) 346–352.

[62] B. Ümsür, W. Calvet, B. Höpfner, A. Steigert, I. Lauermann, M. Gorgoi, et al., Investigation of Cu-poor and Cu-rich Cu(In,Ga)Se_2/CdS interfaces using hard X-ray photoelectron spectroscopy, Thin Solid Films. 582 (2015) 366–370.

[63] J. Hedstrom, H. Ohlsen, M. Bodegard, A. Kylner, L. Stolt, D. Hariskos, et al., ZnO/CdS/Cu(In,Ga)Se_2 thin film solar cells with improved performance, in: 23rd IEEE Photovolatic Spec. Conf., 1993: pp. 364–371.

[64] R. Caballero, C.A. Kaufmann, T. Eisenbarth, A. Grimm, I. Lauermann, T. Unold, et al., Influence of Na on Cu(In,Ga)Se_2 solar cells grown on polyimide substrates at low temperature: Impact on the Cu(In,Ga)Se_2/Mo interface, Appl. Phys. Lett. 96 (2010) 92104.

[65] R. Caballero, C.A. Kaufmann, T. Eisenbarth, M. Cancela, R. Hesse, T. Unold, et al., The influence of Na on low temperature growth of CIGS thin film solar cells on polyimide substrates, Thin Solid Films. 517 (2009) 2187–2190.

[66] C.A. Kaufmann, R. Caballero, A. Eicke, T. Rissom, T. Eisenbarth, T. Unold, et al., Aspects for the optimization of CIGSe growth at low temperatures for application in thin film solar cells on polyimide foil, 34th IEEE Photovolt. Spec. Conf. (2009) 000670–000675.

[67] D. Rudmann, D. Brémaud, H. Zogg, A.N. Tiwari, Na incorporation into Cu(In,Ga)Se_2 for high-efficiency flexible solar cells on polymer foils, J. Appl. Phys. 97 (2005) 84903.

[68] R. Wuerz, A. Eicke, F. Kessler, P. Rogin, O. Yazdani-Assl, Alternative sodium sources for Cu(In,Ga)Se_2 thin-film solar cells on flexible substrates, Thin Solid Films. 519 (2011) 7268–7271.

[69] K. Granath, M. Bodegard, L. Stolt, The effect of NaF on Cu(In,Ga)Se_2 thin film solar cells, Sol. Energy Mater. Sol. Cells. 60 (2000) 279–293.

[70] T. Maeda, A. Kawabata, T. Wada, First-principles study on alkali-metal effect of Li, Na, and K in $CuInSe_2$ and $CuGaSe_2$, Jpn. J. Appl. Phys. 54 (2015) 08KC20-1-08KC20-8.

[71] M.A. Contreras, B. Egaas, P. Dippo, J. Webb, J. Granata, K. Ramanathan, et al., On the Role of Na and Modifications to Cu(In,Ga)Se_2 Absorber Materials Using Thin-MF (M=Na, K,

Cs) Precursor Layers, in: IEEE Photovolt. Spec. Conf., 1997.

[72] E. Ghorbani, J. Kiss, H. Mirhosseini, G. Roma, M. Schmidt, J. Windeln, et al., Hybrid-Functional Calculations on the Incorporation of Na and K Impurities into the $CuInSe_2$ and $CuIn_5Se_8$ Solar-Cell Materials, J. Phys. Chem. C. 119 (2015) 25197–25203.

[73] P. Jackson, R. Wuerz, D. Hariskos, E. Lotter, W. Witte, M. Powalla, Effects of heavy alkali elements in $Cu(In,Ga)Se_2$ solar cells with efficiencies up to 22.6%, Phys. Status Solidi (RRL). (2016) 1–4.

[74] M. Bodeg Ård, K. Granath, L. Stolt, Growth of $Cu(In,Ga)Se_2$ thin films by coevaporation using alkaline precursors, Thin Solid Films. 361–362 (2000) 9–16.

[75] D. Briggs, M.P. Seah, Practical Surface Analysis, John Wiley & Sons, Chichester, 1983.

[76] S. Hüfner, Photoelectron Spectroscopy: Principles and Applications, Springer-Verlag Berlin Heidelberg GmbH, 2003.

[77] C.D. Wagner, W.M. Riggs, L.E. Davis, J.F. Moulder, G.E. Muilenberg, Handbook of X-ray Photoelectron Spectroscopy, Perkin-Elmer Corporation, 1979.

[78] S. Hofmann, Auger- and X-Ray Photoelectron Spectroscopy in Materials Science, Springer Heidelberg New York Dordrecht London, 2013.

[79] S. Suga, A. Sekiyama, Photoelectron Spectroscopy: Bulk and Surface Electronic Structures, Springer-Verlag Berlin Heidelberg, 2014.

[80] P. van der Heide, X-ray Photoelectron Spectroscopy: An Introduction to Principles and Practices, John Wiley & Sons, Inc., 2012.

[81] A.M. Gabor, J.R. Tuttle, D.S. Albin, M.A. Contreras, R. Noufi, A.M. Gabor, et al., High efficiency $CuIn_xGa_{1-x}Se_2$ solar cells made from $(In_x,Ga_{1-x})_2Se_3$ precursor films, Appl. Phys. Lett. 65 (1994) 198.

[82] C.A. Kaufmann, R. Caballero, T. Unold, R. Hesse, R. Klenk, S. Schorr, et al., Depth profiling of $Cu(In,Ga)Se_2$ thin films grown at low temperatures, Sol. Energy Mater. Sol. Cells. 93 (2009) 859–863.

[83] A.M. Gabor, J.R. Tuttle, M.H. Bode, A. Franz, A.L. Tennant, M.A. Contreras, et al., Band-gap engineering in $Cu(In,Ga)Se_2$ thin films grown from $(In,Ga)_2Se_3$ precursors, Sol. Energy

Mater. Sol. Cells. 41/42 (1996) 247–260.

[84] R. Würz, A. Meeder, D. Fuertes Marrón, T. Schedel-Niedrig, A. Knop-Gericke, K. Lips, Native oxidation of $CuGaSe_2$ crystals and thin films studied by electron paramagnetic resonance and photoelectron spectroscopy, Phys. Rev. B. 70 (2004) 205321.

[85] J. Lehmann, S. Lehmann, I. Lauermann, T. Rissom, C.A. Kaufmann, M.C. Lux-Steiner, et al., Reliable wet-chemical cleaning of natively oxidized high-efficiency $Cu(In,Ga)Se_2$ thin-film solar cell absorbers, J. Appl. Phys. 116 (2014) 233502.

[86] M. Kauk, K. Ernits, T. Varema, M. Altosaar, E. Mellikov, Chemical treatment of $CuInSe_2$ monograin powder surface, EMRS Spring Meet. (2004) Strasbourg (France).

[87] R. Caballero, C. Guillén, M.T. Gutiérrez, C.A. Kaufmann, $CuIn_{1-x}Ga_xSe_2$-based thin-film solar cells by the selenization of sequentially evaporated metallic layers, Prog. Photovoltaics Res. Appl. 14 (2006) 145–153.

[88] L. Weinhardt, O. Fuchs, D. Gross, E. Umbach, C. Heske, N.G. Dhere, et al., Surface modifications of $Cu(In,Ga)S_2$ thin film solar cell absorbers by KCN and H_2O_2/H_2SO_4 treatments, J. Appl. Phys. 100 (2006) 24907.

[89] T. Schulmeyer, Mechanismen der Grenzflächenausbildung des $Cu(In,Ga)Se_2$ -Systems, PhD Thesis, Technische Universität Darmstadt, 2005.

[90] R. Klenk, T. Walter, H.-W. Schock, D. Cahen, A model for the successful growth of polycrystalline films of $CuInSe_2$ by multisource physical vacuum evaporation, Adv. Mater. 5 (1993) 114–119.

[91] I. Lauermann, C. Loreck, A. Grimm, R. Klenk, H. Mönig, M.C. Lux-Steiner, et al., Cu-accumulation at the interface between sputter-(Zn,Mg)O and $Cu(In,Ga)(S,Se)_2$ — A key to understanding the need for buffer layers?, Thin Solid Films. 515 (2007) 6015–6019.

[92] P.M.P. Salomé, J. Keller, T. Törndahl, J.P. Teixeira, N. Nicoara, R.R. Andrade, et al., CdS and $Zn_{1-x}Sn_xO_y$ buffer layers for CIGS solar cells, Sol. Energy Mater. Sol. Cells. 159 (2017) 272–281.

[93] R. Hunger, T. Schulmeyer, M. Lebedev, A. Klein, W. Jaegermann, R. Kniese, et al., Removal of the surface inversion of $CuInSe_2$ absorbers by NH3,aq etching, 3rd World Conf.

Photovolt. Energy Convers. May 11-18, 2003 Osaka, Japan. 2LN-C–04 (2003) 566–569.

[94] T. Lepetit, Influence of KF post deposition treatment on the polycrystalline Cu(In,Ga)Se_2/CdS heterojunction formation for photovoltaic application, PhD Thesis, Université de Nantes, 2015.

[95] M. Bär, H.-J. Muffler, C.-H. Fischer, S. Zweigart, F. Krag, M.C. Lux-steiner, ILGAR-ZnO Window Extension Layer: An Adequate Substitution of the Conventional CBD-CdS Buffer in Cu(In,Ga)$(S,Se)_2$-based Solar Cells with Superior Device Performance, Prog. Photovoltaics Res. Appl. 10 (2002) 173–184.

[96] E. Rutherford, The Connexion between the β and the γ Ray Spectra, Philos. Mag. 28 (1914) 305–319.

[97] E. Janocha, Electronic Properties of ALD Zinc Oxide Interfaces and its Implication for Chalcopyrite Absorber Materials, PhD Thesis, Technische Universität Berlin, 2012.

[98] NIST X-ray Photoelectron Spectroscopy Database, srdata.nist.gov/xps/, (2012).

[99] G. Schön, Auger and direct electron spectra in X-ray photoelectron studies of zinc, zinc oxide, gallium and gallium oxide, J. Electron Spectros. Relat. Phenomena. 2 (1973) 75–86.

[100] C.D. Wagner, A. Joshi, The auger parameter, its utility and advantages: a review, J. Electron Spectros. Relat. Phenomena. 47 (1988) 283–313.

[101] G. Moretti, Auger parameter and Wagner plot in the characterization of chemical states by X-ray photoelectron spectroscopy: a review, J. Electron Spectros. Relat. Phenomena. 95 (1998) 95–144.

[102] Lasurface online database, lasurface.com/database/, (2016).

[103] H. Bubert, J.C. Riviere, Surface and Thin Film Analysis, Wiley-VCH Verlag GmbH, 2002.

[104] D.G. Castner, M. Dowsett, P. Gardner, I.S. Gilmore, J.L.S. Lee, G.J. Leggett, et al., Surface Analysis – The Principal Techniques, John Wiley & Sons, Ltd, 2009.

[105] M.P. Seah, W.A. Dench, Quantitative Electron Spectroscopy of Surfaces: A Standard Data Base for Electrron Inelastic Mean Free Paths in Solids, Surf. Interface Anal. 1 (1979) 2–11.

[106] S. Tanuma, C.J. Powell, D.R. Penn, Calculations of Electron Inelastic Mean Free Paths.,

Surf. Interface Anal. 21 (1993) 165–176.

[107] S. Tougaard, QUASES-IMFP-TPP2M code for the calculation of the inelastic mean free path, Version 2.2. http://www.quases.com, 2002.

[108] D.A. Shirley, High-resolution x-ray photoemission spectrum of the valence bands of gold, Phys. Rev. B. 5 (1972) 4709–4714.

[109] Sigmaplot, PeakFiT software v4.11, www.sigmaplot. com/products/peakfit/peakfit.php, 1998.

[110] C.D. Wagner, L.E. Davis, M. V Zeller, J.A. Taylor, R.H. Raymond, L.H. Gale, Empirical atomic sensitivity factors for quantitative analysis by electron spectroscopy for chemical analysis, Surf. Interface Anal. 3 (1981) 211–225.

[111] M.B. Trzhaskovskaya, V.I. Nefedov, V.G. Yarzhemsky, Photoelectron angular distribution parameters for elements Z=1 to Z=54 in the photoelectron energy range 100–5000 eV, At. Data Nucl. Data Tables. 77 (2001) 97–159.

[112] M.B. Trzhaskovskaya, V.I. Nefedov, V.G. Yarzhemsky, Photoelectron angular distribution parameters for elements Z=55 to Z=100 in the photoelectron energy range 100–5000 eV, At. Data Nucl. Data Tables. 82 (2002) 257–311.

[113] R. Tschöke, Untersuchung der Phasenbildung in Cu/In-Legierungen als Ausgangsmaterialien für $CuInS_2$-Dünnschichtsolarzellen, Master Thesis, Freie Univ. Berlin. (2010).

[114] M. Cardona, L. Ley, Photoemission in Solids I, Springer-Verlag Berlin Heidelberg, 1978.

[115] T. Alford, L. Feldman, J. Mayer, Fundamentals of Nanoscale Film Analysis, Springer US, 2007.

[116] BESSY, Information for Users, www.helmholtz-berlin.de, (2016).

[117] F. Schaefers, M. Mertin, M. Gorgoi, KMC-1: A high resolution and high flux soft x-ray beamline at BESSY, Rev. Sci. Instrum. 78 (2007) 123102.

[118] M.J. Hetzer, Y.M. Strzhemechny, M. Gao, M.A. Contreras, A. Zunger, L.J. Brillson, Direct observation of copper depletion and potential changes at copper indium gallium diselenide grain boundaries, Appl. Phys. Lett. 86 (2005) 162105.

[119] H. Mönig, C. Fischer, A. Grimm, B. Johnson, C.A. Kaufmann, H. Mönig, et al., Surface Cu-depletion of Cu(In,Ga)Se_2 thin films: Further experimental evidence for a defect-induced surface reconstruction, J. Appl. Phys. 107 (2010) 113540.

[120] A. Rockett, D. Liao, J.T. Heath, J.D. Cohen, Y.M. Strzhemechny, L.J. Brillson, et al., Near-surface defect distributions in Cu(In,Ga)Se_2, Thin Solid Films. 431–432 (2003) 301–306.

[121] A. Hofmann, C. Pettenkofer, The $CuInSe_2$–$CuIn_3Se_5$ defect compound interface: Electronic structure and band alignment, Appl. Phys. Lett. 101 (2012) 62108.

[122] S. Toki, T. Nishimura, H. Sugiura, K. Nakada, A. Yamada, Improvement of Cu(In,Ga)Se_2 photovoltaic performance by adding Cu-poor compounds Cu(In,Ga)$_3Se_5$ at Cu(In,Ga)Se_2/CdS interface, IEEE PVSC. (2016) 512–517.

[123] G. Henkelman, B.P. Uberuaga, H.A. Jonsson, Climbing image Nudged Elastic Band method for finding saddle points and minimum energy paths, J. Chem. Phys. 113 (2000) 9901–9904.

[124] J. Heyd, G.E. Scuseria, M. Ernzerhof, Hybrid Functionals Based on a Screened Coulomb Potential, J. Chem. Phys. 118 (2003) 8207–8215.

[125] J. Kaneshiro, N. Gaillard, R. Rocheleau, E.M. Ã, Advances in copper-chalcopyrite thin films for solar energy conversion, Sol. Energy Mater. Sol. Cells. 94 (2010) 12–16.

[126] I. Repins, M.A. Contreras, B. Egaas, C. Dehart, J. Scharf, C.L. Perkins, 19.9%-efficient ZnO/CdS/ $CuInGaSe_2$ Solar Cell with 81.2% Fill Factor, Prog. Photovoltaics Res. Appl. 16 (2008) 235–239.

[127] S. Kijima, T. Nakada, High-temperature degradation mechanism of Cu(In,Ga)Se_2-based thin film solar cells, Appl. Phys. Express. 1 (2008) 75002.

[128] C. Heske, D. Eich, R. Fink, E. Umbach, T. van Buuren, C. Bostedt, et al., Observation of intermixing at the buried CdS/Cu(In,Ga)Se_2 thin film solar cell heterojunction, Appl. Phys. Lett. 74 (1999) 1451–1453.

[129] D. Liao, A. Rockett, Cd doping at the $CuInSe_2$/CdS heterojunction, J. Appl. Phys. 93 (2003) 9380.

[130] U. Rau, M. Schmidt, Electronic properties of ZnO/CdS/Cu(In,Ga)Se_2 solar cells-aspects of heterojunction formation, Thin Solid Films. 387 (2001) 141–146.

[131] H. Mönig, C.-H. Fischer, R. Caballero, C.A. Kaufmann, N. Allsop, M. Gorgoi, et al., Surface Cu depletion of Cu(In,Ga)Se_2 films: An investigation by hard X-ray photoelectron spectroscopy, Acta Mater. 57 (2009) 3645–3651.

[132] K. Ramanathan, R.N. Bhattacharya, J. Granata, J. Webb, D. Niles, M.A. Contreras, et al., Advances in the CIS research at NREL, in: 26th IEEE PVSC, 1997: pp. 319–322.

[133] N.A. Stolwijk, S. Obeidi, J. Bastek, R. Wuerz, A. Eicke, N.A. Stolwijk, et al., Fe diffusion in polycrystalline Cu(In,Ga)Se_2 layers for thin-film solar cells, Appl. Phys. Lett. 96 (2010) 244101.

[134] S. Obeidi, R. Würz, M. Frankenfeld, A. Eicke, N.A. Stolwijk, Diffusion of iron into solar-grade CIGS layers from natural and radioactive front-side sources, Thin Solid Films. 517 (2009) 2205–2208.

[135] J. Bastek, N.A. Stolwijk, R. Wuerz, A. Eicke, J. Albert, S. Sadewasser, Zinc diffusion in polycrystalline Cu(In,Ga)Se_2 and single-crystal CuInSe2 layers, Appl. Phys. Lett. 101 (2012) 74105.

[136] J. Haarstrich, M. Teichmann, H. Metzner, M. Gnauck, C. Ronning, W. Wesch, et al., Buffer-free Cu(In,Ga)Se_2-solar cells by near-surface ion implantation, Sol. Energy Mater. Sol. Cells. 116 (2013) 43–48.

[137] L.E. Oikkonen, M.G. Ganchenkova, A.P. Seitsonen, R.M. Nieminen, Effect of sodium incorporation into $CuInSe_2$ from first principles, J. Appl. Phys. 114 (2013) 83503.

[138] A.P. Kumar, K. V. Reddy, Cadmium diffusion in $CuInSe_2$ thin film, Semicond. Sci. Technol. 12 (1997) 966–969.

[139] E.I. Altman, M. Bienfait, H. Brune, R. Diehl, V.G. Lifshitz, M.E. Michel, et al., Physics of Covered Solid Surfaces, Springer Verlag Berlin Heidelberg New York, 2001.

[140] S. Oswald, X-ray Photoelectron Spectroscopy in Analysis of Surfaces, Encycl. Anal. Chem. (2013).

[141] B. Yin, C. Lou, (112) Surface of $CuInSe_2$ Thin Films with Doped Cd Atoms, Adv. Condens. Matter Phys. 2015 (2015) 1–7.

[142] J.F. Guillemoles, Stability of Cu(In,Ga)Se_2 solar cells: A thermodynamic approach, Thin

Solid Films. 361–362 (2000) 338–345.

[143] O. Cojocaru-Mirédin, P. Choi, R. Wuerz, D. Raabe, Atomic-scale characterization of the CdS/$CuInSe_2$ interface in thin-film solar cells, Appl. Phys. Lett. 98 (2011) 103504.

[144] O. Cojocaru-Mirédin, P. Choi, R. Wuerz, D. Raabe, Exploring the p-n junction region in Cu(In,Ga)Se_2 thin-film solar cells at the nanometer-scale, Appl. Phys. Lett. 101 (2012) 181603.

[145] N.J. Biderman, S.W. Novak, R. Sundaramoorthy, P. Haldar, J.R. Lloyd, Insights into cadmium diffusion mechanisms in two-stage diffusion profiles in solar-grade Cu(In,Ga)Se_2 thin films, Appl. Phys. Lett. 107 (2015) 232104.

[146] S.M. Park, T.G. Kim, Y.D. Chung, D.-H. Cho, J. Kim, K.J. Kim, et al., Junction formation at the interface of CdS/$CuIn_xGa_{(1-x)}Se_2$, J. Phys. D. Appl. Phys. 47 (2014) 345302.

[147] Y.L. Soo, S. Huang, Y.H. Kao, S.K. Deb, K. Ramanathan, T. Takizawa, Migration of constituent atoms and interface morphology in a heterojunction between CdS and $CuInSe_2$ single crystals, J. Appl. Phys. 86 (1999) 6052–6058.

[148] T. Schulmeyer, R. Hunger, R. Fritsche, B. Jäckel, W. Jaegermann, A. Klein, et al., Interfaces of chalcogenide solar cells: a study of the composition at the Cu(In,Ga)Se_2/CdS contact, Thin Solid Films. 480–481 (2005) 110–117.

[149] S. Sadewasser, W. Bremsteller, T. Plake, C.A. Kaufmann, C. Pettenkofer, S. Sadewasser, et al., Microscopic investigation of the CdS buffer layer growth on Cu(In,Ga)Se_2 absorbers, J. Vac. Sci. Technol. B. 26 (2008) 901.

[150] R. Hunger, T. Schulmeyer, A. Klein, W. Jaegermann, M. V. Lebedev, K. Sakurai, et al., SXPS investigation of the Cd partial electrolyte treatment of $CuInSe_2$ absorbers, Thin Solid Films. 480–481 (2005) 218–223.

[151] M. Morkel, L. Weinhardt, B. Lohmüller, C. Heske, E. Umbach, W. Riedl, et al., Flat conduction-band alignment at the CdS/$CuInSe_2$ thin-film solar-cell heterojunction, Appl. Phys. Lett. 79 (2001) 4482–4484.

[152] A. Kylner, The Chemical Bath Deposited CdS/Cu(In,Ga)Se_2 Interface as Revealed by X-Ray Photoelectron Spectroscopy, J. Electrochem. Soc. 146 (1999) 1816–1823.

[153] L.L. Kazmerski, P.J. Ireland, O. Jamjoum, R.A. Mickelsen, W. Chen, A.H. Clark, Summary Abstract: Annealing and interface effects in CdS–$CuInSe_2$ solar cells, J. Vac. Sci. Technol. 20 (1982) 308–309.

[154] L.L. Kazmerski, O. Jamjoum, P.J. Ireland, R.A. Mickelsen, W. Chen, Formation, growth, and stability of the CdS/$CuInSe_2$ interface, J. Vac. Sci. Technol. 21 (1982) 486.

[155] K. Ramanathan, H. Wiesner, S. Asher, D. Niles, R.N. Bhattacharya, M.A. Contreras, et al., High-Efficiency $Cu(In,Ga)Se_2$ Thin Film Solar Cells Without Intermediate Buffer Layers, in: 2nd World Conf. Exhib. Photovolt. Sol. Energy Convers., 1998.

[156] J. Han, C. Liao, L. Cha, T. Jiang, X. Hua-mu, Z. Kui, et al., TEM and XPS studies on CdS/CIGS interfaces, J. Phys. Chem. Solids. 75 (2014) 1279–1283.

[157] D.J. Schroeder, G.D. Berry, A.A. Rockett, Gallium diffusion and diffusivity in $CuInSe_2$ epitaxial layers, Appl. Phys. Lett. 69 (1996) 4068.

[158] C.C. Landry, A.R. Barron, Synthesis of Polycrystalline Chalcopyrite Semiconductors by Microwave Irradiation, Sci. Reports. 260 (1993) 1653–1655.

[159] C. Malitesta, D. Centonze, L. Sabbatini, P.G. Zambonin, L.P. Bicelli, S. Maffi, Analytical Characterization by X-Ray Photoelectron Spectroscopy of Quaternary Chalcogenides for Cathodes in Lithium Cells, J. Mater. Chem. 1 (1991) 259–263.

[160] J.C.J.M. Terhell, R.M.A. Lieth, Preparation and crystallography of gallium sulfide–selenide solid solutions, Phys. Status Solidi. 5 (1971) 719.

[161] O. Knacke, O. Kubaschewski, H. Hasselmann, Thermochemical properties of inorganic substances, 2nd ed., Springer Verlag Berlin, 1991.

[162] J.B. Chaudhari, N.G. Deshpande, Y.G. Gudage, A. Ghosh, V.B. Huse, R. Sharma, Studies on growth and characterization of ternary $CdS_{1-x}Se_x$ alloy thin films deposited by chemical bath deposition technique, Appl. Surf. Sci. 254 (2008) 6810–6816.

[163] C. Paracchini, A. Parisini, L. Tarricone, $CdIn_2S_2Se_2$: A new semiconducting compound, J. Solid State Chem. 65 (1986) 40–44.

[164] P. Vijayakumar, P. Ramasamy, Investigation on synthesis, growth and characterization of $CdIn_2S_2Se_2$ single crystal grown by vertical Bridgman method, J. Cryst. Growth. (2016).

[165] N.M. Gasanly, A.F. Goncharov, N.N. Melnik, A.S. Ragimov, Optical Phonons in $GaS_{1-x}Se_x$ Layer Mixed Crystals, Phys. Status Solidi. 120 (1983) 137–147.

[166] C.S. Jung, F. Shojaei, K. Park, J.Y. Oh, H.S. Im, D.M. Jang, et al., Red-to-Ultraviolet Emission Tuning of Two-Dimensional Gallium Sulfide/ Selenide, ACS Nano. 9 (2015) 9585–9593.

[167] P. Jackson, D. Hariskos, R. Wuerz, O. Kiowski, A. Bauer, T.M. Friedlmeier, et al., Properties of $Cu(In,Ga)Se_2$ solar cells with new record efficiencies up to 21.7%, Phys. Status Solidi - Rapid Res. Lett. 9 (2015) 28–31.

[168] A. Laemmle, R. Wuerz, M. Powalla, Efficiency enhancement of $Cu(In,Ga)Se_2$ thin-film solar cells by a post-deposition treatment with potassium fluoride, Phys. Status Solidi (RRL). 7 (2013) 631–634.

[169] A. Laemmle, R. Wuerz, M. Powalla, Investigation of the effect of potassium on $Cu(In,Ga)Se_2$ layers and solar cells, Thin Solid Films. 582 (2014) 27–30.

[170] P. Reinhard, B. Bissig, F. Pianezzi, E. Avancini, H. Hagendorfer, D. Keller, et al., Features of KF and NaF Postdeposition Treatments of $Cu(In,Ga)Se_2$ Absorbers for High Efficiency Thin Film Solar Cells, Chem. Mater. 27 (2015) 5755–5764.

[171] P. Jackson, D. Hariskos, R. Wuerz, W. Wischmann, M. Powalla, Compositional investigation of potassium doped $Cu(In,Ga)Se_2$ solar cells with efficiencies up to 20.8%, Phys. Status Solidi (RRL). 8 (2014) 219–222.

[172] T.M. Friedlmeier, P. Jackson, A. Bauer, D. Hariskos, O. Kiowski, R. Wuerz, et al., Improved Photocurrent in $Cu(In,Ga)Se_2$ Solar Cells: From 20.8% to 21.7% Efficiency with CdS Buffer and 21.0% Cd-Free, IEEE J. Photovoltaics. 5 (2015) 1487–1491.

[173] F. Pianezzi, P. Reinhard, A. Chirilă, B. Bissig, S. Nishiwaki, S. Buecheler, et al., Unveiling the effects of post-deposition treatment with different alkaline elements on the electronic properties of CIGS thin film solar cells., Phys. Chem. Chem. Phys. 16 (2014) 8843.

[174] F. Pianezzi, P. Reinhard, A. Chirilă, S. Nishiwaki, B. Bissig, S. Buecheler, et al., Defect formation in $Cu(In,Ga)Se_2$ thin films due to the presence of potassium during growth by low temperature co-evaporation process, J. Appl. Phys. 114 (2013) 194508.

[175] L.M. Mansfield, R. Noufi, C.P. Muzzillo, C. Dehart, K. Bowers, B. To, et al., Enhanced performance in Cu(In,Ga)Se_2 solar cells fabricated by the two-step selenization process with a potassium fluoride postdeposition treatment, IEEE J. Photovoltaics. 4 (2014) 1650–1654.

[176] E. Handick, P. Reinhard, J.H. Alsmeier, L. Köhler, F. Pianezzi, S. Krause, et al., Potassium Postdeposition Treatment-Induced Band Gap Widening at Cu(In,Ga)Se_2 Surfaces - Reason for Performance Leap?, ACS Appl. Mater. Interfaces. 7 (2015) 27414–27420.

[177] B. Ümsür, W. Calvet, A. Steigert, I. Lauermann, M. Gorgoi, K. Prietzel, et al., Investigation of the potassium fluoride post deposition treatment on the CIGSe/CdS interface using hard X-ray photoemission spectroscopy – a comparative study, Phys. Chem. Chem. Phys. 18 (2016) 14129–14138.

[178] T.M. Friedlmeier, D. Braunger, D. Hariskos, M. Kaiser, H.N. Wanka, H.W. Schock, Nucleation and growth of the CdS buffer layer on Cu(ln,Ga)Se_2 thin films, in: 25th IEEE Photovolt. Spec. Conf., Washington, D. C., 1996: pp. 845–848.

[179] W. Calvet, H.-J. Lewerenz, C. Pettenkofer, Model experiments on growth modes and interface electronics of $CuInS_2$: Ultrathin epitaxial films on GaAs(100) substrates, Phys. Status Solidi A. 211 (2014) 1981–1990.

[180] H. Xiao, W.A. Goddard, Predicted roles of defects on band offsets and energetics at CIGS (Cu(In,Ga)Se_2/CdS) solar cell interfaces and implications for improving performance, J. Chem. Phys. 141 (2014) 94701.

[181] A.D. Becke, Density-functional thermochemistry. III. The role of exact exchange, J. Chem. Phys. 98 (1993) 5648–5652.

[182] N.E. Christensen, Possibility of heterostructure band offsets as bulk properties: Transitivity rule and orientation effects, Phys. Rev. B. 38 (1988) 12687–12690.

[183] T. Lepetit, S. Harel, E. Gautron, D. Mangin, L. Arzel, N. Barreau, Microstructural implications of the potassium post-deposition treatment in the near-surface CIGSe region, MRS Spring Meet. Exhib. San Fransisco, April 9, B8.02. (2015).

[184] J.L. Shay, B. Tell, H.M. Kasper, L.M. Schiavone, p-d hybridization of the valence bands of I-III-VI2 compounds, Phys. Rev. B. 5 (1972) 5003–5005.

[185] B. Johnson, J. Klaer, A. Vollmer, I. Lauermann, Electronic effects of Cd on the formation of the $CdS/CuInS_2$ heterojunction, J. Vac. Sci. Technol. A. 30 (2012) 04D114.

[186] A. Klein, J. Fritsche, W. Jaegermann, J.H. Schön, C. Kloc, E. Bucher, Fermi level-dependent defect formation at $Cu(In,Ga)Se_2$ interfaces, Appl. Surf. Sci. 166 (2000) 508–512.

[187] J.I. Pankove, Optical Processes in Semiconductors, Dover Publications, Inc., New York, 1971.

[188] D. Strauch, CdS: lattice parameters, in: U. Rössler (Ed.), New Data Updat. Sev. III-V (Including Mix. Crystals) II-VI Compd., Springer Berlin Heidelberg, 2012: pp. 99–102.

[189] P. Reinhard, F. Pianezzi, B. Bissig, A. Chirila, P. Blösch, S. Nishiwaki, et al., $Cu(In,Ga)Se_2$ Thin-Film Solar Cells and Modules— A Boost in Efficiency Due to Potassium, IEEE J. Photovoltaics. 5 (2015) 656–663.

[190] X.-R. Yu, F. Liu, Z.-Y. Wang, Y. Chen, Auger parameters for sulfur-containing compounds using a mixed aluminum-silver excitation source, J. Electron Spectros. Relat. Phenomena. 50 (1990) 159–166.

[191] M. Marychurch, G.C. Morris, X-ray photoelectron spectra of crystal and thin film cadmium sulphide, Surf. Sci. 154 (1985) L251–L254.

[192] V. Bhide, S. Salkalachen, A. Rastogi, C. Rao, M.S. Hegde, Depth profile composition studies of thin film $CdS:Cu_2S$ solar cells using XPS and AES, J. Phys. D Appl. Phys. 14 (1981) 1647–1656.

[193] G. Moretti, A. Anichini, G. Fierro, M. Lo Jacono, P. Porta, Surface Characterization of $Cu_{x/2}Cd_{1-x}In_{2+x/2}S_4$ Model Catalysts, Surf. Interface Anal. 16 (1990) 352–358.

[194] J. Riga, J.J. Verbist, P. Josseaux, A. Kirschdemesmaeker, Correlation between CdS photoanodic behavior and electrode chemical modifications: An x-ray photoelectron spectroscopic study, Surf. Interface Anal. 7 (1985) 163–168.

[195] D.M. Poirier, J.H. Weaver, CdS by XPS, Surf. Sci. Spectra. 2 (1993) 249.

[196] M.P. Houng, S.L. Fu, T.S. Wu, Effect of surface chemisorption on the photoconductivity enhancement of CdS thick films, J. Mater. Sci. Lett. 5 (1986) 96–98.

[197] I.B. Rufus, V. Ramakrishnan, B. Viswanathan, J.C. Kuriacose, Surface characterization of

$CdS_{0.62}Se_{0.38}$ by X-ray photoelectron spectroscopy, J. Mater. Sci. Lett. 11 (1992) 252–254.

[198] I. Nakai, Y. Sugitani, K. Nagashima, Y. Niwa, X-ray photoelectron spectroscopic study of copper minerals, J. Inorg. Nucl. Chem. 40 (1978) 789–791.

[199] Y. Tao, A. Yelon, E. Sacher, Z.H. Lu, M.J. Graham, Y. Tao, et al., S-passivated InP (100)-(1×1) surface prepared by a wet chemical process, Appl. Phys. Lett. 60 (1992) 2669.

[200] J.M. Thomas, I. Adams, R.H. Williams, M. Barber, Valence Band Structures and Core-Electron Energy Levels in the Monochalcogenides of Gallium, J. Chem. Soc. Faraday Trans II. 68 (1972) 755–764.

[201] S.W. Gaarenstroom, N. Winograd, S.W. Gaarenstroom, N. Winograd, Initial and final state effects in the ESCA spectra of cadmium and silver oxides, J. Chem. Phys. 67 (1977) 3500.

[202] O.P. Tkachenko, E.S. Shpiro, M. Wark, G. Schulz-ekloff, N. Jaeger, X-Ray Photoelectron / X-Ray Excited Auger Electron Spectroscopic Study of Highly Dispersed Semiconductor CdS and CdO Species in Zeolites, J. Chem. Soc. Faraday Trans. 89 (1993) 3987–3994.

[203] M. Polak, X-ray Photoelectron Spectroscopic Studies of $CdSe_{0.65}Te_{0.35}$, J. Electron Spectros. Relat. Phenomena. 28 (1982) 171–176.

[204] R. Islam, D.R. Rao, X-ray photoelectron spectroscopy of $Zn_{1-x}Cd_xSe$ thin films, J. Electron Spectros. Relat. Phenomena. 81 (1996) 69–77.

[205] C. Battistoni, J.L. Dormann, D. Fiorani, E. Paparazzo, S. Viticoli, An XPS and Mössbauer study of the electronic properties of $ZnCr_xGa_{2-x}O_4$ spinel solid solutions, Solid State Commun. 39 (1981) 581–585.

[206] C.D. Wagner, Chemical shifts of Auger lines, and the Auger parameter, Faraday Discuss. Chem. Soc. 60 (1975) 291.

[207] G. Cossu, G.M. Ingo, G. Mattogno, G. Padeletti, G.M. Proietti, XPS investigation on vacuum thermal desorption of UV/ozone treated GaAs(100) surfaces, Appl. Surf. Sci. 56–58 (1992) 81–88.

[208] O. Lang, Y. Tomm, R. Schlaf, C. Pettenkofer, W. Jaegermann, Single crystalline $GaSe/WSe_2$ heterointerfaces grown by van der Waals epitaxy. II. Junction characterization, J. Appl. Phys. 75 (1994) 7814.

[209] D. Cahen, P.J. Ireland, L.L. Kazmerski, F.A. Thiel, X-ray photoelectron and Auger electron spectroscopic analysis of surface treatments and electrochemical decomposition of $CuInSe_2$ photoelectrodes, J. Appl. Phys. 57 (1985) 4761.

[210] L.L. Kazmerski, O. Jamjoum, P.J. Ireland, S.K. Deb, R.A. Mickelsen, W. Chen, Initial oxidation of $CuInSe_2$, J. Vac. Sci. Technol. 19 (1981) 467.

[211] R. Scheer, H. Lewerenz, Formation of secondary phases in evaporated $CuInS_2$ thin films: A surface analytical study, J. Vac. Sci. Technol. A. 13 (1995) 1924–1929.

[212] G. Hollinger, R. Skheyta-Kabbani, M. Gendry, Oxides on GaAs and InAs surfaces: An x-ray-photoelectron-spectroscopy of reference compounds and thin oxide layers, Phys. Rev. B. 49 (1994) 11159.

[213] H. Yamaura, T. Jinkawa, J. Tamaki, K. Moriya, N. Miura, N. Yamazoe, Indium oxide-based gas sensor for selective detection of CO, Sensors Actuators B. 35–36 (1996) 325–332.

[214] W.K. Liu, W.T. Yuen, R.A. Stradling, Preparation of InSb substrates for molecular beam epitaxy, J. Vac. Sci. Technol. B. 13 (1995) 1539.

[215] J.E. Gebhardt, J.J. McCarron, P.E. Richardson, The effect of cathodic treatment on the anodic polarization of copper sulfides, Hydrometallurgy. 17 (1986) 27–38.

[216] M. Romand, M. Roubin, J.P. Deloume, ESCA studies of some copper and silver selenides, J. Electron Spectros. Relat. Phenomena. 13 (1978) 229–242.

[217] D. Brion, Etude par spectroscopie de photoelectrons de la degradation superficielle de FeS_2, $CuFeS_2$, ZnS et PbS a l’air et dans l’eau, Appl. Surf. Sci. 5 (1980) 133–152.

[218] J.C. Klein, A. Proctor, D.M. Hercules, X-ray Excited Auger Intensity Ratios for Differentiating Copper Compounds, Anal. Chem. 55 (1983) 2055–2059.

[219] D.L. Perry, J.A. Taylor, X-ray photoelectron and Auger spectroscopic studies of Cu_2S and CuS, J. Mater. Res. 5 (1986) 384–386.

[220] V.I. Nefedov, Y. V. Salyn, P.M. Solozhenkin, G.Y. Pulatov, X-ray photoelectron study of surface compounds formed during flotation of minerals, Surf. Interface Anal. 2 (1980) 170–172.

[221] J. Mielczarski, E. Minni, The adsorption of diethyldithiophosphate on cuprous sulphide,

Surf. Interface Anal. 6 (1984) 221–226.

[222] G. Deroubaix, P. Marcus, X-ray photoelectron spectroscopy analysis of copper and zinc oxides and sulphides, Surf. Interface Anal. 18 (1992) 39–46.

[223] B. Strohmeier, Surface spectroscopic characterization of Cu/Al_2O_3 catalysts, J. Catal. 94 (1985) 514–530.

[224] P.E. Sobol, A.J. Nelson, C.R. Schwerdtfeger, W.F. Stickle, J.F. Moulder, Single Crystal $CuInSe_2$ Analysis by High Resolution XPS, Surf. Sci. Spectra. 1 (1992) 393.

List of publications

Part of this thesis has already been published:

B. Ümsür, W. Calvet, A. Steigert, I. Lauermann, M. Gorgoi, K. Prietzel, D. Greiner, C.A. Kaufmann, T. Unold, M.Ch. Lux-Steiner, *Investigation of the potassium fluoride post deposition treatment on the CIGSe/CdS interface using hard X-ray photoemission spectroscopy – a comparative study*, Phys. Chem. Chem. Phys. 18, 14129–14138 (2016).

Other Journal Publications

5. W. Calvet, B. Ümsür, A. Steigert, K. Prietzel, D. Greiner, C.A. Kaufmann, T. Unold, M.Ch. Lux-Steiner, I. Lauermann, *In-situ investigation of as-grown Cu(In,Ga)Se_2 absorbers used for thin film solar cells by means of photoemission spectroscopy*, (under preparation).

4. T. Olar, I. Lauermann, H. Xie, M. Neuschitzer, E. Saucedo, W. Calvet, A. Steigert, B. Ümsür, B. Chacko, V. Parvan, M. Gorgoi, B. Senkovskiy, M.Ch. Lux-Steiner, *Assessment of Chemical and Electronic Surface Properties of the $Cu_2ZnSn(SSe)_4$ After Different Etching Procedures by Synchrotron-based Spectroscopies*, Energy Procedia. 84, 8–16 (2015).

3. S. Bröker, D. Kück, A. Timmer, I. Lauermann, B. Ümsür, D. Greiner, C.A. Kaufmann, H. Mönig, *Correlating the Local Defect-Level Density with the Macroscopic Composition and Energetics of Chalcopyrite Thin-Film Surfaces*, ACS Appl. Mater. Interfaces. 7, 13062–13072 (2015).

2. W. Calvet, B. Ümsür, B. Höpfner, I. Lauermann, K. Prietzel, C.A. Kaufmann, T. Unold, M.Ch. Lux-Steiner, *Locally resolved investigation of wedged Cu(In,Ga)Se_2 films prepared by physical vapor deposition using hard X-ray photoelectron and X-ray fluorescence spectroscopy*, Thin Solid Films. 582, 361–365 (2015).

1. B. Ümsür, W. Calvet, B. Höpfner, A. Steigert, I. Lauermann, M. Gorgoi, K. Prietzel, H.A. Navirian, C.A. Kaufmann, T. Unold, M.Ch. Lux-Steiner, *Investigation of Cu-poor and Cu-rich Cu(In,Ga)Se2/CdS interfaces using hard X-ray photoelectron spectroscopy*, Thin Solid Films. 582, 366–370 (2015).

Oral Presentations

11. B. Ümsür, W. Calvet, A. Bercegol, A. Steigert, J. Kiss, H. Mirhosseini, M. Gorgoi, D. Greiner, C.A. Kaufmann, M.Ch. Lux-Steiner, I. Lauermann, *XPS Analysis of Cd Diffusion into Cu-poor and Cu-rich*

$Cu(In,Ga)Se_2$ Solar Cell Absorbers. 1st International Underground Resources and Energy Conference, 10/2016, Yozgat, Turkey.

10. T. Olar, I. Lauermann, A. Manoharan, L. Pardini, K. Hannewald, C. Draxl, H. Xie, E. Saucedo, W. Calvet, A. Steigert, B. Ümsür, M.Ch. Lux-Steiner, *The band edges development in $Cu_2ZnSn(S,Se)_4$ with different [S]/([S]+[Se]) ratios tackled with synchrotron-based spectroscopy*. E-MRS Spring Meeting, 05/2016, Lille, France.

9. I. Lauermann, R. Mainz, W. Calvet, B. Ümsür, T. Olar, A. Steigert, M.Ch. Lux-Steiner, *In-situ characterization of solar cells using synchrotron techniques*. E-MRS Spring Meeting, 05/2016, Lille, France.

8. W. Calvet, B. Ümsür, A. Steigert, I. Lauermann, B. Chacko, V. Parvan, T. Olar, K. Prietzel, H.A. Navirian, S. Brunken, C.A. Kaufmann, D. Greiner, T. Unold, M.Ch. Lux-Steiner, *Comparison of surface composition, electronic properties, and solar cell performance of UHV-transferred and air exposed CIGSe thin film solar cell absorbers*. 31st European Photovoltaic Solar Energy Conference and Exhibition, 09/2015, Hamburg, Germany.

7. B. Ümsür, W. Calvet, B. Höpfner, A. Steigert, I. Lauermann, M. Gorgoi, K. Prietzel, S. Brunken, D. Greiner, C.A. Kaufmann, T. Unold, M.Ch. Lux-Steiner, *Investigation of KF-PDT on the CIGSe/CdS interface using hard x-ray photoemission spectroscopy*. SolarTR-3, 05/2015, Ankara, Turkey.

6. T. Olar, I. Lauermann, H. Xie, E. Saucedo, W. Calvet, A. Steigert, B. Ümsür, B. Chacko, V. Parvan, M.Ch. Lux-Steiner, *Assessment of the $Cu_2ZnSnSSe_4$ chemical and electronic surface properties after different etching procedures by synchrotron-based spectroscopies*. E-MRS Spring Meeting, 05/2015, Lille, France.

5. W. Calvet, B. Ümsür, A. Steigert, I. Lauermann, K. Prietzel, H.A. Navirian, S. Brunken, C.A. Kaufmann, T. Unold*, The impact of pre-and post-deposition sodium fluoride treatments on CIGSe absorbers and solar cell performance - a comparative study using surface and bulk sensitive analysis tools*. 29th European Photovoltaic Solar Energy Conference and Exhibition, 09/2014, Amsterdam, The Netherlands.

4. W. Calvet, B. Ümsür, A. Steigert, B. Höpfner, I. Lauermann, K. Prietzel, C.A, Kaufmann, T. Unold, M.Ch. Lux-Steiner, *Thickness dependent investigation of wedged $Cu(In,Ga)Se_2$ films prepared by physical vapor deposition (PVD) using hard x-ray photoelectron spectroscopy (HAXPES)*. The 562nd Wilhelm and Else Heraeus-Seminar “From Sunlight to Fuels”, 05/2014, Bad-Honnef, Germany.

3. B. Ümsür, W. Calvet, A. Steigert, B. Höpfner, I. Lauermann, K. Prietzel, C. Kaufmann, T. Unold, M.Ch. Lux-Steiner, *Investigation of Cu-poor and Cu-rich Cu(In,Ga)Se2/CdS interfaces using hard x-ray photoelectron spectroscopy (HAXPES)*. E-MRS Spring Meeting, 05/2014, Lille, France.

2. A. Ennaoui, I. Lauermann, B. Ümsür, F. Hergert, W. Kasper, T. Hahn, A. Flückiger, *Development of chemical bath deposited Zn(S,O) buffer layer for cadmium free Cu-chalcopyrite thin film solar cells during the NeuMaS project*. 27th European Photovoltaic Solar Energy Conference and Exhibition, 09/2012, Frankfurt, Germany.

1. A. Ennaoui, B. Ümsür, A. Grimm, I. Lauermann, *Effect of hot light soaking on* $Cu(In,Ga)(Se,S)_2/Zn(S,O)/ZnO$ *thin film solar cells*. E-MRS Spring Meeting, 05/2012, Strasbourg, France.

Poster Presentations

8. I. Majumdar, B. Ümsür, M. Heinemann, B. Chacko, D. Smirnov, W. Calvet, V. Parvan, A. Mizrak, I. Lauermann, *Depth profiled XPS analysis and NEXAFS study of Na, K-PDT on CIGSe as a function of deposition temperature using synchrotron radiation*. MSE Congress, 09/2016, Darmstadt, Germany.

7. W. Calvet, I. Majumdar, B. Ümsür, A. Steigert, B. Chacko, V. Parvan, T. Olar, C. A. Kaufmann, D. Greiner, J. Lauche, H. Navirian, G. Voorwinden, W. Mannstadt, R. Schlatmann, M. Ch. Lux-Steiner, I. Lauermann, *Analysis of surface composition and device performance of UHV and air-transferred CIGSe thin film solar cell absorbers on alkali-containing substrate glass*. 32nd European Photovoltaic Solar Energy Conference and Exhibition, 06/2016, Munich, Germany.

6. V. Parvan, A. Mizrak, B. Ümsür, W. Calvet, A. Steigert, I. Lauermann. T. Dittrich, D. Greiner, C.A. Kaufmann, M.Ch. Lux-Steiner, *The impact of thin KF, NaF, K, and Na layers on CIGS studied with SPV and XPS/UPS*. E-MRS Spring Meeting, 05/2016, Lille, France.

5. W. Calvet, B. Ümsür, A. Steigert, I. Lauermann, B. Chacko, V. Parvan, T. Olar, K. Prietzel, H.A. Navirian, S. Brunken, C.A. Kaufmann, D. Greiner, T. Unold, M.Ch. Lux-Steiner, *Comparison of surface composition, electronic properties, and solar cell performance of UHV-transferred and air exposed CIGSe thin film solar cell absorbers*. E-MRS Spring Meeting, 05/2015, Lille, France.

4. B. Ümsür, W. Calvet, A. Steigert, I. Lauermann, M. Gorgoi, K. Prietzel, D. Greiner, C.A. Kaufmann, T. Unold, M. Lux-Steiner, *Investigation of the potassium fluoride-post deposition treatment on the CIGS/CdS interface using hard x-ray photoemission spectroscopy – a comparative study*. E-MRS Spring Meeting, 05/2015, Lille, France.

3. T. Olar, I. Lauermann, H. Xie, E. Saucedo, W. Calvet, A. Steigert, B. Ümsür, M.Ch. Lux-Steiner, *Diffusion of indium in kesterite thin-film solar cells investigated by hard x-ray photoelectron spectroscopy*. The 562nd Wilhelm and Else Heraeus-Seminar "From Sunlight to Fuels", 05/2014, Bad-Honnef, Germany.

2. W. Calvet, B. Ümsür, A. Steigert, B. Höpfner, I. Lauermann, K. Prietzel, C. Kaufmann, T. Unold, M. Lux-Steiner, *Thickness dependent investigation of wedged $Cu(In,Ga)Se_2$ films prepared by physical vapor deposition (PVD) using hard x-ray photoelectron spectroscopy (HAXPES)*. E-MRS Spring Meeting, 05/2014, Lille, France.

1. B. Ümsür, W. Calvet, B. Höpfner, A. Steigert, I. Lauermann, M.Ch. Lux-Steiner, *Synchrotron-based analysis of the $Cu(In,Ga)Se_2/CdS$ and $Cu(In,Ga)Se_2/ZnS$ interfaces using soft x-ray photoemission spectroscopy (SXPS) and near edge x-ray absorption fine structure spectroscopy (NEXAFS)*. International Conference on Solar Energy for World Peace, 08/2013, Istanbul, Turkey.

Acknowledgments

I would like to acknowledge all of those who helped and contributed to this work:

- Prof. M. Ch. Lux-Steiner for giving me the opportunity to perform my PhD thesis at her department at the Helmholtz-Zentrum Berlin, for her guidance through this work and for carefully correcting this thesis.
- Prof. W. Kuch for accepting to be my second examiner and for regularly inviting me to present my latest results in his group seminars.
- Dr. Iver Lauermann for accepting me in his CISSY group, for the great supervision during my PhD work, for expanding my horizon in the field of x-ray photoelectron spectroscopy, for the proof reading of this thesis, and for the things that I forget to mention here... It was a great pleasure for me to work in the CISSY group under his supervision.
- Dr. Wolfram Calvet for his continuous guidance during my PhD, especially during the beamtimes at the BESSY, and for his support in writing publications. His contribution to this work is indescribable.
- The current and the former members of the CISSY group: Alexander Steigert, Dr. Britta Höpfner, Tetiana Olar, Binoy Chacko, Vladimir Parvan, Isheta Majumdar, Adrien Bercegol, and Ali Vâlâ Mızrak for creating a pleasant work atmosphere and for their contributions to this work. Especially Alexander Steigert, for being an excellent officemate and for the Friday songs (Applaus Applaus sage ich nur!); and Britta Höpfner for bringing me the details on the quantitative analyses of XPS data in the beginning of my PhD.
- The project partners in Max-Planck Institute for Chemical Physics of Solids Dr. Janos Kiss and Dr. Hossein Mirhosseini for the DFT calculations of the Cd diffusion into the CIGSe materials and for the valuable discussions on it.
- Dr. Jaison Kavalakkatt and Carola Kelch, for the SEM images.
- Dr. Mihaela Gorgoi and Dr. Roberto Felix Duarte for the technical assistance at the HIKE beamline, and Dr. Boris Senkovsky and Dmitry Smirnov at the Russian-German Beamline at BESSY.

- Dr. Christian Kaufmann, Dr. Dieter Greiner, Dr. Marc Daniel Heinemann, Dr. Thomas Unold, Dr. Allaf Navirian Hengameh, and Dr. Stefan Brunken for providing me Cu(In,Ga)Se_2 absorbers during this work.
- Ministry of National Education of the Republic of Turkey (Milli Eğitim Bakanlığı) for the financial support during my Master and PhD.
- My friend/brother Riad for his support in my daily life in Berlin.
- Dr. Ahmet Akın Ünal and Hatice Doğanay for the coffee breaks.
- Last but not least my parents, my brother Yusuf Ümsür, my wife and her parents, and my lovely daughter Sümeyye for their continuous and unlimited support, and for their patience.

Selbständigkeitserklärung

Hiermit erkläre ich, dass ich die vorliegende Dissertation selbständig verfasst und nur mit Hilfe der angegebenen Quellen angefertigt habe. Ich versichere, dass diese Arbeit nicht schon einmal in einem früheren Promotionsverfahren angenommen oder als ungenügend beurteilt worden ist.

Berlin, 30.03.2017

Ort, Datum

Bünyamin Ümsür

Curriculum Vitae

For reasons of data protection, the Curriculum vitae is not published in the online version.